Viable Welding Alloy for Mitigation of Residual Stress and Enhancement of Fatigue Resistance

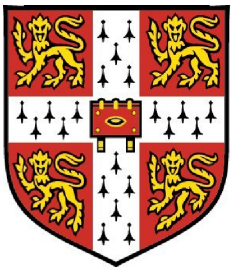

Timothy Issak Ramjaun

Darwin College

University of Cambridge

A dissertation submitted for the degree of Doctor of Philosophy

September 2014

Mum and Dad

Grandma and Grandad

with love

"My son, do not forget my teaching,
but keep my commands in your heart,
for they will prolong your life many years
and bring you prosperity.

Let love and faithfulness never leave you;
bind them around your neck,
write them on the tablet of your heart.
Then you will win favour and a good name
in the sight of God and man.

Trust in the Lord with all of your heart
and lean not on your own understanding;
in all of your ways acknowledge him,
and he will direct your paths."

Proverbs 3 (NIV)

Preface

This thesis is submitted for the degree of Doctor of Philosophy at the University of Cambridge. The research was conducted under the supervision of Professor H. K. D. H. Bhadeshia in the Department of Materials Science and Metallurgy; 2011 – 2014.

This work is original, except where acknowledged or referenced. Neither this, nor any substantially similar thesis has been submitted for a degree, diploma or other qualification at any other university. This dissertation does not exceed the limit of 60,000 words.

Aspects of this work have been published:

T. I. Ramjaun, H. J. Stone, L. Karlsson, J. Kelleher, R. J. Moat, J. R. Kornmeier, K. Dalaei, and H. K. D. H. Bhadeshia: Effect of inter-pass temperature on residual stresses in multi-pass welds produced using a low transformation temperature filler alloy, *Sci. Technol. Weld. Join.*, 2014, 19, 44–51.

T. I. Ramjaun, H. J. Stone, L. Karlsson, J. Kelleher, S. W. Ooi, K. Dalaei, J. R. Kornmeier and H. K. D. H. Bhadeshia: Effects of dilution and baseplate strength on stress distributions in multipass welds deposited using low transformation temperature filler alloys, *Sci. Technol. Weld. Join.*, 2014, 19, 461–567.

S. W. Ooi, J. E. Garnham, and T. I. Ramjaun: Low transformation temperature weld filler for tensile residual stress reduction, *Materials and Design*, 2014, 56, 773–781.

T. I. Ramjaun, H. J. Stone, L. Karlsson, M. A. Gharghouri, K. Dalaei, R. J. Moat and H. K. D. H. Bhadeshia: Surface residual stresses in multipass welds produced using low transformation temperature filler alloys, *Sci. Technol. Weld. Join.*, 2014, 19, 623–630.

T. I. Ramjaun
Cambridge, September 2014

Acknowledgements

I would like to express my sincere gratitude to my supervisor, Professor Harry Bhadeshia, for providing me with the opportunity, support and guidance necessary to pursue this research. I am indebted to Dr Howard Stone for sharing his expertise in strain analysis and sacrificing his time to accompany me on two neutron diffraction experiments. I am grateful to Dr Leif Karlsson, my industrial supervisor, for initiating the project and providing direction, along with the resources necessary to successfully complete it. I am immensely thankful for the privilege of being the understudy of these three prominent researchers.

Performing neutron diffraction experiments is a communal effort and impossible without the dedicated contributions of the team members and instrument scientists. For this reason I would like to thank Joe Kelleher, who accompanied me twice to Germany, and Richard Moat for supporting me in Canada. Both Richard and Joe have been a constant resource during the course of my studies and offered their services generously. I would also like to thank Dr Michael Gharghouri, the local contact at Chalk River, for his hard work and patience, which was required to obtain the involved near-surface strain measurements over a period of many weeks. Steve Ooi and Ivan Lonardelli, from the Phase Transformations Group, were kind enough to assist me at ISIS and Joana Rebelo Kornmeier acted as the FRM2 local contact.

I acknowledge the support and assistance of the Phase Transformations Group, past and present, who have communally provided instruction, insight and discussion. Of course this has been combined with much amiable conversation and coffee, necessary ingredients to triumph through the high and lows of being a Ph.D. student and writing a thesis. Chris, Subhankar, Ed, Hector, Ivan, Wendy, James, Neel, Lucy, Mandla, Wil, Guo Lei, Steve, Rose, Lin Sun, and Matthew – thank you for your friendship. Not forgetting Anita Bailey, who has a gift for booking last minute travel arrangements.

I would like to extend further thanks to all staff members in the Department of Materials Science & Metallurgy who provided assistance and support in completing this project. To Professors Lindsay Greer and Mark Blamire for the provision of laboratory facilities; Ken Thorn, Paul Stokes and Stefan Savage for specimen preparation; Simon Griggs for SEM training. Dr Iris Buisman at the Department of Earth Sciences for EPMA analysis.

Neutron diffraction studies were conducted on the following instruments: ENGIN-X at ISIS, Rutherford Appleton Laboratory, Didcot, UK (Exp. no. RB1210178 and RB1220125); STRESS-SPEC operated by FRM II at the Heinz Maier-Leibnitz Zentrum, Garching, Germany (Exp. no. 6312 and 6903); L3 beam line at the Canadian Neutron Beam Centre, Chalk River Laboratories, Canada. I would like to acknowledge Dr Kamellia Dalaei, ESAB AB, for the X-ray diffraction data and organising a training session so that I could try my hand at welding.

Finally, I am most grateful to ESAB AB, Lindholmsallen 9, 40277 Gothenburg, Sweden for sponsoring me to complete this work.

Abstract

Residual stresses that accumulate during welding are generally deleterious to fatigue performance and arise as a result of thermal contraction of the weld metal following solidification. The shrinkage can, in principle, be compensated by phase transformation strain that is available during martensite formation. Lowering the martensite–start temperature of the welding electrode can furthermore induce compressive stress into the weldment and increase component longevity. The principle of stress alleviation through transformation plasticity has been established in literature but limited to single–pass welds. The work presented in this thesis seeks to characterise the residual stresses that develop in multipass welds, using low–temperature transforming weld material.

The evolution of stress with increasing number of passes and varying interpass temperatures has been assessed. Compressive stress developed in the first welding pass can be eradicated by the deposition of additional layers if the majority of the underlying weld material is not re-austenitised. If the interpass temperature is sufficiently high for all welding passes, the entire weld remains austenitic until all of the layers have been deposited and it becomes possible to exploit the stress reduction benefits that can be derived from each layer. This is the first time such a concept has been proposed and validated by continuity of the solidification structure across weld passes. Further neutron diffraction experiments identified the effects of dilution and base plate strength with a view to optimising the welding process.

Surface stress data were collected using both X-ray and neutron diffraction. The adoption of a small gauge volume permitted the measurement of near-surface stresses using neutrons and revealed the local stress variations at the weld toe. The low-transformation temperature welding alloy is capable of inducing compression into these regions, which contributes towards improved fatigue life. Major differences in the weld deposit stress state exist between the surface and in the bulk material below. A key outcome of the totality of this work is that transformation plasticity influences the stress state in the vicinity of the weld toe such that compression is induced at this critical location.

Contents

Nomenclature

α'	Martensite
β	Material constant used in the Koistinen–Marburger equation
δ	Dilatational strain
$\Delta\sigma$	Stress range
γ	Austenite
λ	Wavelength of incident X-ray
ν	Poisson's ratio
ϕ	Measurement angle relative to sample principal axes
ψ	Scattering angle from sample surface
σ_{a} , σ_{m}	Stress amplitude , Mean stress
σ_{ij}	Stress along the direction ij
θ_{M}	Take off angle from moderator
ε_{ij}	Strain along the direction ij
Ac_3	Temperature at which a sample becomes fully austenitic during heating
B_{S}	Bainite–start temperature
C	Elastic stiffness
$d_{0,hkl}$	Strain–free lattice spacing for hkl planes
d_{hkl}	Lattice spacing for hkl planes
E	Young's Modulus
h	Planck's constant
L	Neutron path length
M_{F}	Martensite–finish temperature
M_{S}	Martensite–start temperature
m_n	Neutron mass
N_{f}	Number of cycles to failure
q	Strain measurement direction

S	Elastic complience
s	Shear strain
t_n	Time–of–flight for a neutron to reach the detector
T_q	Temperature below the M_S
$V_{\alpha'}$	Volume fraction of martensite
V_γ	Volume fraction of retained austenite
CCT	Continuous cooling transformation
EDM	Electro–discharge machining
EDX	Energy–dispersive X-ray
EPMA	Electron probe microanalysis
FWHM	Full width at half maximum
GMAW	Gas–metal arc welding
HAZ	Heat–affected zone
HTT	High transformation temperature
LTT	Low transformation temperature
MCAW	Metal cored arc welding
TOF	Time–of–flight

Chapter 1

Introduction

For over a century, the use of electric arc welding has been utilised to successfully join steel components and the development of this technology has literally fabricated the world that currently surrounds us. Nevertheless, despite a hundred years of continual process improvement, it remains that the welded joints of engineering structures are often the features that limit both the service loads that can be tolerated and their fatigue life [1]. Stress concentration at the boundary between the weld metal and base material caused by geometrical changes contributes to preferential crack initiation and fatigue failure at this site [2]. Susceptibility to microcrack initiation/propagation can be further exacerbated by tensile residual stresses in this region, which accumulate as a result of thermal contraction strains during cooling of the weld metal to ambient temperature [3, 4].

To increase the longevity of welded components, post-weld treatments may be applied that are either mechanical or thermal in nature and aim to change the joint geometry or residual stress state [5]. Unfortunately, these subsequent treatments are often costly or impractical and it would be preferable to modify the welding process itself in order to minimise the occurrence of harmful stresses. In their seminal paper, Jones and Alberry demonstrated a novel mechanism to counter these thermally induced tensile stresses [6]. This is attained through exploitation of the strains associated with the solid-state phase transformation of a martensitic weld filler.

The transformation of austenite to martensite is displacive in nature and during this process multiple dislocations slip to produce a shear strain, which may manifest on a macroscopic scale [7, 8]. The shear component, in conjunction with a dilatational strain, is sufficient to not only cancel the tensile stresses, but even create compression in the weld metal [9]. However, the beneficial effects of stress relaxation through transformation plasticity are dependent on the temperature at which the austenite to martensite transformation occurs. If the transformation takes place above an optimal temperature, continued thermal contraction to ambient temperature leads to further accumulation of tensile stress. Thus, the initial benefits associated with the transformation are eliminated [10]. To avoid this problem, the weld metal should be designed with a low martensite-start temperature, typically 200 °C [11]. The concept of *transformation plasticity* has been used as the basis for explaining stress evolution and is defined in this work as the irreversible deformation resulting from the solid-state transformation of austenite to martensite.

To achieve the prescribed low martensite start temperature while limiting the carbon concentration requires the weld metal to contain relatively large concentrations of solute. Additions of nickel and chromium lead to a total substitutional alloying element concentration of around 15–20 wt% [12]. This is necessary to ensure that the carbon concentration is sufficiently reduced to avoid the embrittlement associated with hard martensite [13]. Low transformation temperature welding alloys have therefore been the subject of much research over the previous few decades. They have proved effective in enhancing fatigue performance but generally to the detriment of toughness [14, 15]. Indeed, judicious alloy design has been required to balance the transformation temperature, whilst still maintaining appropriate mechanical properties in the weld metal. This has been overcome through a combination of thermodynamic calculations and neural networks, to develop a new generation of tough, low transformation temperature welding alloys [16, 17].

Recent fatigue studies have proved the effectiveness of these latest welding fillers, with the understanding that enhanced fatigue performance is founded on a more favourable residual stress state [18]. This has been firmly established when a single layer of weld metal is deposited but there remain signif-

icant knowledge deficiencies regarding the redistribution of stresses following additional welding passes for multiple layer welds. In multipass welds, the heat input from later weld passes may be insufficient to retransform prior welding passes, leading to the accumulation of thermally-induced strains and elevated residual stresses.

The aim of this work therefore was to characterise the residual stresses that invariably develop during the process of multipass welding. A combination of welding alloys and base plates were selected and subjected to strain analysis using neutron diffraction. Near-surface neutron diffraction was also used to probe the residual stress state in the vicinity of the free surface and these results are critically compared with residual stresses determined using X-ray diffraction. This study highlights the differences between the residual stresses at the surface and those in the bulk immediately below it, and serves to rationalise the apparent disparity between the residual stress data obtained with X-ray and neutron diffraction in the literature [19–21].

Chapter 2

Review: Low Transformation Temperature Welding Alloys

2.1 Introduction

The joining of materials is necessary to achieve functionality and current technologies range from the simplicity of nuts & bolts to the manipulation of a high energy electron beam to fuse dissimilar metals. Certainly when it comes to joining steel components for engineering structures, arc welding is often the process of choice. It is versatile, portable and able to produce a final, continuous workpiece with strength equal to the constituent parts. However, the deposition of molten metal on to a steel plate is the equivalent of a localised heat treatment, which influences the microstructure and properties depending on the proximity to the heat source.

Calculating these changes is difficult due to the variables involved and in the case of thick sections, multiple layers of filler material are required to fill large gaps between adjoining workpieces. This further complicates predictions for the final mechanical properties as the base plate and underlying weld metal have both received multiple, localised heat treatments. Residual stresses also accumulate due to thermal contraction strains, which can lead to distortion, stress-corrosion cracking and premature fatigue failure [22]. It is not surprising then, that arc welding has the been the subject of considerable research over the years due to it being both extremely useful and extremely complex.

2.2 Arc Welding

Welding processes are generally divided in to two categories, depending on whether pressure is applied in order to achieve material continuity. Fusion welding involves melting the base plate with or without a filler. Non-fusion welding processes require pressure, with or without heat, to cause plastic deformation of the joining workpieces. Arc welding itself, describes a diverse group of welding techniques that use an electric arc as a heat source to melt and join metals. They are a subsidiary of fusion welding and are most often used with a filler.

The arc is formed between the electrode and the workpiece and the length of weld is created by moving either the electrode or the workpiece. The electrode is used to conduct the current and sustain the electric arc across its tip and the workpiece. In some welding processes the electrode is manufactured from a consumable rod/wire, that in addition to producing the arc, supplies filler material to the joint. A non-consumable tungsten/carbon rod may also be used, in which case a separate source of filler can be implemented. When welding steel products though, the electrode is generally consumed and specially designed to maintain the integrity and properties of the joint once solidified.

A specific variant of arc welding is *gas-metal arc welding* (GMAW), Fig. 2.1, so called because it uses an inert shielding gas to provide a protective atmosphere for the molten weld metal, thus preventing contact with air. The technique is used to weld steels and can incorporate a low-transformation temperature filler wire as the electrode. Once established, the high-temperature arc melts the continuously fed filler wire (electrode) and it is deposited on to the base metal as droplets of molten metal. Concurrently, the arc melts the base metal surface, creating the weld pool, which is a mixture of molten metal from both the filler and workpiece. The temperatures experienced at the tip of the electrode are approximately 3500 °C, which is more than sufficient for melting most metals [23]. The weld pool then solidifies behind the arc as it moves along the workpiece. If executed correctly, the welded joint is often superior in strength compared with the base metal being joined. However, the heat that is necessary to melt and fuse the workpieces can cause various metallurgical effects in

the weld metal and the adjacent base metal. The heat flow during welding, which is predominately dissipated through the base plate, is also responsible for weld residual stresses and distortion.

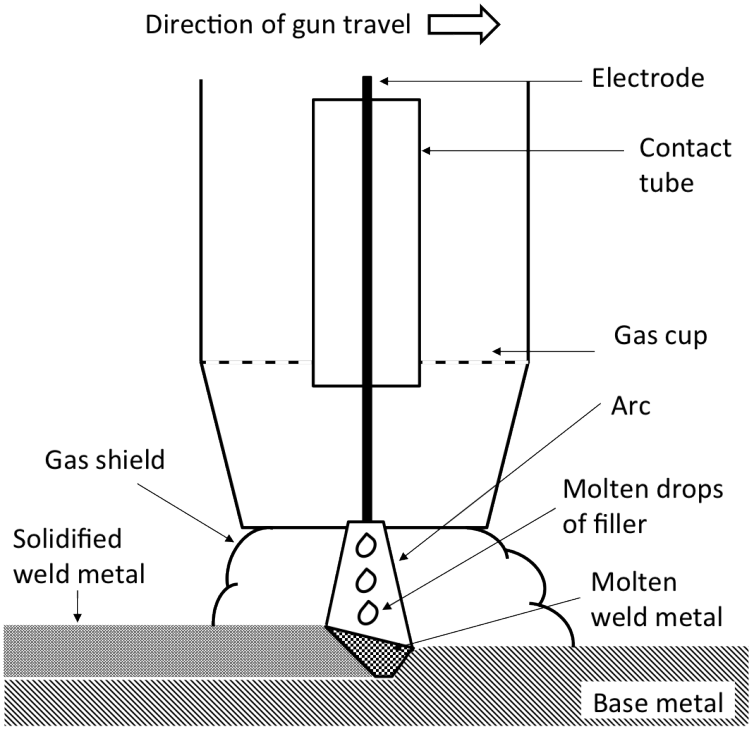

Figure 2.1: Gas-metal arc welding. The shielding gas protects the molten weld metal, which is produced from the consumable electrode [24].

2.3 Welding Residual Stresses

Residual stress is defined as: "*A stress state which exists in the bulk of a material without application of an external load... All stress systems are self-equilibrating; the resultant force and the moment which they produce must be zero.*" [25].

Alternatively, "*that which remains in a body that is stationary and at equilibrium with its surroundings.*" [4].

Residual stresses arise during welding as a result of sharp thermal gradients between deposited weld metal and the parent material being joined. This thermal mis-match, when combined with a constrained assembly, is capable of producing residual stresses that are equal in magnitude to the yield strength of the weld and are limited only by plastic relaxation. Consider the three constrained bars arranged in Fig. 2.2. If the middle bar is heated, it will develop an increasing state of compression resulting from its thermal expansion whilst being restrained by its neighbours, until the yield strength is attained and plastic deformation occurs. On subsequent cooling, the bar contracts and a tensile stress is induced which is retained at ambient temperature and forces the two neighbouring bars into compression equal to half the equivalent stress in the middle bar [26]. This arrangement represents the macroscopic stresses that arise during welding, the centre bar is analogous to the weld metal and the two restraining bars the parent material being joined.

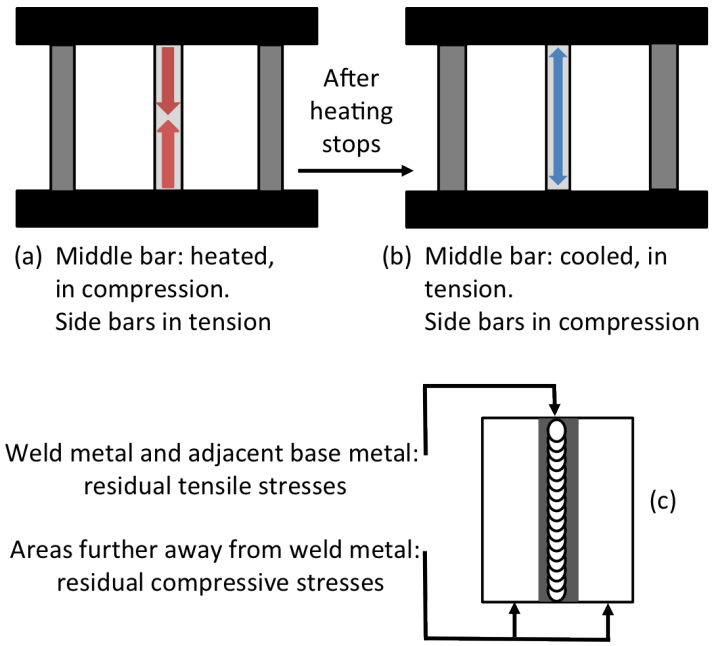

Figure 2.2: Thermally induced stresses in a constrained assembly; (a) heating, (b) cooling, (c) typical residual stresses for a welded component [26].

The changes in stress state as a function of temperature for a welded component are shown schematically in Fig. 2.3. Four sections are taken at different positions along the weld (a) to highlight the temperature change (b) and its

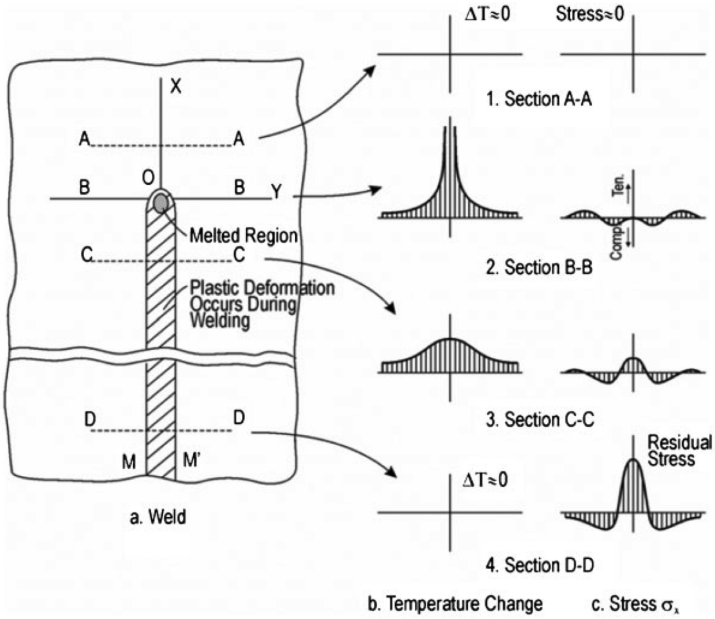

Figure 2.3: Stress as a function of temperature for sections at different positions along a weld; (A–A) pre-weld condition, (B–B) weld pool, (C–C) post-weld cooling, (D–D) post-weld, ambient temperature [5].

effect on stress (c). The hatched area represents the region where plastic deformation occurs. Section A–A is the parent material prior to welding and is positioned suitably away from the weld bead such that there is no heat input or thermally induced stress (assuming the parent material has a zero stress state). Section B–B has the peak temperature and steepest gradient as it cuts through the freshly deposited weld, the stress state directly at the weld pool is approaching zero because it is liquified. The stress profile is comparable to the heating cycle of the constrained bars in Fig. 2.2. The regions adjacent to the weld pool are compressive (centre bar) and the further regions are tensile in order to equilibrate the stress. The stresses developed are significantly lower compared with the final residual stress, this is due to the material's low yield strength at high temperature. During cooling, section C–C, the signs for the stresses reverses compared with the heating stage. As the weld cools it contracts, however, the adjacent material is rigid and will not allow the volume change required. This forces the central region into a state of tensile stress, whilst the outlying regions become compressive. As the weld continues to cool towards ambient temperature, it will also continue to contract in accordance

with its thermal expansivity. The stress levels will increase to a maximum, which is the yield strength of the weld and create a final profile as shown in section D–D. These residual stresses are much higher at room temperature due to the increase in yield strength with decreasing temperature [26–28].

2.3.1 Characterisation & Measurement

Incorporation of residual stress levels and distribution is essential to the safe design and lifing of welded engineering structures. Tensile residual stresses are deleterious to the integrity of an engineering component because they are superposed with the stresses that a structure is subjected to in service, thus promoting the likelihood of unexpected, premature failure. Complexities and variables associated with the welding process make it difficult to predict the final stress state. This is compounded by limitations to measurement techniques that can be destructive, expensive or require *ex-situ* investigation. In many cases it is impossible to measure the residual stresses for a functioning fabrication, especially when they are located deep within the bulk of the material and destructive analysis is not an option.

Prior to summarising the main measurement techniques, it is useful to categorise residual stresses. This is most satisfactorily achieved in terms of the 'length scale of self-equilibration' (or simply length scale) because it provides the necessary information for the correct choice of measurement methods. They are Type I (macrostress), Type II (microstress) and Type III (microstress) as shown in Fig. 2.4 [25, 29].

1. Type I stresses extend over several grains to the macroscopic dimensions of the component. They are typically measured in material removing, destructive examination but also for neutron diffraction experiments with welds.

2. Type II stresses are the order of a grain width or part of a grain in a polycrystalline material, around a few tens of micrometres. They occur between different phases or inclusions.

3. Type III stresses are limited to a sub-grain length scale and typically occur as a result of dislocations, vacancies and interstitials.

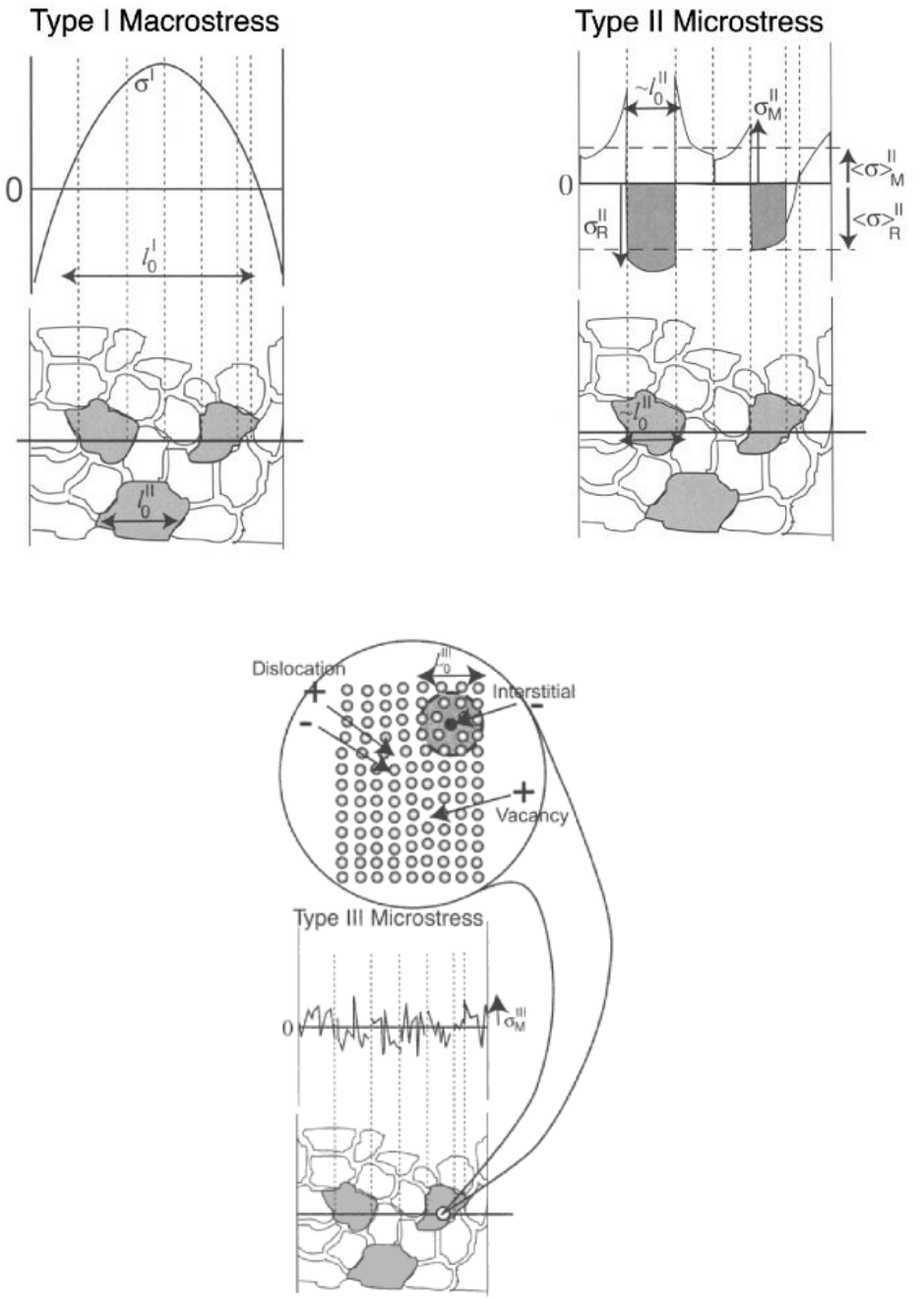

Figure 2.4: Length scales of Type I (l_0^I), Type II (l_0^{II}) and Type III (l_0^{III}) stresses [29].

Measurement techniques can also be classified as destructive or non-destructive. The principle behind the former group involves disruption of the residual stress from its state of equilibrium, generally by material removal to create a free surface, whilst local changes in strain or displacement are measured. The strain values are then used to calculate the original residual stress state. Destructive methods include hole drilling and the more recent contour method [30]; non-destructive techniques include X-ray and neutron diffraction, which essentially use the lattice parameter as a strain gauge [25].

A summary of common practices is highlighted in Table 2.1. No single technique can be universally applied so it is necessary to select the most appropriate method(s) for the material being tested. A powerful technique for strain analysis is neutron diffraction, which complements laboratory X-rays through its ability to penetrate the surface layers into the bulk of specimens. Even so, both procedures adopt the same principle of diffraction.

Through measurement of the distance between lattice planes using Bragg's Law:

$$n\lambda = 2d_{hkl}\sin\theta \tag{2.1}$$

it is possible to determine the residual stresses associated with welded components, where λ is the wavelength of the incident X-ray, d_{hkl} is the lattice spacing for the hkl planes and $\sin\theta$ is the angle between the beam and the planes. Fig. 2.5 shows the effect of strain on the diffraction peak position. In (a) the sample is unstressed and d_0 is the the unstrained lattice parameter. If a tensile stress is applied normal to the diffracting planes then the effect is an increase in width of the planes and corresponding peak shift to a lower angle (b). Non-uniform strain within the gauge volume leads to peak broadening, which can mask peak shifts and affect the final stress measurements [31].

X-Ray diffraction has been embraced industrially as a result of its portability, non-destructive nature and ability to measure surface stresses, which is necessary when estimating the fatigue life of welds. It is, unfortunately, limited by depth of penetration, which is the order of several micrometres in steel. This

Table 2.1: A summary of the various techniques employed for measuring residual stresses in engineering components. The values quoted provide a broad indication of measurement capabilities [3, 29].

Method	Penetration	Spatial resolution	Accuracy
Hole drilling (distortion caused by stress relaxation)	$\sim 1.2 \times$ hole diameter	50 µm depth	±50 MPa, limited by reduced sensitivity with increasing depth
X-ray diffraction (atomic strain gauge)	$<10\,\mu$m or <1 mm (with layer removal)	1 mm laterally; 20 µm depth	±20 MPa, limited by non-linearities in $\sin^2\psi$ or surface condition
Hard X-rays (atomic strain gauge)	∼ 20 mm (Fe)	20 µm lateral to incident beam; 1 mm parallel to beam	$\pm 10 \times 10^{-6}$ strain, limited by grain sampling statistics
Neutrons (atomic strain gauge)	25 mm (Fe)	500 µm	$\pm 50 \times 10^{-6}$ strain, limited by counting statistics and reliability of stress-free references
Ultrasonics (stress related changes in elastic wave velocity)	>10 cm	5 mm	10%
Magnetic (variations in magnetic domains with stress)	10 mm	1 mm	10%
Raman	$<1\,\mu$m	<1 µm approx.	$\Delta\lambda \approx 0.1\,\text{cm}^{-1} \equiv 50$ MPa

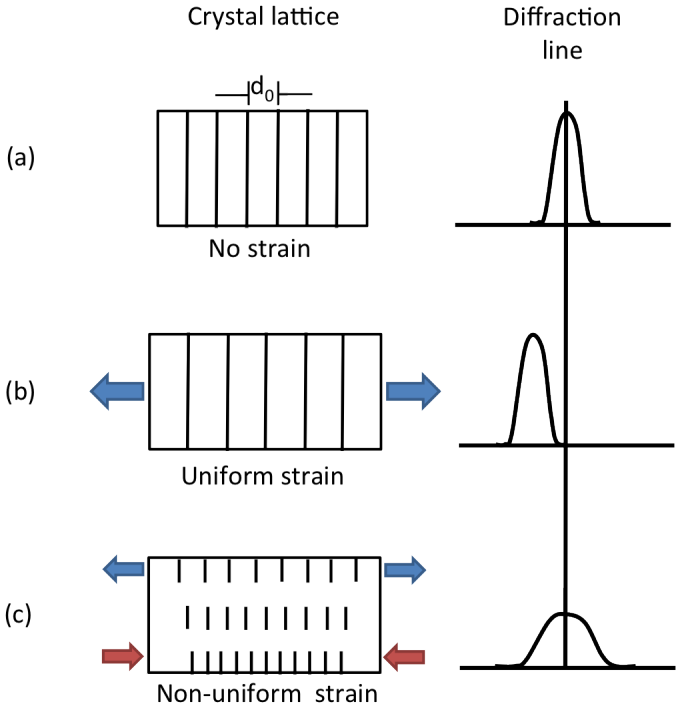

Figure 2.5: The effect of strain on diffraction peaks: (a) unstrained, (b) uniform strain, (c) non-uniform strain [31].

can be improved when incorporated with layer removal but is not ideal. In the context of welds, uneven surfaces and variations in microstructure (texture / large grains) can cause some measurement difficulties but it remains a widely used technique for assessing Type I and II stresses [32].

The primary appeal for using neutrons is their greater depths of penetration. Indeed, it is possible to produce 3-dimensional stress maps to depths of up to 25 mm in steel when measuring through thickness Type I stresses. The disadvantages of neutron experiments is their relative expense, limited access (mostly national facilities) and the extensive data processing required. Errors can arise when measuring lattice spacings due to drastic changes in microstructure and composition across the welded region. Nevertheless, with an ability to provide such unique results they are heavily subscribed for residual stress measurements in welds [33].

2.3.2 Fatigue Performance

As previously mentioned, welding is known to cause distortion, reduced fatigue performance and stress corrosion cracking in joined components. Despite variations in microstructure across the weld, it is the presence of residual stresses that are the major contributors to these problems and the reason why such efforts to measure, predict and control their distribution are employed.

Although residual stresses will affect static loading, it is generally accepted that $\sim 80\%$ of mechanical failures are caused by fatigue and so understanding the relationship between residual stress and fatigue performance is paramount [34]. For structures subjected to fatigue under tension, it is clear that reducing the tensile residual stresses or developing compression is advantageous. This is especially true at free surfaces, which are the usual sites for crack initiation [35]. It is a common industrial practice to grind the crown of the weld flat, this process is performed in order to improve fatigue performance or aid non-destructive evaluation techniques. Grinding will mitigate geometric stress concentration but will inevitably influence the surface residual stress distribution.

The fluctuating stresses that cause fatigue are typically reproduced in the laboratory environment under controlled conditions. This is an idealised situation and produces a completely reversed stress cycle of sinusoidal form, Fig. 2.6a. Both the maximum stress $\sigma_{\max}$ and minimum stress $\sigma_{\min}$ are equal in magnitude and the parameters are defined as:

$$\text{stress range} \qquad \Delta\sigma = \sigma_{\max} - \sigma_{\min} \tag{2.2}$$

$$\text{stress amplitude} \qquad \sigma_{\mathrm{a}} = \frac{\sigma_{\max} - \sigma_{\min}}{2} \tag{2.3}$$

$$\text{mean stress} \qquad \sigma_{\mathrm{m}} = \frac{\sigma_{\max} + \sigma_{\min}}{2} \tag{2.4}$$

where tensile stresses are denoted by a positive sign and compression is negative. For the repeated stress cycle in Fig. 2.6b, $\sigma_{\max} \neq \sigma_{\min}$, thus increasing the mean stress.

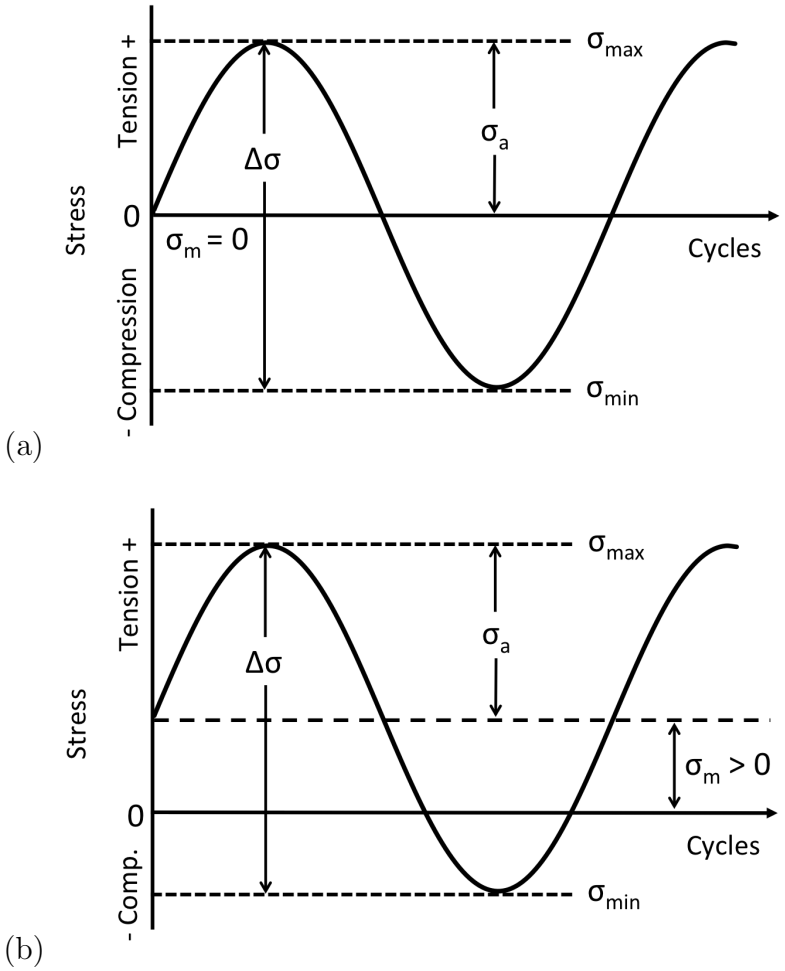

Figure 2.6: Idealised fatigue stress cycles, indicating the stress parameters that affect fatigue life. (a) Reversed stress, zero fatigue cycle: $\sigma_{\mathrm{m}} = 0$ (b) repeated stress, non-zero fatigue cycle: $\sigma_{\mathrm{m}} > 0$ [36].

There is a decrease in fatigue life with increasing mean stress value. This is shown by plotting the stress amplitude from a uniaxial fatigue test as a function of number of cycles to failure, Fig. 2.7a. The effect can also be represented using constant-life diagrams, Fig. 2.7b, one of the most well known being attributed to Goodman. In this case, varying combinations of mean stress and stress amplitude are plotted for a constant fatigue life. If the mean stress is increased by the presence of a tensile residual stress then it follows that there must be a reduction in stress amplitude for the material life to be unaffected. N_f is the number of cycles to failure and $N_{f3} > N_{f2} > N_{f1}$ [37].

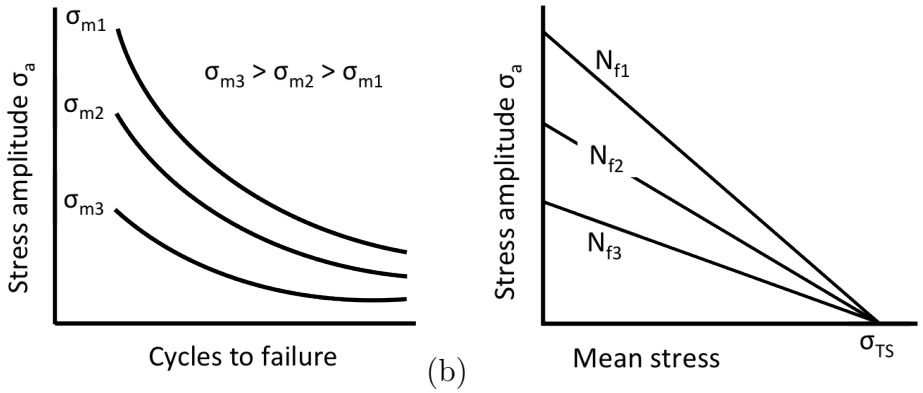

Figure 2.7: (a) The effects of mean stress value on fatigue performance, (b) Goodman constant life curves for fatigue loading with a non-zero mean stress [37].

By virtue of the tensile residual stresses that develop during welding there is an increase in mean stress as the residual stresses are superposed with those applied during service. For this reason, additional processing steps (e.g. shot peening) are often included in component manufacture specifically to introduce surface compressive stresses, which can enhance fatigue performance. Alternatively the harmful tensile residual stresses can be relieved through post-weld thermal treatments. The mean stress has a significant effect on fatigue crack growth, but only during the periods at the onset of crack propagation and high growth rate approaching failure. During stable crack growth (Paris regime), the mean stress is arbitrary, unless it contributes to crack closure [3, 36].

2.4 Martensite in Steels

The role of martensite in steels is often associated with its final mechanical properties, such as increased strength and hardness. It has historically been synonymous with quenching, and rapid cooling is indeed necessary in order to manufacture this phase in low alloy steels. The hard, brittle phase is invaluable for many engineering applications, although it is usually tempered to improve toughness. However, in the context of welding, the formation of martensite is generally undesirable due to its encouragement of hydrogen-induced cracking/cold-cracking. The requirements for this to occur being the presence of hydrogen, residual stress and a 'susceptible' (brittle) microstructure [24].

To embark on the development of a martensitic welding alloy may appear inappropriate, given the inevitable issues that would ensue. Fortunately it is possible to manipulate the toughness through judicious alloying additions and the evolution of martensitic welding alloys with appropriate mechanical properties are discussed in section 2.5. High strength welds are needed to join high strength steel members and the final transformation product will always remain of primary interest. In this particular situation though, the actual transformation mechanism itself is of significant technological interest and can be controlled to provide a useful outcome in the context of residual stress relief [38].

The transformation of austenite (γ) to martensite (α') occurs under non-equilibrium conditions, hence martensite is not represented on the iron–carbon phase diagram. Instead, especially for welds, continuous cooling transformation (CCT) curves are utilised and refer to the phases that will be formed during continuous cooling from the austenite phase field, Fig. 2.8. A relatively rapid quench is required to form martensite where Ae_3 is the the temperature separating the the $\alpha+\gamma$ and γ phase fields, B_{S} is the bainite–start temperature and M_{S} is the martensite–start temperature.

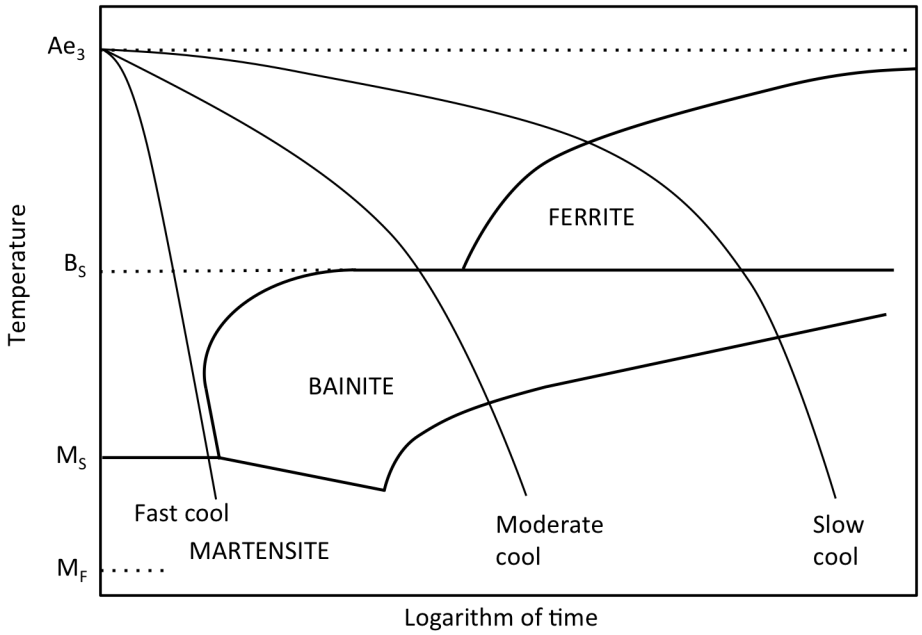

Figure 2.8: A schematic CCT diagram illustrating the effect of cooling rate on microstructure [39].

2.4.1 Transformation Plasticity

The fast cooling rate promotes a diffusionless, displacive transformation, forcing carbon atoms to remain trapped in solid solution and contributing to the increase in strength and hardness [40]. During the $\gamma \rightarrow \alpha'$ transformation there is a homogeneous deformation of the original crystal arrangement into a new structure. This does not involve the bonds being broken. In a reconstructive transformation, bonds are broken and there is a subsequent re-arrangement of atoms into an alternative pattern, Fig. 2.9. Here, the open and closed circles schematically represent two kinds of atoms and their movements for the different types of transformation [28].

The displacement of atoms during the $\gamma \rightarrow \alpha'$ transformation is significant and capable of altering the macroscopic shape of an unconstrained specimen. Experimentally, this can be determined by polishing a surface and observing the change in surface relief during transformation, Fig. 2.10a; scratches on the surface are also displaced. For constrained transformation, the surrounding

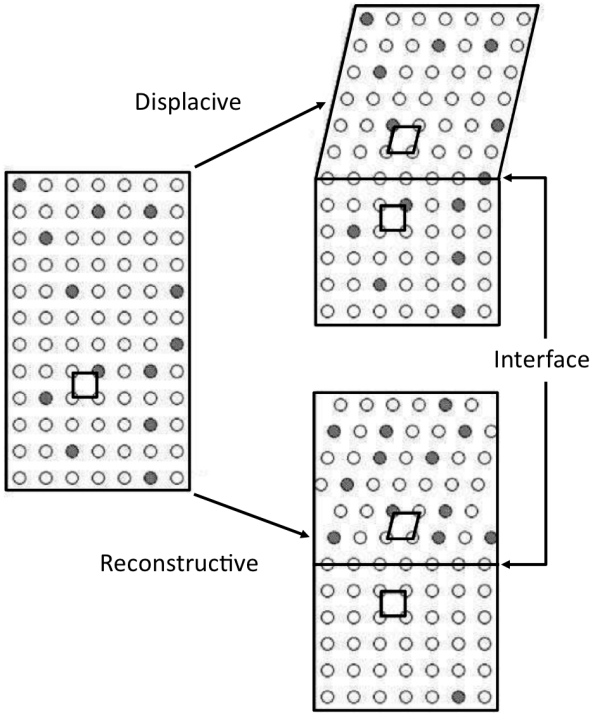

Figure 2.9: Schematic illustration of the difference between displacive and reconstructive transformation, highlighting the co-ordinated movement of atoms and shear displacement. The interface plane can also be referred to as the habit plane [28].

matrix accommodates the shape change through a combination of elastic and plastic strains. The martensite then forms as thin lenticular plates to minimise the elastic strain energy, Fig. 2.10b.

(a) 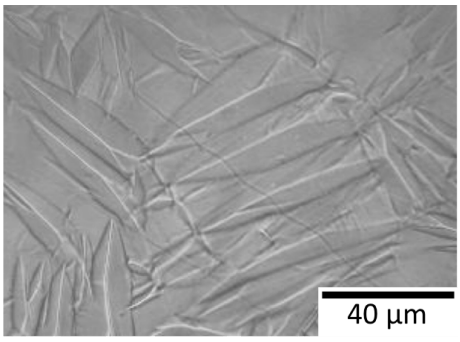

(b) 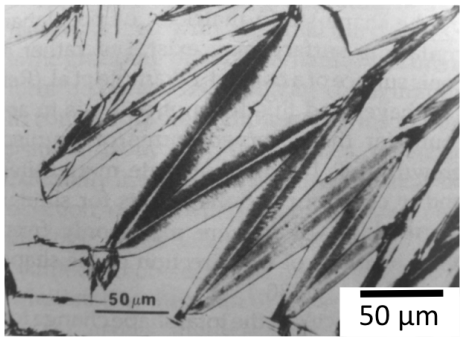

Figure 2.10: (a) Deflection of scratches resulting from martensitic transformation: Fe-0.31C-30.5Ni wt% [41]. (b) Lenticular martensite plates formed in Fe-0.38C-30Ni wt% [42].

The surface displacement is an example of transformation plasticity manifesting on a macroscopic scale and this concept is used as the basis for explaining stress evolution in welded components. It is defined in this work as the irreversible deformation resulting from the solid-state transformation of austenite to martensite but is in reality a complex process that is comprised of several simultaneous events. For both reconstructive and displacive transformations the associated volume expansion influences the residual stress state in a material. This is inevitable during transformation of the parent (face-centred cubic) to the product phases (body-centred cubic) and in the context of welding, is sufficient to alleviate the thermal contraction strains. However, an additional shear component of the martensitic transformation may also contribute to stress reduction in the presence of an applied stress [9].

The crystallographic shapes changes associated with the $\gamma \rightarrow \alpha'$ transformation are shown schematically in Figs. 2.11a–c and belong to a class known as invariant–plane strains (IPS) [38]. The dilatational strain normal to the habit plane $\delta \simeq 0.03$ and the shear component $s \simeq 0.26$ represent the martensitic transformation [43]. These strains are substantial when compared with a typical elastic strain in a metal tested under a tensile load, which is the order of 10^{-3}. The dilatation will always influence strain on a macroscopic level, whereas the shear contribution may only manifest at a crystallographic level depending on the external load. Another aspect of transformation plasticity is the Greenwood-Johnson mechanism [44]. A softer daughter phase (austenite) is plastically deformed by the hard daughter phase (martensite) as it grows during transformation. The consequence of this phenomena is a two-phase aggregate that yields at very low macroscopic stress [45].

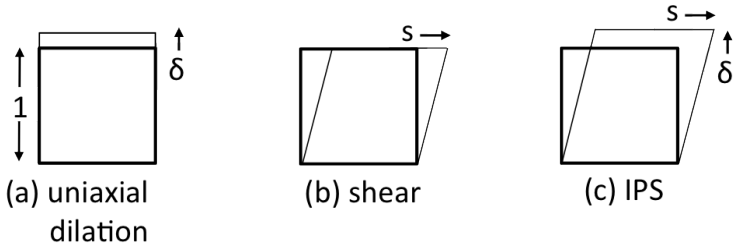

Figure 2.11: Three types of invariant–plane strains that graphically represent the martensitic transformation. [28].

2.4.2 Variant Selection

When austenite transforms to martensite (or bainite) it may produce one or more of 24 crystallographic variants. In the absence of a significant applied stress, the individual shear components tend to cancel each other in a polycrystalline material. In situations of large applied stress below the yield strength of the austenite, variant selection occurs [15, 46]. This permits the large shear strain component s to manifest itself on a macroscopic scale. Fig. 2.12 shows (a) polycrystalline austenite, (b) transforming into randomly oriented plates of martensite for an unstressed specimen. Whereas, (c) acquires texture resulting from variant selection under the influence of an applied macroscopic stress. For a constrained welded member, the latter occurs in an effort to compensate for the thermal contraction strain [10].

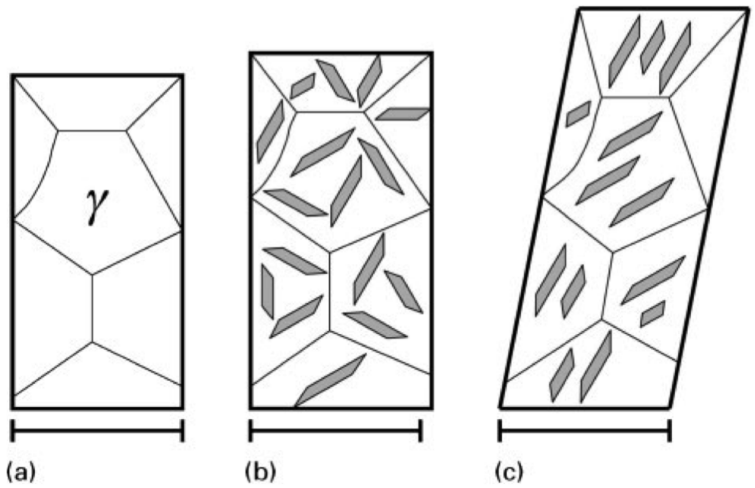

Figure 2.12: Schematic illustration of austenite to martensite (or bainite) transformation in a polycrystalline material; (a) austenite phase, (b) no applied stress: random orientation of plates, (c) applied stress: variant selection [10].

2.4.3 Calculating the Martensite–Start Temperature

The temperature at which the $\gamma \rightarrow \alpha'$ transformation occurs in the weld metal is critical for stress relief. It is therefore necessary to design a welding alloy with both appropriate mechanical properties and a low M_S. This is predominantly achieved through alloying additions and the M_S is strongly dependent on the

content of austenite stabilising elements. The major influence on the M_S is chemical composition, although there are other contributing factors including the prior austenite grain size [47, 48], plastic strain in the austenite prior to its transformation [49] and stress which is present during welding. Shiga *et al.* measured $\sim 30°C$ increase in the M_S for restrained specimens [50].

There are different modelling techniques which can be used to predict the M_S. Several linear regression models have been proposed [51–53]. Those suggested by Andrews [54] and Steven & Haynes [55] are perhaps the most relevant as they are capable of estimating the M_S for both low and high alloy steels. Although both show small deviation from the measured M_S temperatures (the former shows a deviation for high chromium alloys, the latter for high molybdenum alloys) [56].

Thermodynamic [57–59] and artificial neural network models [60–62] have also been developed to predict the M_S temperatures. All such methods provide a reasonable guide during the alloy design stage if they are used within the data boundaries stipulated by the respective model. This includes thermodynamic models where their accuracy is limited by the underlying thermodynamic, empirically obtained database. An excellent critique of the various methods is presented by Sourmail *et al.* [63].

As a result of rapid nucleation and growth of the product phase, the martensite reaction occurs athermally and is effectively independent of time. The volume fraction of transformation product is a function of undercooling below the M_S. This is expressed by the Koistinen and Marburger equation [64]:

$$1 - V_{\alpha'} = V_\gamma = \exp\{\beta(M_S - T_q)\} \tag{2.5}$$

where $V_{\alpha'}$ is the volume fraction of martensite, V_γ is the volume fraction of retained austenite, T_q the temperature below the M_S and $\beta \simeq -0.011$ is a material constant normally quoted for ferrous martensite. It has subsequently been determined that β has a value within the range of -0.0175–0.0190 for low carbon, high chromium/nickel welding alloys [65]. If T_q is set at ambient temperature, it follows that there will be a quantity of retained austenite depending

on the M_S. This is important for the final microstructure. Even at very low undercooling the reaction does not go to completion [66]. The martensite–finish temperature M_F is then conveniently defined as 95% transformation to martensite. Terasaki *et al.* showed the progressive microstructural change to martensite at several different temperatures below the M_S for a welding alloy [67].

2.5 Development of Welding Alloys

In an attempt to refine the modelling of stress accumulation during welding, Jones and Alberry determined that transformation plasticity and temperature contribute significantly to the final stress state of a constrained sample as it cools from the austenite phase [6]. This experimental procedure is used for weld simulation because it apples constraint and measures stress directly. An unconstrained tensile specimen of weld metal is heated above its austenitisation temperature, prior to constraint and cooling, whilst monitoring stress [68, 69]. Fig. 2.13 shows three different types of steels cooling from their austenitic state, with the 2Cr1Mo and 9Cr1Mo samples transforming to bainite and martensite at approximately 600 °C and 500 °C respectively.

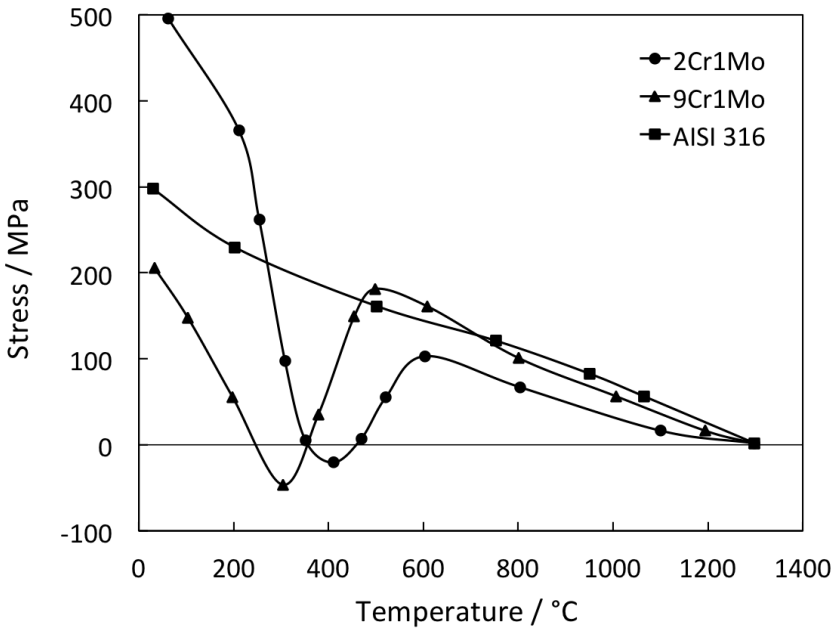

Figure 2.13: Accumulation of stress during cooling of a martensitic (9Cr1Mo), bainitic (2Cr1Mo) and austenitic steel (AISI 316) [6].

The phase transformation start temperature is observed by the sudden decrease in stress, which can be attributed to the dilatation and shear strains that compensate for the accumulated thermal contraction. However, the beneficial offset in contraction strain is negated by continued cooling to ambient temperature after the transformation product has been exhausted. These ob-

servations led to the conclusion that the final stress state (of a welded component) is not only affected by transformation temperature but significantly, it has the potential to be *reduced* by lowering the M_S.

Bhadeshia *et al.* later explained this phenomenon in more detail [38]:

(i) The coefficient of thermal expansion for austenite is greater than that of ferrite. Hence, the volume expansion due to transformation at a lower temperature will be more pronounced. This counteracts the accumulated thermal contraction strains to a greater extent.

(ii) If transformation occurs at a higher temperature, the ferrite formed will have a lower yield strength and be more susceptible to plastic deformation. This will alleviate the thermal contraction strains. As the ferrite continues to cool, its yield strength will increase and allow a greater stress to be sustained. This is indicated by the sharp rise in stress after transformation is complete.

(iii) Variant selection occurs when a displacive transformation occurs under constraint. As a result of increased stress accumulation prior to low transformation-temperature, the shear component will align itself to counter the thermal contraction. This will make a significant contribution in a uniaxially loaded situation.

2.5.1 Initial Fatigue Studies

The concept of transformation plasticity and low M_S welding alloys were further investigated by Ohta *et al.* with the intention of improving fatigue strength through the introduction of compressive residual stresses around the weldment [12, 70]. This would promote crack closure during the load cycle [71]. They successfully designed a new alloy with a composition of 10Cr–10Ni, which reduced the M_S in an unconstrained specimen to approximately 180 °C. The transformation finishes around ambient temperature. Standard welding alloys have a $M_S \sim 500\,°C$ and the profound effects on strain, residual stress and fatigue performance are evident in Figs. 2.14-2.17.

Fig. 2.14 illustrates the changes in strain with cooling for a 'conventional' high M_S welding alloy ε_{HTT} compared with the newly developed low M_S welding

alloy $\varepsilon_{\mathrm{LTT}}$. The relative, final strains resulting from transformation plasticity were pronounced, the low M_{S} alloy had an expansion strain of 0.55 %. Conversely, the conventional alloys tested displayed negative expansion strains at ambient temperature.

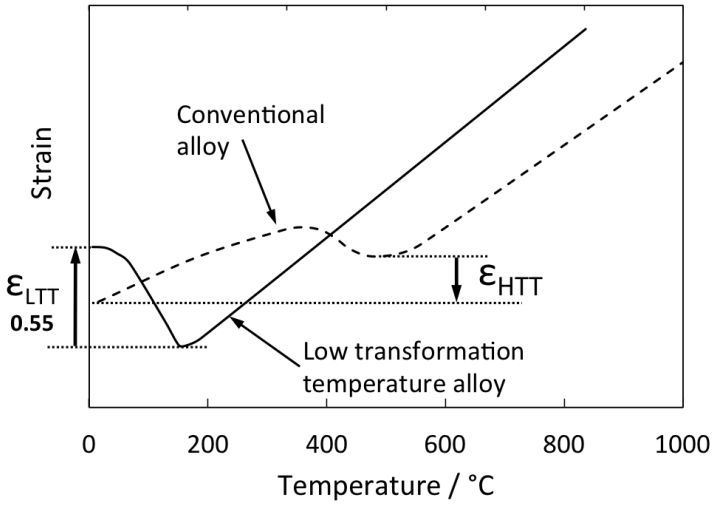

Figure 2.14: Variation of strain with unconstrained cooling for two alloys that have differing M_{S}. The low M_{S} alloy displays a final expansion strain at ambient temperature [12].

The strain results were confirmed by measuring stress as a function of temperature during constrained cooling, Fig. 2.15. Both welding alloys were cooled from the γ–phase and accumulate similar stress levels until the conventional welding alloy begins to transform at around 600 °C. This causes a reduction in stress until around 450 °C when the stress increases again, leaving the specimen in a final state of tension at ambient temperature. The delayed M_{S} for the low transformation temperature alloy drives the specimen in to a state of compression that remains at ambient temperature.

The low M_{S} welding alloy was used to produce cruciform type fatigue specimens. Prior to testing the residual stresses were measured in the vicinity of the weld deposit, Fig. 2.16, and were in agreement with the constrained cooling experiments. The stress values have been extrapolated back to the weld toe, which is the most probable site of failure for a fillet weld under fatigue

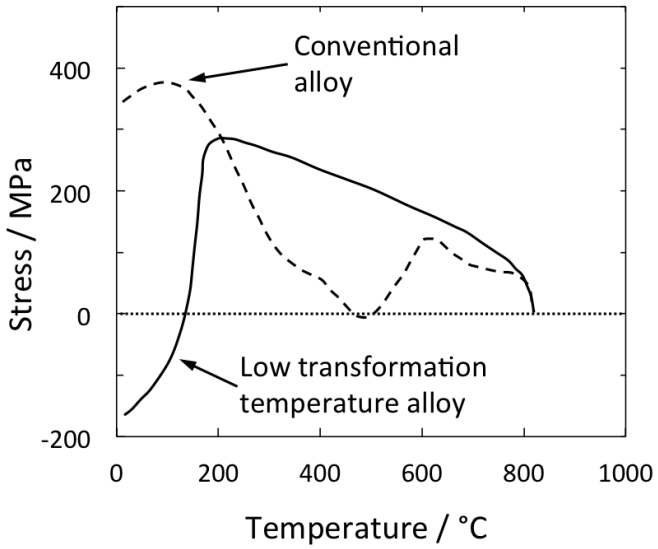

Figure 2.15: Variation of stress for alloys with differing M_S (constrained cooling). The low M_S alloy displayed a final compressive stress at ambient temperature [70].

conditions. The difference between residual stress nearest the weld for the conventional and low M_S alloys is the order of 200 MPa. At the weld toe it could be as much as 600 MPa, although this could be an over-generous extrapolation. However, investigation of the fracture surfaces following fatigue testing revealed crack initiation from blow holes rather than the weld toe, suggesting that the compressive stresses at the toe are sufficient to displace initiation to a more susceptible region.

Fatigue results, the first recorded for these types of low M_S welding alloys, show a marked improvement in fatigue performance, Fig. 2.17. This is achieved through the introduction of compression into the weldment, which reduces the effective stress that the specimen experiences during fatigue testing. The fatigue limit has essentially doubled from 65 MPa to 130 MPa.

Wang *et al.* designed seven different low transformation temperature welding alloys to identify the ideal M_S. They considered that the most favourable alloy was able to induce the maximum residual compressive stress in to the weld bead and henceforth improve fatigue performance [11]. Their approach included the following practical considerations:

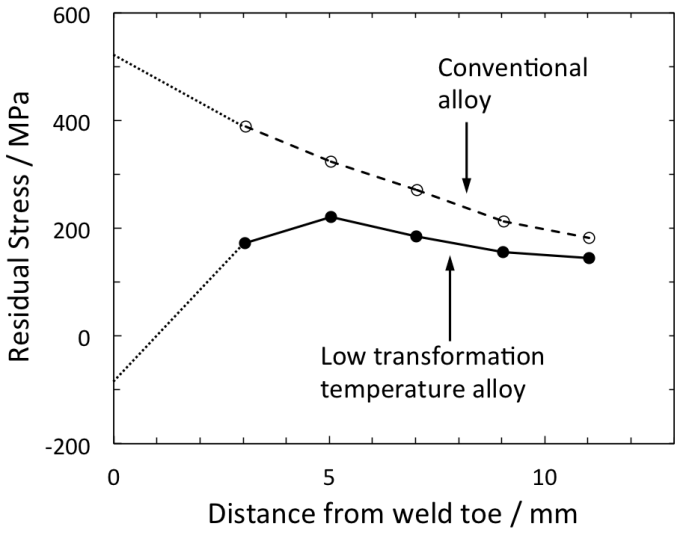

Figure 2.16: Residual stress distributions for cruciform fatigue specimens joined with a conventional and low M_S welding alloy [12].

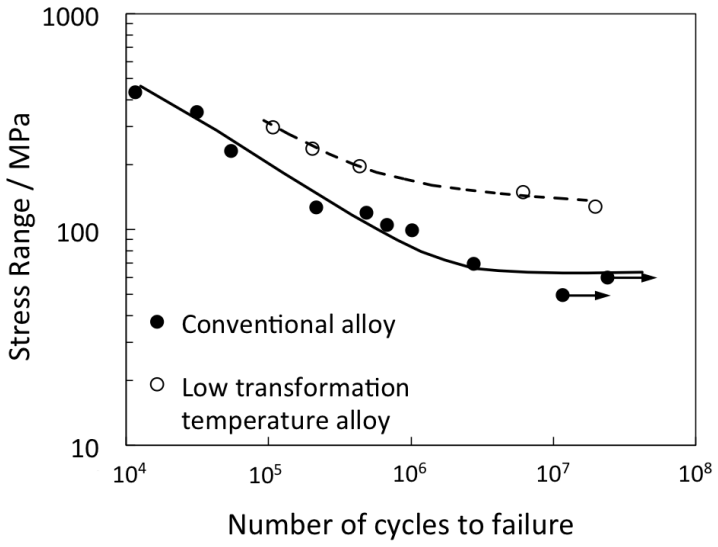

Figure 2.17: S-N curves of conventional and low M_S welding alloys [12].

(i) A low C content (< 0.08 wt%) was essential to reduce hardness and strength, whilst improving toughness and weldability. This also reduced the likelihood of embrittlement that is associated with a martensitic weld microstructure.

(ii) Cr levels were varied (6–12 wt%) to provide a range of reaction start temperatures, $M_S \sim 100$–$300\,^{\circ}C$. However, excessive Cr may have allowed δ-ferrite formation so Ni (5–11 wt%) was added to improve microstructural control.

(iii) Mn and Si were added as deoxidising agents but limited to 2.0 wt% and 1.0 wt% respectively, above certain limits weldability is impaired.

Residual stress measurements were taken from the weld bead using the blind-hole drilling method and the results are shown in Fig. 2.18. The most compressive stresses for both σ_{long} and σ_{tran} were produced by specimen L4 (9Cr–9.5Ni wt%), which had an $M_S = 191\,^{\circ}C$. Wang *et al.* point out three general areas: (1) when $M_S < 100\,^{\circ}C$, the residual stresses are in tension due to incomplete martensite transformation. (2) $M_S \sim 100$–$300\,^{\circ}C$ the weld is in compression. (3) $M_S > 300\,^{\circ}C$ the residual stresses were once again tensile. For both σ_{long} and σ_{tran} the curves bottomed out around $200\,^{\circ}C$ with fairly sharp inclinations either side. This could be fortuitous given that during welding it is difficult to control compositional dilution, which will effect the M_S and residual stresses.

The low M_S specimen, L4, was fatigue tested alongside a conventional welding alloy, L9 ($<$ 0.5Cr–Ni wt%). The results once again proved the low transformation temperature principle. The fatigue performance improved from $\Delta\sigma_{L9} = 113$ to $\Delta\sigma_{L4} = 180$ MPa at 2×10^6 cycles with the stress ratio R = 0.1. The retained austenite in L4 was $\sim 9\%$, as measured by X-ray diffraction.

Following these initial investigations, further fatigue data confirmed that transformation plasticity had become a viable method of controlling residual stress and improving fatigue performance for constant amplitude loading. Eckerlid *et al.* found that crack initiation positions had a tendency to move from the weld toe to the weld root when using a low M_S welding consumable [72]. Darcis *et al.* also recorded crack initiation in the middle of the weld rather than the weld toe [73]. This would suggest that the effects of transformation strain in the weld metal were capable of favourably redistributing the residual stresses at the expected site of crack initiation.

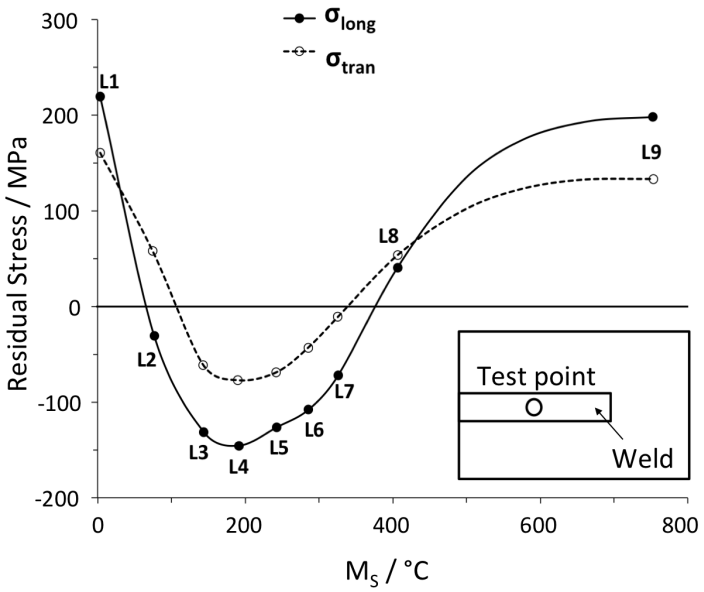

Figure 2.18: Longitudinal and transverse surface residual stress measurements as a function of M_S [11].

One of the motivations for developing self-stress relieving welding consumables was to dispense with expensive post-weld treatments. Ultrasonic peening is one such technique used to surface treat welds and can induce compressive stresses to a depth of 1–1.5 mm in general construction steels [74]. The low M_S concept had by this time proved superior to conventional welding alloys in terms of fatigue performance. This was a considerable achievement but to increase its potential as a viable option for industrial applications the improvements would have to be on a par with current post-weld treatments.

Lixing *et al.* performed a comparative study of fatigue properties for welds joined with a low M_S alloy (LTTE 3) versus conventional welds treated by ultrasonic peening, Table 2.2 [14]. The low M_S alloys showed an improvement versus conventional alloys but not to the magnitude displayed by the post-weld treatment. This could limit the situations where these types of welding alloys could be utilised. There seems to be a lack of literature comparing the effects of transformation plasticity versus specific post-weld treatments, with only one other reference that considered hammer peening [75].

Table 2.2: A comparison of fatigue performance between different welded joints at 2×10^6 cycles [14].

Type of joint	Filler alloy/treatment	$\Delta\sigma$ / MPa
Butt Joint	Conventional filler/no treatment	156
	LTTE 3 filler/no treatment	174
	Conventional filler/ultrasonic peening	234
Fillet Joint	Conventional filler/no treatment	117
	LTTE 3 filler/no treatment	167
	Conventional filler/ultrasonic peening	200

2.5.2 Stress Characterisation Using Neutrons

The principle of improved fatigue performance through using low M_S welding alloys had been established and correlated with limited residual stress measurements determined from destructive techniques such as hole drilling. The next major step in alloy development came through the use of neutron diffraction to create stress maps across the entire section of a weld. These could be superimposed on macrographs to provide an indication of stress contours with the boundaries of the weld bead, heat affected zone (HAZ) and parent material.

Francis *et al.* [21, 76] compared the results of Satoh tests with neutron diffraction experiments for three welding alloys with markedly different M_S, Table 2.3. B_S is the bainite-start temperature. In Fig. 2.19, an unconstrained sample of undiluted alloy is heated above its austenitisation temperature (850 °C for 60 s), prior to constraint and cooling at 10 °C s^{-1}, whilst monitoring stress. The general shapes of the curves have already been described in Fig. 2.13 but they relate the final stress state with the welding alloy M_S. LTTE has the most favourable final stress state with a M_S = 200 °C. The purpose of comparing the results from a constrained, uniaxial Satoh test with the stress maps was to identify any correlation between the residual stress state. Although the information from neutron diffraction is superior, given its ability to determine strain in different orientations the technique has limited access. Whereas Satoh tests are a convenient method for measuring stress when designing new welding alloys.

Table 2.3: Compositions of the base plate (Weldox 960) and undiluted filler alloys in wt%. Included are the estimates M_S and B_S of the conventional (OK75.78) and low transformation temperature alloys (LTTE and Series B) [76].

Material	C	Si	Mn	Cr	Ni	Mo	Cu	M_S / °C	B_S / °C
Weldox 960	0.20	0.50	1.6	0.7	2.0	0.7	0.3	-	-
OK75.78	0.05	0.19	2.0	0.4	3.1	0.6	-	388	421
LTTE	0.07	0.20	1.3	9.1	8.5	-	-	200	-
Series B	0.03	0.65	0.5	1.0	12.0	0.5	-	275	-

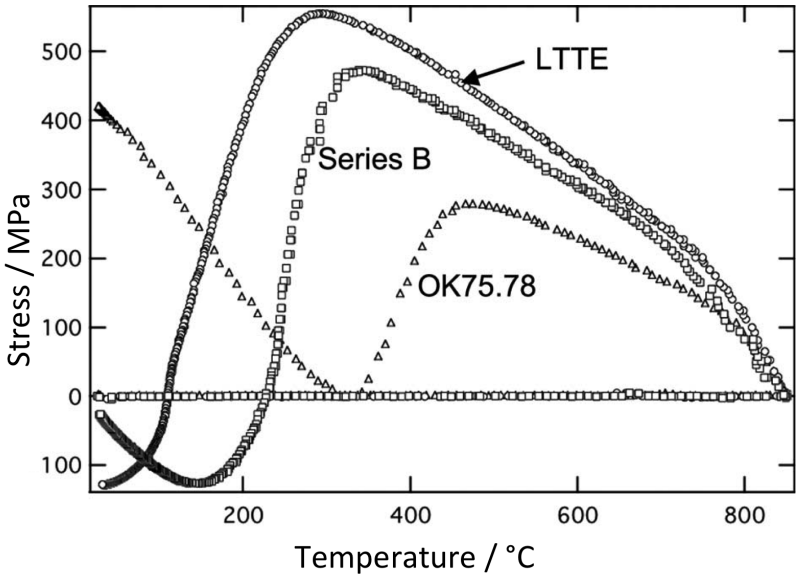

Figure 2.19: Satoh tests conducted on undiluted filler alloys. The final stress state decreases with decreasing M_S [76].

Fig. 2.20 shows the longitudinal stresses across the mid-section of a plate with a single-pass weld deposited along a 5 mm deep V-groove, for the three different fillers. For OK75.78 the weld bead and underlying parent plate display low levels of stress, which rapidly increase (tensile) with horizontal displacement and peak at $\sim$ 800 MPa near the HAZ boundary. The LTTE and Series B welds have major compressive stress in the weld deposit, up to -600 MPa and the inclined stress contours follow its shape. The stress contours are almost vertical for OK75.78. The low M_S alloys show a reduction in peak tensile stress, $\sim$ 600 MPa, similarly adjacent to the HAZ but occupying a much smaller region [21].

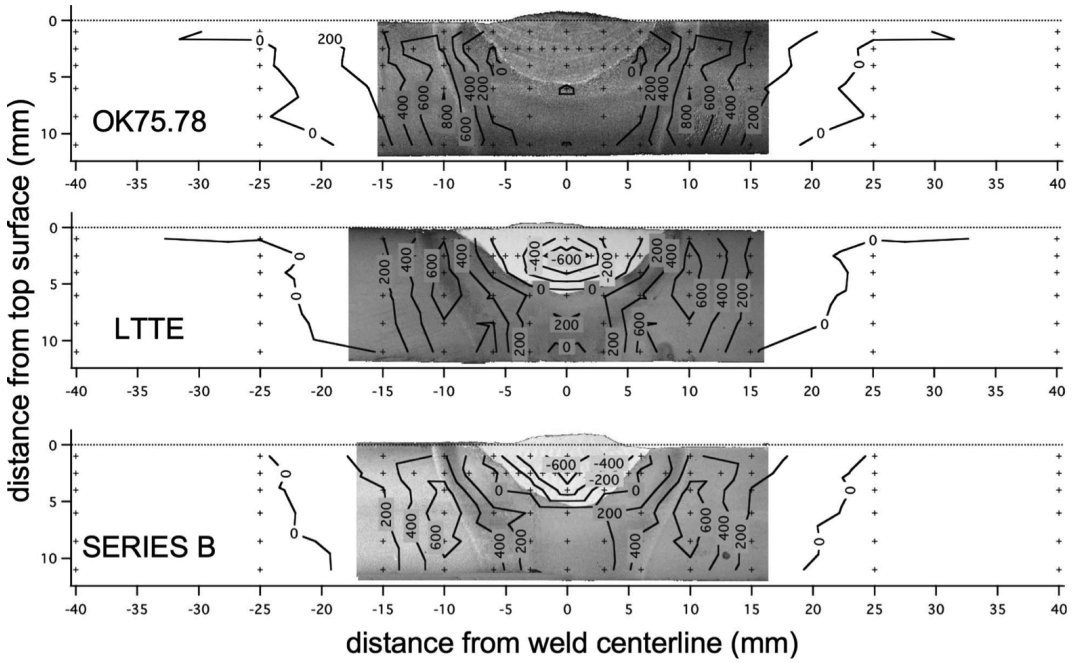

Figure 2.20: Longitudinal residual stresses estimated using neutron diffraction measurement positions marked by crosses. For each weld, the stresses are superimposed on their corresponding macrograph. Measurements have been averaged to reduce scatter, i.e. symmetry has been assumed about the weld centre line [76].

Undoubtedly, the large compressive stresses result from a suppressed M_S as observed in the Satoh tests (Fig. 2.19). It is difficult to ascertain the effects of the M_S on stress distribution between the LTTE and Series B, which resulted in $\sim$ 100 MPa difference in the Satoh test. The variables associated with welding may mask these smaller changes but there is a noticeable shift

in the position of the 600 MPa region towards the surface for the LTTE. This could be counter productive from a fatigue perspective, even though the Satoh tests may suggest that LTTE is at the optimum M_S because it produces the greatest compressive stress. The data acquired from neutron experiments is more informative than uniaxial techniques given its ability to measure the full stress tensor as a function of position in the weld.

Additional transverse and normal stresses were measured, Fig. 2.21. The weld deposit is in compression for both orientations for the LTTE, although the levels are much lower compared with the longitudinal direction. The tensile stresses accumulated in the base material are also lower for the transverse and normal directions. This is perhaps due to lower stress magnitudes being required to equilibrate the compression. However, the difference between OK75.78 and LTTE is substantial for the transverse direction with a peak tensile stress $\sim$ 400 MPa (LTTE) versus negligible stress for OK75.78. This should be considered for welded structures in service when the applied load is in the same direction as the transverse residual stress.

Shiga *et al.* have also performed a neutron diffraction study on two butt welds using low M_S alloys ($9Ni_{eq}$–$13Cr_{eq}$ and $7Ni_{eq}$–$12Cr_{eq}$). Fig. 2.22 shows the longitudinal results compared with measurements for the LTTE alloy (8.5Ni-9.1Cr). Although a direct comparison is not possible due to slight variations in measurement depth, composition and the M_S. The general trends show good correlation with maximum compressive stresses in the weld deposit. There follows a sharp incline in stress as the distance from the weld centreline increases and the measurement position moves towards the heat affected zone and base plate. Eventually the peak tensile stresses subside and tend towards zero, several centimetres away from the weld. It is possible that the fillers developed by Shiga *et al.* would be more beneficial in terms of fatigue performance because of lower peak tensile stresses but no fatigue data exist to validate this theory.

Altenkirch *et al.* recently used neutron diffraction to measure in-situ lattice strains for three low M_S welded specimens (10Cr–8Ni, 10Cr–10Ni, 10Cr–12Ni wt%) as a function of applied load and showed that an increase in load leads to stress induced martensite formation. This is dependent on the amount

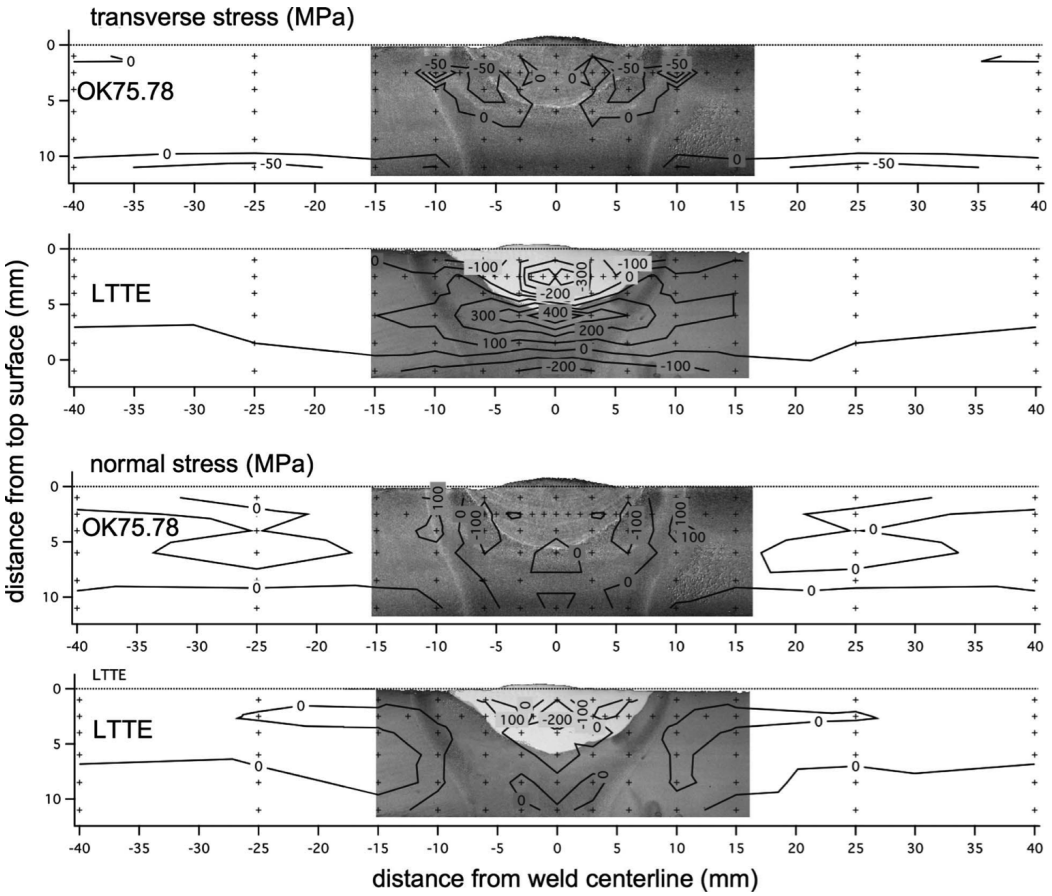

Figure 2.21: Transverse and normal residual stresses estimated using neutron diffraction measurements at locations marked by crosses for conventional (OK75.78) and the low M_S (LTTE) alloy. Stresses are superimposed on the corresponding macrographs [21].

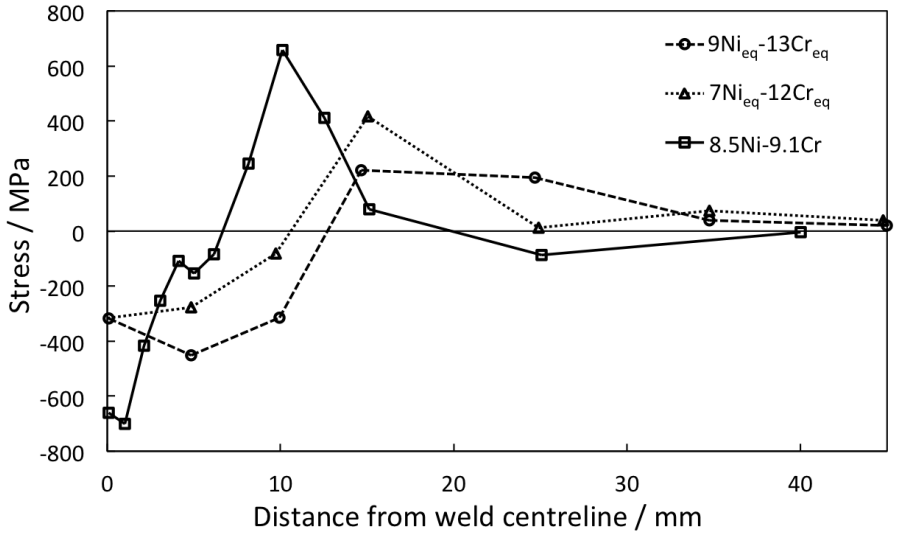

Figure 2.22: Longitudinal residual stresses developed in welds using low M_S alloys as measured by neutron diffraction. The 9Ni$_{eq}$–13Cr$_{eq}$ and 7Ni$_{eq}$–12Cr$_{eq}$ alloys were measured at 2 mm below the surface [50], whilst 8.5Ni–9Cr was measured 2.5 mm below the surface [76].

of retained austenite, which increases with Ni content [77]. The research was focused towards quantification of stress induced transformation of welds with varying fractions of austenite and the influence on mechanical properties rather than on the production of residual stress maps.

2.5.3 Synchrotron X-Ray Diffraction

Alongside neutron diffraction, the use of hard X-rays has become a recognised technique in the determination of residual stresses. Increased depths of penetration are of value, when compared with conventional laboratory X-ray instruments. The main attraction though, is the wealth of time resolved information that can be acquired, rather than final stress state only. Stone *et al.* installed a thermomechanical simulator on a synchrotron X-ray beam line to characterise phases under conditions representative of welding. They were successful in determining the cooling rate dependence of phase transformation and suggested that: phase fractions, texture, lattice parameters and potentially, residual stress, could be collected as a function of cooling rate and applied mechanical constraint [78].

Kromm *et al.* have conducted several investigations on low M_S alloys with variable Ni content, Table 2.4. They have used synchrotron radiation to measure phase specific residual stresses to 150 µm below the surface in a two-pass weld. The results showed that both compressive (in α'-phase) and tensile (in γ-phase) Type II microstresses can coexist at a specific depth, where the macrostress is determined by the phase proportions [79]. Further in-situ investigations confirmed the existence of phase-specific residual stresses and compositional effects on the M_S. Although compressive stresses were found in the austenite phase, which is not in agreement with their initial findings. Welded plates were prepared offline and then installed on the beam line. Phase transitions were observed directly during the re-melting and cooling of the weld using the tungsten inert gas (TIG) technique. An increase of Ni content by 4 wt% was sufficient to decrease the M_S by $\sim 200\,^{\circ}\mathrm{C}$ for the diluted filler. Measurements were taken specifically from the surface regions of the diluted weld metal [80].

Table 2.4: Compositions of the undiluted low M_S fillers used in several investigations [19, 20, 77, 79–84]. The undiluted filler M_S were measured by thermal analysis [81]. The as-welded M_S were measured on the EDDI beam line at the BESSY site, Berlin and highlight the effects of dilution [80].

Alloy	C	Ni	Cr	Mn	Si	M_S / °C	
						Undiluted	Diluted
8 wt% Ni	0.04	8.0	10.0	0.7	0.4	184	268
10 wt% Ni	0.04	10.0	10.0	0.7	0.4	90	125
12 wt% Ni	0.04	12.0	10.0	0.7	0.4	71	39

Additionally, an investigation of sub-surface residual stresses in multipass welds has been concluded, with the intention of further volume characterisation using neutron diffraction [19]. The initial work compares below-surface stresses (up to 100 µm) for two plates (thickness = 6 and 15 mm) to confirm the effect of increased restraint due to multipass welding and thicker sections. The 10 wt% Ni welding alloy (Table 2.4) was used to butt weld the steel plates ($200 \times 150 \times 6 \mid 15$ mm), which had a minimum yield strength of 690 MPa. The interpass temperature was held above 150 °C until the final welding pass was complete.

Fig. 2.23 shows the longitudinal and transverse residual stresses in the subsurface region across the weld and into the base plate for the 15 mm and 6 mm thick samples. Based on the previous neutron data, the results for the 15 mm plate are unexpected. The stress profiles were expected to show compression in the weld deposit, with tensile stresses being manifest towards the HAZ and equilibrating with continuation into the base plate. Instead, both tensile and compressive stresses are evident in the weld. Additionally, the stress range in the transverse direction is greater than the longitudinal, which is unusual. The transverse stress for the 6 mm plate (not shown) followed a similar trend of both compression and tension in the weld as for the 15 mm plate. However, the longitudinal stress became compressive (~ -100 MPa) in the weld and resembled profiles measured by neutron diffraction [50, 76].

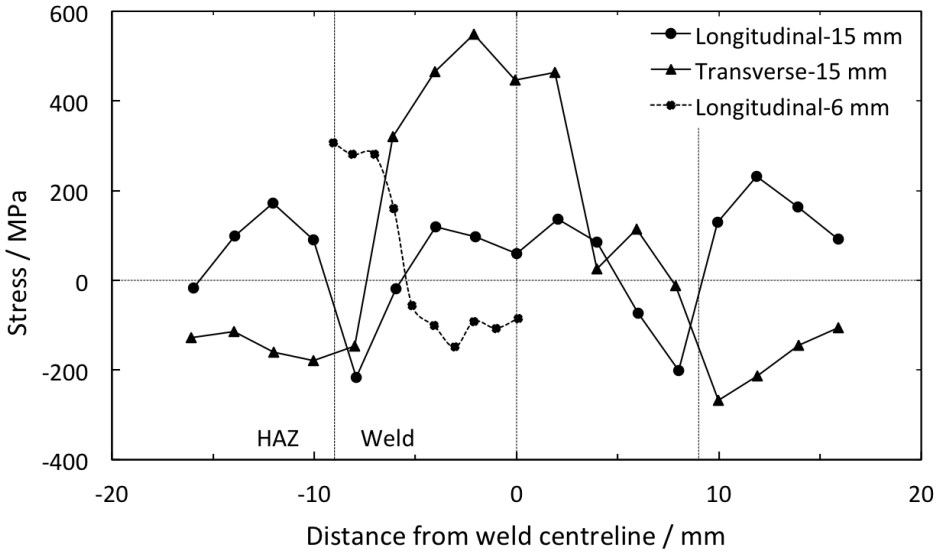

Figure 2.23: The longitudinal and transverse residual stress profiles for two different thickness plates welded with a low M_S filler. The plate thickness were 15 mm (solid line) and 6 mm (dashed line). The weld metal and heat affected zone are indicated for the 15 mm plate only [19].

The apparent disparity in results between those measured by neutron diffraction and hard X-rays has not been investigated further. Also, an explanation has not been fully defined but 'inhomogeneous transformation' has been suggested as the cause of higher surface residual stresses. In thick multipass welds

with larger weld volumes, there will be a temperature gradient between the core and the surface that may lead to delayed transformation between these regions. Initial compressive stresses in the transformed surface may be forced into tension to balance stresses arising from the later transforming weld core [19]. With an interpass temperature of 150 °C, which is sufficiently above the M_S (125 °C), it is possible that this phenomenon could occur.

Altenkirch *et al.* attempted to observe phase specific strain evolution for an in-situ time and temperature resolved welding experiment for low M_S welds. It was partially successful, but unfortunately, specimen shape changes caused by the liquid weld pool during welding limited their ability to collect diffraction data. They also measured the M_S for three alloys of constant Cr content and varying Ni for the pure alloy and weld. There were some major differences between the values, with the measurements from the weld being higher than expected, this was apportioned to texture and dilution resulting from re-positioning of the beam because of the weld pool [83]. Finally, the use of synchrotron residual stress data has been exploited to develop numerical models, considering the effects of varying the M_S / M_f and quantities of retained austenite [84].

The Germany based research groups have focused on 10Cr wt% filler alloys with varying Ni content and their most recent work has concentrated on residual stress and retained austenite measurements in multipass welds. They have produced stress contour plots for a five layer weld using a combination of energy dispersive synchrotron X-ray diffraction (longitudinal/transverse orientation) and neutron diffraction (normal orientation). Contour plots of retained austenite for the three different alloys showed maximum values at the surface. The 8Ni wt% filler had an average quantity of $< 5\%$ in the weld metal whereas the 12Ni wt% filler was $\sim$ 15–20% [20].

A further 17–pass weld was produced to investigate the effects of restraint on strains measured at the surface using X-ray diffraction [85]. The weld was created while the base plate was being held rigid in a hydraulic rig to ensure controlled restraint. Strain gauges in the equipment measured the reaction force as each weld layer was deposited. It was shown that stress relief occurs

due to the $\gamma \rightarrow \alpha'$ transformation for each individual layer. The amount of stress reduction was dependent on the volume of material transforming. The transverse residual stresses were dictated by the applied restraint.

Finite Element Modelling

The measurement of residual stresses in welded assemblies is challenging and not always possible, especially in large structures. It is more efficient to predict the evolution of stresses and the results from diffraction based experiments contribute to the refining of these models. A material's physical and mechanical properties such as: heat capacity, thermal expansion coefficient, density and strength all influence the final stress state. Finite element software should account for all of the processes that occur during welding including transformation plasticity. Combining this phenomenon to existing stress accumulation models was the original intent of Jones and Alberry and is pertinent to simulating the behaviour of low M_S welding alloys. Authors that have been involved in researching this topic are in agreement that the solid-state transformation of $\gamma \rightarrow \alpha'$ must be included in predictive models and that the temperature of occurrence should be accounted for [86–88]. Stress measurements made by neutron diffraction have been used to validate algorithms [89, 90]. Thomas *et al.* used the angular distortion of welded plates to confirm predictions [91]. Whilst Yamamoto *et al.* calculated stress build up in welded specimens, which they then manufactured and fatigue tested [88].

In particular the variant selection and its impact on residual stress should be incorporated in to simulations [92]. Takahashi *et al.* used electron backscatter diffraction to compare the variants that dominate during welding for two different geometries [93]. Neutron diffraction confirmed a reduction in residual stress as a result of the martensitic transformation. They proposed that variant selection was dependent on the weld geometry. For a butt weld, all 24 of the available variants were almost randomly selected. For a cruciform type weld, a few variants were preferentially chosen based on higher residual stresses generated by this weld geometry.

2.5.4 Latest Fatigue Studies

Extensive fatigue studies have been conducted by Karlsson *et al.* using a range of low M_S alloys on both butt and fillet welds [18, 94, 95]. Their latest work includes three sets of welds with the compositions and predicted transformation temperatures shown in Table 2.5. The parent plate was a 900 MPa high strength ferritic steel. LTT-C is a high Cr alloy, designed for stainless steel applications [16], LTT-S has extraordinarily high alloying additions to account for dilution and OK Autrod 89 is a standard high strength welding alloy. The element concentration of welds is significantly lower than the initial pure alloy material. Dilution levels vary between $\sim$ 25–35% for single-pass and $\sim$ 10% for two-pass welds [18].

Table 2.5: Compositions (wt%) and predicted transformation temperatures for two low M_S (LTT-C and LTT-S) fillers and a conventional high strength filler (OK Autrod 89). The compositions are for the undiluted weld metal. The M_S/B_S predictions are for the as-welded alloys [18].

Alloy	C	Si	Mn	Cr	Ni	Mo	M_S / °C	B_S / °C
LTT-C	0.014	0.7	1.27	13.4	6.1	0.07	281	-
LTT-S	<0.02	<1	<2	15-18	6-8	<2	221	-
OK Autrod 89	0.09	0.8	1.9	0.3	2.2	0.6	416	544

Fig. 2.24 clearly highlights dilution effects and the improvements in fatigue performance that can achieved by designing an alloy to counter them. $\Delta\sigma$ at 2×10^6 cycles is doubled from $\sim$ 75 MPa (OK Autrod 89) to $\sim$ 150 MPa (LTT-C) and increased almost threefold $>$ 200 MPa for LTT-S. The dilution effect on fatigue is considered to be a result of the M_S change influencing residual stress rather than microstructure.

Previous fatigue studies have concentrated on constant amplitude loading, which may not be representative of structures that are subjected to uneven cyclic loading and peak stresses. For this reason Barsoum *et al.* conducted both constant and variable amplitude fatigue testing on a low M_S alloy [96]. Fatigue strength improvement was measured in terms of mean stress at 2×10^6 cycles. During constant amplitude loading, the low M_S alloy showed $\sim$40%

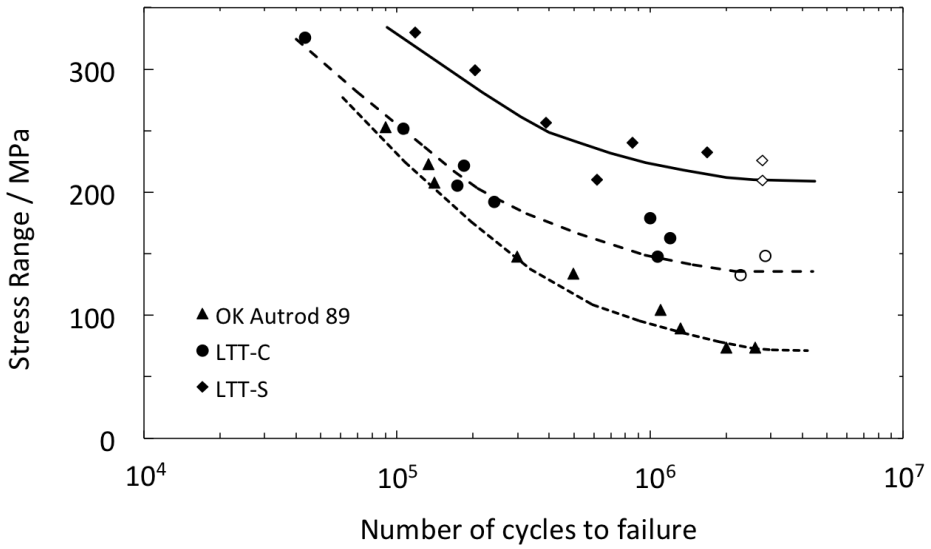

Figure 2.24: Fatigue results for three single-pass fillet welds. The LTT-S specimen provides evidence for improved fatigue performance through designing an alloy to account for dilution. Open symbols represent specimens that did not fracture [18].

improvement compared to a conventional alloy. For variable amplitude loading the improvement was only $\sim 12\%$. It was suggested that the decrease in performance is caused by relaxation of the compressive stresses under variable conditions that leads to a reduction in crack closure. Stress levels were measured 1–2 mm from the weld toe at 50,000 and 600,000 cycles to confirm this theory. As with Karlsson *et al.*, all of the fatigue specimens fractured at the weld toe, Fig. 2.25, which is in contrast with Ohta *et al.* who identified a few failures at blow holes. This would suggest that stress concentration is still a dominating factor in fatigue failure.

Miki *et al.* have also performed variable amplitude fatigue tests and shown that a low M_S filler improves fatigue life [75]. This was part of a large-scale study to understand the effects of a low M_S welding alloy when repairing fatigue-cracked joints in steel bridges [97]. Repairs to the girder around the cracked regions showed improvement when compared with a conventional weld filler. The use of these types of fillers is also relevant to welding sheet steel and improvements have been shown [98]. However, relatively high levels of carbon were used to depress the M_S and this would not be appropriate for most applications. Zhao

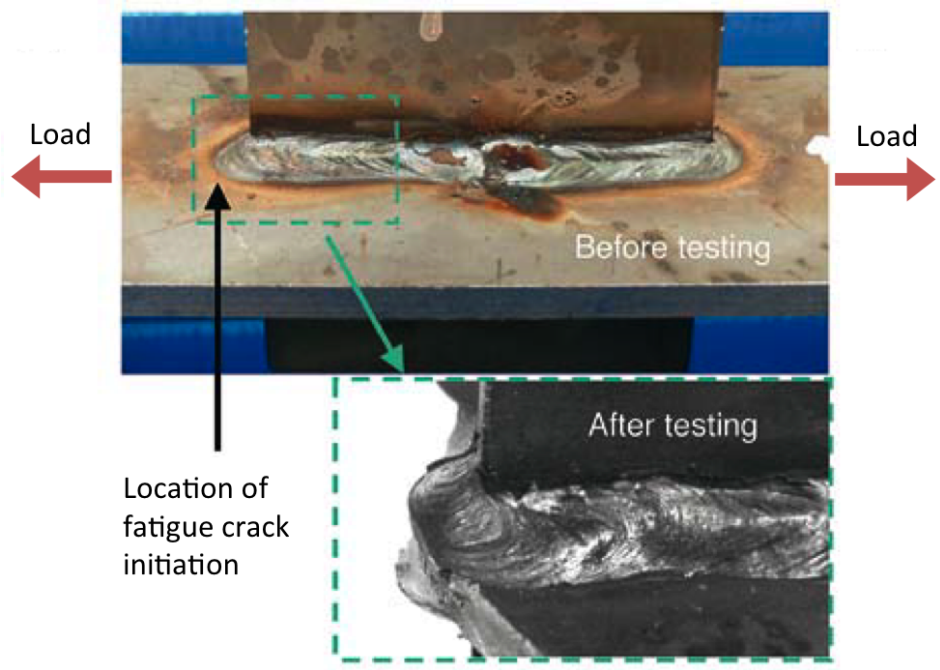

Figure 2.25: Fillet weld fatigue test specimen. Load is applied along the longitudinal direction and fracture ordinarily occurs at the fillet weld toe. The enlargement highlights the fracture surface at the weld toe [94].

et al. have perhaps conducted the most novel research on these types of fillers. In an attempt to enhance fatigue behaviour they spray coated welded joints with a low M_S alloy powder [99]. Their fatigue results were promising for this initial study.

2.5.5 Microstructure and Properties

Given the evidence for the fatigue enhancement of low M_S welding alloys, it is also necessary to understand the compositional effects on microstructure, mechanical properties and cracking. In order to adequately suppress the M_S and ensure a fully martensitic structure at room temperature, large quantities of γ–stabilizing alloying elements are included. As a result of rapid cooling, the Schaeffler diagram, Fig. 2.26, is commonly used to estimate the final structure of weld fillers. This is based on the alloying elements, which are appropriated in terms of Cr or Ni equivalent:

$$\text{Cr equivalent} = (\text{Cr})+2(\text{Si})+1.5(\text{Mo})+5(\text{V})+5.5(\text{Al})+1.75(\text{Nb}) \\ +1.5(\text{Ti})+0.75(\text{W})\,\text{wt\%} \tag{2.6}$$

$$\text{Ni equivalent} = (\text{Ni})+(\text{Co})+0.5(\text{Mn})+0.3(\text{Cu})+25(\text{N})+30(\text{C})\,\text{wt\%} \tag{2.7}$$

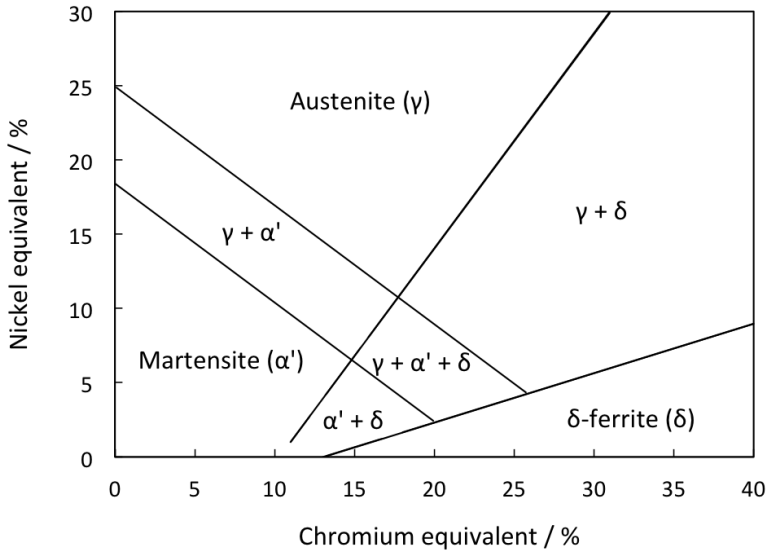

Figure 2.26: The Schaeffler diagram can be used to estimate the effects of alloying elements on the final microstructure of welds with Cr–Ni additions [28].

The principal alloying elements used to control the M_S are C, Cr, Ni, Mn, Si and to a lesser extent, Mo. Other additions are generally $< 0.05\,\text{wt\%}$, with carbon also being kept to a minimum, whilst chromium and nickel are the major influences. Although chromium is a α–stabilizer, quantities in excess of 12Cr wt% may be added when the Ni equivalent content is $\sim 6\%$. Using chromium to decrease the transformation temperature allows the filler to be 'stainless' in nature. Electrochemical testing has shown no detriment to corrosion resistance when using these types of fillers to join stainless steel base plates [100]. However, a low carbon content is required to prevent chromium carbide formation during the re-heating of underlying layers for multipass welds. Chromium depletion at the grain boundaries would lead to inter-granular cor-

rosion. This should not be a problem because low carbon levels are a primary concern and necessary to avoid the formation of hard, brittle martensite and susceptibility to hydrogen-assisted cold cracking.

It is standard practice to apply a pre-heat in order to prevent this phenomenon [24]. Zenitani *et al.* investigated this issue with cracking tests to ascertain if the compressive stresses developed in the weld could reduce susceptibility. The alloy compositions, hardness and M_S are in Table 2.6 and the results from the crack tests are in Fig. 2.27. Microscopy revealed mostly martensite for welds A and B, whilst C contained martensite and bainite, this is consistent with hardness values and suggests that cracking might occur preferentially in A and B. This was not the outcome and implies that the reduced susceptibility to cracking is due to residual stress reduction [101]. Based on these results Kasuya *et al.* conducted a more detailed analysis on a singular low M_S filler (W-1), measuring the hydrogen content and preheat required to avoid cracking [102].

Table 2.6: Compositions (wt%), hardness and measured M_S of alloys used in crack tests [101].

Alloy	C	Si	Mn	Ni	Cr	Mo	Hardness / HV	M_S / °C
A	0.05	0.25	0.73	8.80	10.10	0.30	366	210
B	0.06	0.28	0.55	4.40	9.90	0.40	386	312
C	0.09	0.52	1.18	1.76	0.60	0.31	334	436

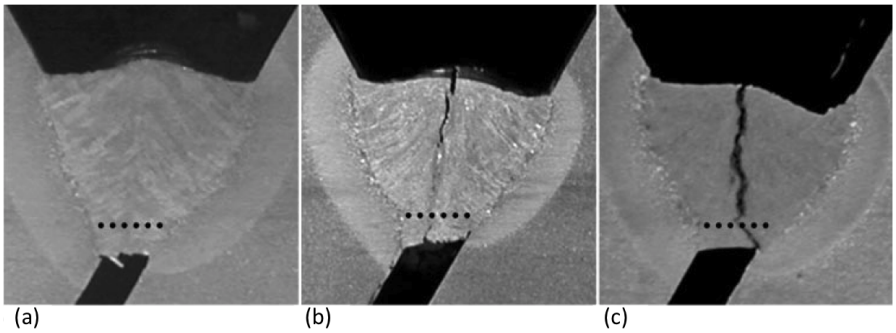

Figure 2.27: Sections of welds following crack testing; (a)→(c) is increasing M_S [101].

Maintaining tough welds is of paramount importance and for this reason nickel has proved a popular choice to lower the M_S. However, high levels of Ni have raised concerns regarding segregation, hot cracking and cost. Although, segregation of Cr, Ni and Mn have been observed in multipass welds [103]. Kromm *et al.* designed three filler alloys with varying nickel compositions and following microscopy and hardness inspection revealed an increase in segregation as Ni content increased. Fortunately, this could be reduced in re-heated zones when additional layers of weld metal were deposited [79]. Other workers [21, 73] have designed low M_S welding alloys with nickel as the major constituent but toughness levels were not significantly improved over fillers with a Cr–Ni combination.

Manganese is a more cost effective alloying addition and attempts have been made to design a filler based on this element with silicon present to improve the weld deposit morphology [104]. Unfortunately, martensitic Fe–Mn alloys can be quite brittle [105]. This probably stems from co-segregation of manganese and phosphorous to prior austenite grain boundaries [106]. Impurity elements such as sulphur and phosphorus should be minimised while elements like molybdenum and tungsten can be included depending on application. For example if pitting corrosion is to be prevented. Micro-alloying elements such as titanium and niobium can be used to control the nitrogen content.

There already exists considerable experience in the field of stainless steel welding fillers and research has shown that the solidification mode can influence susceptibility to hot cracking. If the alloy solidifies as δ-ferrite there is a greater resistance to hot cracking, the reverse being the case for alloys that solidify entirely as austenite. Designing a filler that retains a small quantity of discontinuous δ-ferrite in the weld deposit is thought to enhance toughness properties [16]. If excessive amounts of δ-ferrite remain and a continuous network forms, the impact toughness decreases and the ductile/brittle transition temperature increases [107]. A finer grain size also contributes to improved toughness. The austenite grain size is finer when transformed from δ-ferrite compared with austenite formed directly from the molten weld metal [108].

The focus of alloy design has so far been restricted to joining ferritic steels. Shirzadi *et al.* refined existing commercially available martensitic stainless steel fillers to weld austenitic stainless steels. They specified a design criteria to achieve this goal and proved the principle through distortion measurements [16]. Dilution must also be accounted for when welding austenitic stainless steel plates, which have higher alloying concentrations than the welding alloy. This will lower the M_S such that transformation may not occur. Fig 2.28 shows the first pass of a low M_S alloy on an austenitic stainless steel, the microstructure remains austenitic, compared with subsequent passes that were martensitic.

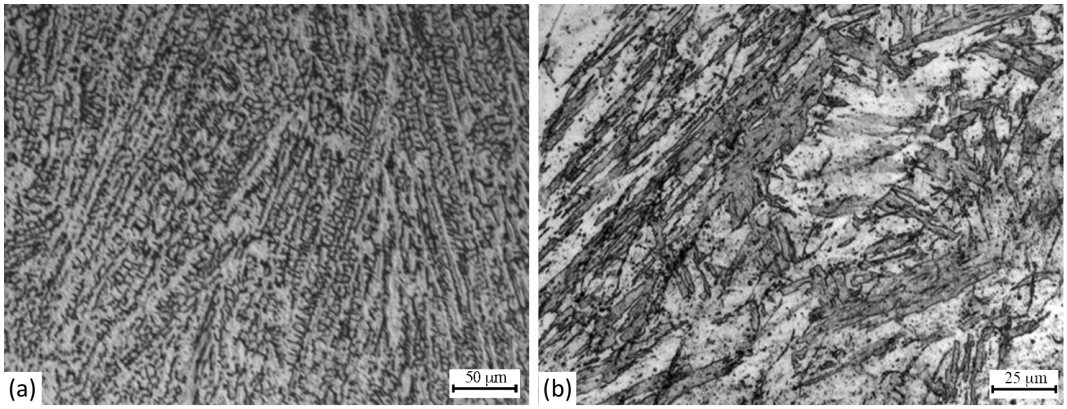

Figure 2.28: Microstructures from a low M_S multipass weld deposited on an austenitic stainless steel; (a) austenitic dendrites, only observable in the first pass due to dilution effects, (b) martensitic structure evident in subsequent passes [109].

Thibault *et al.* measured the residual stresses across a stainless steel plate welded with a low M_S welding alloy [110]. Compressive stresses were evident in the final layers of the weld deposit as measured by both neutron diffraction and the contour method. A subsequent post-weld heat treatment was effective in reducing the peak tensile stresses that developed in the HAZ from 534 to 136 MPa. The benefits in compression were concurrently sacrificed from −426 to −152 MPa (maximum values). Other workers showed that low M_S welding alloys are capable of reducing angular distortion for ferritic base plates [111]. Moat *et al.* added parameters for welding ferritic steels, Table 2.7 and showed a reduction in residual stresses for a stainless steel welding alloy (13Cr–6Ni wt%) using neutron diffraction techniques. The concept of using a low M_S filler has

also been applied to joining dissimilar low carbon steel pipes with low alloy steel forgings [112].

Table 2.7: Low M_S weld alloy design criteria [17].

	Stainless alloy	Ferritic alloy
(i)	$M_S \approx 200 \pm 50\,^{\circ}\mathrm{C}$	$M_S \approx 200 \pm 50\,^{\circ}\mathrm{C}$
(ii)	Fully austenitic at high temperatures	Fully austenitic at high temperatures
(iii)	Transformation exhausted at ambient tempeature	Transformation exhausted at ambient temperature
(iv)	Charpy impact energy $\geqslant 27$ J at $-20\,^{\circ}\mathrm{C}$	Charpy impact energy $\geqslant 27$ J at $-20\,^{\circ}\mathrm{C}$
(v)	Solidify as delta ferrite to limit susceptibility of hot cracking	
(vi)	Maintain stainless character (> 13 wt%Cr)	

A wide variety of alloying additions have been investigated to optimise the fatigue properties and microstructure of low M_S welding fillers, a summary is provided in Table 2.8. Mechanical properties are in Table 2.9.

Table 2.8: Chemical compositions (wt %) and M_S of low transformation temperatures welding fillers from various sources.

Welding alloy	C	Si	Mn	Cr	Ni	Mo	M_S / °C	Ref.
10Cr–10Ni	0.025	0.32	0.70	10.0	10.0	0.13	180	[12, 70, 71]
L2	0.04	0.17	0.27	11.69	10.01	0.04	80	[11]
L3	0.04	0.17	0.30	10.51	9.62	0.05	138	[11]
L4	0.07	0.23	1.25	9.10	8.46	0.50	191	[11]
L5	0.08	0.17	1.35	7.78	6.88	0.06	242	[11]
LTTE	0.07	0.20	1.30	9.10	8.50	-	200	[21, 76]
Series B	0.03	0.65	0.50	1.00	12.0	0.50	275	[17, 21, 76]
B206	0.01	0.40	1.80	12.5	6.70	2.50	<150	[72, 96]
Tubrod 15.55	0.01	0.40	1.80	12.5	6.70	2.5	<150	[72, 96]
13Cr/LC35	0.04	0.50	0.80	12.3	7.30	2.20	<150	[72]
A	0.05	0.25	0.73	10.1	8.80	0.30	210	[101]
B	0.06	0.28	0.55	9.90	4.40	0.40	312	[101]
C	0.09	0.52	1.18	0.60	1.76	0.31	436	[101]
D	0.047	0.40	1.50	11.1	8.60	0.30	94	[101]
A6	0.08	0.19	0.89	14.7	0.27	0.04	360	[73, 103]
B5	0.04	0.19	0.86	13.0	1.70	0.04	300	[73, 103]
C5	0.05	0.22	0.41	3.00	13.2	0.35	270	[73, 103]
Alloy 1	0.01	0.73	1.50	12.9	4.00	0.06	327	[16]
Alloy 2a	-	0.70	1.70	13.6	5.90	0.01	216	[16]
Alloy 2b	0.014	0.76	1.36	12.66	5.24	0.10	-	[16]
Camalloy 4	0.01	0.73	1.50	13.0	6.00	0.06	-	[109]
LTTW (a)	0.04	0.32	0.36	-	11.9	-	420	[89]
H077	0.01	0.80	1.20	12.5	6.80	1.50	214	[90]
LTTW (b)	0.046	0.22	0.69	11.05	9.51	0.296	122	[88]
XTT8	0.04	0.26	0.56	7.60	10.0	0.47	209	[113]
XTT10	0.05	0.21	0.61	5.90	7.80	0.50	295	[113]
LTTE1	0.04	0.17	0.27	10.69	10.01	0.04	79	[14]
LTTE2	0.04	0.17	0.30	10.5	9.62	0.05	144	[14]
LTTE3	0.07	0.23	1.25	9.10	8.46	0.05	191	[14]
8% Ni	0.04	0.04	0.70	10.0	8.0	<0.02	184	[19,
10% Ni	0.04	0.04	0.70	10.0	10.0	<0.02	90	20, 77,
12% Ni	0.04	0.04	0.70	10.0	12.0	<0.02	39	79–84]
LTTW (c)	0.02	0.39	0.19	9.76	10.14	0.17	205	[111]
LTT-C	0.014	0.70	1.27	13.4	6.10	0.07	281	[18, 95]
LTT-S	<0.02	<1.0	<2.0	15-18	6-8	<2.0	221	[18]
WM	0.02	0.34	0.48	12.5	3.80	0.47	-	[110]
W-1	0.052	0.67	0.72	15.6	7.00	-	-	[102]
Butt WJ	0.084	0.41	1.66	12.5	6.05	0.29	-	[93]
Box WJ	0.10	0.34	1.50	14.8	7.11	0.22	-	[93]
LTTW (d)	0.037	0.376	1.30	8.90	8.74	0.235	-	[100]
C15N / LTT	0.029	0.15	0.19	15.66	7.07	-	250	[75, 97]
1	0.20	0.15	2.00	10.0	5.00	1.75	100	[91]

Table 2.9: Mechanical properties of low M_S welding fillers from various sources.

Welding alloy	0.2% PS / MPa	UTS / MPa	Elong. / %	Impact toughness / J					Ref
				-40 °C	-30 °C	-20 °C	0 °C	20 °C	
10Cr–10Ni	822	1192	36	-	-	48	-	-	[70]
B206	700-850	950-1050	>15	>100	-	-	-	>110	[72, 96]
13Cr/LC35	680	1050	15	30	-	-	-	36	[72]
A6	500	624	-	-	-	-	8	10	[73]
B5	886	1002	-	-	-	-	12	14	[73]
C5	702	1155	-	-	-	-	14	14	[73]
Alloy 2b	838	1069	17.6	-	-	53	-	72	[16]
LTTE	1135	1287	6	-	17	15	-	20	[21]
Series B	∼1100	-	-	-	22	27	-	28	[21]
C15 N / LTT	614	1117	-	-	-	-	-	-	[75, 97]
LTT-C	736	1127	13	49	-	-	14	14	[18]
W-1	976	1106	17	35	-	32	35	-	[18]

2.6 Summary

The exploitation of transformation plasticity associated with the austenite–martensite reaction has led to the development of a range of martensitic welding alloys. The purpose of these fillers is to self-relieve the harmful tensile stresses that accumulate during cooling of constrained weld metal to ambient temperature. This is achieved through macroscopic dilatational and shear strains during solid-state transformation that compensate for the thermal contraction strains. The temperature at which the austenite transforms to martensite dictates the final stress state and must be sufficiently low to prevent further thermal contraction strains after transformation is exhausted. However, if the temperature is too low, then the transformation will not be sufficiently complete to counter the thermal stresses.

Manipulation of the chemical composition has led to the creation of a variety of low transformation temperature welding alloys which have different martensite-start temperatures. Uniaxial constrained cooling tests of the pure filler have shown that a $M_S \approx 200\,^{\circ}\mathrm{C}$ produces the maximum stress alleviation. The fillers have been used to manufacture butt welds and cruciform fillet welds for laboratory fatigue testing. Based on the correlation between residual stress and fatigue performance, stress analysis has been conducted using both destructive and non-destructive methods. This has been in order to evaluate the residual stress distributions at the surface and in the bulk of the weld deposit and surrounding regions. Advances in diffraction techniques have allowed the full stress tensor of a weld section to be recorded and mapped.

Specimens welded with low M_S fillers indicate compressive stresses in the weld metal when measured by neutron diffraction. These are usually balanced by tensile stresses found in the heat-affected zone. Surface stress measurements conducted using X-rays have revealed peak tensile stresses in the weld deposit that appear contradictory to the neutron diffraction results. However, fatigue testing of welded samples consistently shows a significant improvement in fatigue performance when joined with low transformation temperature fillers. The margins of improvement over 'conventional' higher M_S fillers are reduced when variable amplitude testing criteria are employed. Not enough data exists

to categorically state the magnitude of fatigue improvement subject to these conditions. The effects of post-weld treatments on fatigue performance of conventional fillers are superior to the effects of transformation plasticity for low M_S fillers with no treatment.

Microstructural control is essential for maintaining mechanical properties, especially toughness. Parameters have been introduced to design welding alloys for ferritic and stainless applications to ensure the correct solidification mode and to address issues sensitive to welding such as hot and cold cracking. Many of the compositions investigated satisfy the M_S criteria but fail to produce an acceptable microstructure. The effects of composition and other influences on the M_S are known and has allowed the development of models based on thermodynamics and empirical data. Dilution with the base material must be considered and laboratory measured M_S can differ substantially from actual welds. This is pertinent to the alloy design because fatigue improvements are based on residual stress levels, which are dictated by the M_S. Dilution effects have been identified and countered by using highly concentrated alloys and proved through fatigue studies. Also, a quantity of retained austenite will always be present, depending on the M_S.

Most research has concentrated on proving the principal of these types of fillers through single-pass welds. The few experiments focused on multipass welds have shown that reheating of deposited layers effects the final stress state. There has not been a systematic evaluation of stress accumulation with additionally deposited layers. Thermal cycles of additional welding passes may not provide sufficient heat to retransform previous welding passes into the γ-phase and allow further stress mitigation. It is necessary to correlate residual stress state in a welded component with fatigue performance for safe design. Now that low M_S fillers are available with appropriate mechanical properties there is a necessity for a more comprehensive understanding of stress accumulation during cooling and transformation of multipass welds. Specifically, the magnitude and location of stresses that will determine fatigue properties.

Chapter 3

Experimental Procedures

3.1 Alloy Characterisation

Two low M_S welding alloys were selected in order to manufacture welded plates for residual stress assessment using neutron and X-ray diffraction. They were based on the nominal compositions referred to in the literature [18] as 'LTT-C' and 'LTT-S'. LTT-C is a stainless steel welding alloy, which could be used to join both ferritic and austenitic stainless steels. The toughness levels displayed were relatively high for these types of fillers and the estimated M_S is appropriate for LTT behaviour such that transformation plasticity would be fully exploited at ambient temperature. LTT-S is a more highly alloyed stainless steel filler, which was designed to correct for dilution of the weld metal when joining ferritic base plates. Following dilution, the filler will assume a composition equivalent to LTT-C. Both of the alloys, when used to join fatigue specimens, displayed improvements in fatigue performance. For the purposes of this work LTT-C and LTT-S are referred to as LTT-1 and LTT-2 respectively.

Specimens of the undiluted LTT-1 and LTT-2 alloys were prepared from a buttered, multilayer butt weld, Fig. 3.1. Buttering is a preparatory step commonly used to produce all-weld test specimens, the joint faces are initially coated with a filler to avoid mixing between the main welding alloy and parent material. The welding process employed was metal-cored arc welding (MCAW), which is a variant of gas-metal arc welding (GMAW) and uses a tubular consumable

filled with the powdered alloy rather than a solid consumable filler wire. No pre-heat was applied and the interpass temperature was 140–150 °C. Mechanical test specimens were cut from the 18-pass welds as shown in Fig. 3.2.

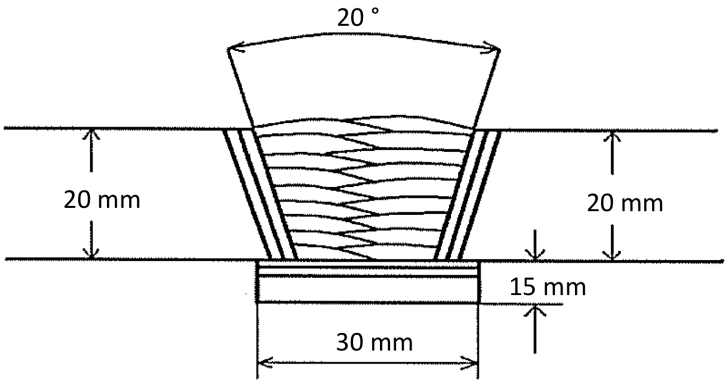

Figure 3.1: Schematic cross-section of the 18-pass weld used to produce the undiluted specimens of LTT-1 and LTT-2. The initial buttered layers are represented by the near vertical lines that follow the incline of the base plate faces [114].

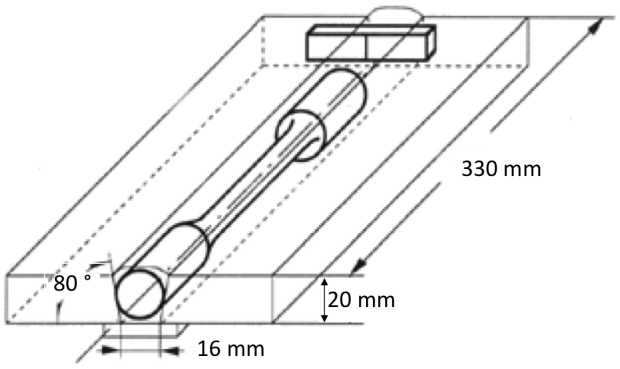

Figure 3.2: Tensile and impact toughness specimens were cut from the undiluted region of the weld [114].

Compositions of the LTT-1 and LTT-2 fillers are in Table 3.1, along with two commercially available welding wires (HTT-1, HTT-2) and base plate materials. The compositions of the low-transformation temperature fillers (LTT fillers) were measured from the undiluted region of the weld. The values quoted for the commercial fillers are typical of the all-weld metal and supplied by the manufacturer. The elemental concentrations of the LTT fillers and base materials were also determined by the manufacturer. BP700 and BP960 are high

Table 3.1: Compositions (wt %) of the undiluted welding alloys and base plate materials used for residual stress assessment.

Alloy	C	Si	Mn	Cr	Ni	Mo	P	S	V	Nb	Cu	Al	Ti	O	N
Low transformation temperature fillers															
LTT-1	<0.02	0.6–0.8	1.2–1.7	12–13	5–6	<0.1	0.008	0.009	0.008	0.010	0.026	0.029	0.040	0.026	0.005
LTT-2	<0.02	<1	<2	15–18	6–8	<0.1	0.019	0.009	0.090	0.012	0.047	0.014	0.008	0.027	0.016
Commercial fillers															
HTT-1	0.10	0.53	1.25	0.58	2.40	0.71	0.010	0.010	-	-	-	-	-	-	-
HTT-2	0.10	0.90	1.50	-	-	-	<0.025	<0.025	-	-	-	-	-	-	-
Base materials															
BP700	0.15	0.29	0.98	0.25	0.043	0.15	0.007	0.001	0.027	0.020	0.006	0.035	0.013	0.002	0.005
BP960	0.17	0.22	1.24	0.20	0.052	0.65	0.008	0.001	0.037	0.016	0.016	0.061	0.002	0.002	0.006
BP355	0.16	0.26	0.95	0.012	0.017	0.006	0.039	0.043	0.008	0.017	0.022	0.005	0.001	0.011	0.005

strength, quenched and tempered martensitic steels, whilst BP355 is a low strength steel. The mechanical properties of the LTT alloys are in Table 3.2, along with the conventional fillers and base materials.

Table 3.2: Mechanical properties of the undiluted welding alloys and base plates used for residual stress assessment.

Alloy	0.2% PS /MPa	UTS /MPa	Elong. /%	Impact toughness /J	
				-40 °C	-20 °C
LTT-1	627	1111	14.0	43	45
LTT-2	319	845	31.8	77	88
HTT-1	>890	940–1180	18.0	72	-
HTT-2	470	560	26.0	-	90
BP700	>700	780–930	14.0	>69	-
BP960	>960	980–1150	12.0	>40	-
BP355	>355	-	-	-	-

The M_S of the undiluted welding alloys were calculated as a function of chemical composition, Table 3.3. The thermodynamic model [115], which combines MTDATA [116] and the PLUS database, was not designed to account for the very high quantities of nickel and chromium that are present in LTT-2. A neural network [61] and several empirical formulae [54–56] were also used to predict the M_S and dilatometry was then performed on the LTT samples to validate the different calculation methods.

Dilatometry

Cylindrical samples of length 12 mm and diameter 8 mm were cut by electro-discharge machining from the undiluted region of the weld with the specimen length parallel to the longitudinal direction. A 0.1 mm gauge Type S platinum/platinum–10% rhodium thermocouple was spot welded to the specimen. The M_S was measured by dilatometry using a Thermecmaster-Z thermomechanical simulator. Samples were austenitised under vacuum conditions by heating to 850 °C for 60 s. They were cooled at a rate of $10\,^{\circ}\mathrm{C\,s^{-1}}$ whilst measuring radial dilation as a function of temperature. Helium was used to quench the samples and all experiments were conducted without constraint.

Table 3.3: Predicted M_S of undiluted welding alloys.

Calculation method	M_S / °C			
	LTT-1	LTT-2	HTT-1	HTT-2
Thermodynamic				
Okumura *et al.* [115]	240	-	410	450
Neural network				
Sourmail *et al.* [61]	121 ±27	31 ±33	389 ±24	435 ±24
Empirical				
Andrews [54]	217	151	404	451
Steven *et al.* [55]	175	93	407	464
Kung *et al.* [56]	169	87	403	457

3.2 Manufacture of Welded Plates

A total of 13 welds were produced for residual stress evaluation as a function of the following variables: base plate, filler, deposition sequence, pre-heat and interpass temperature, Fig. 3.3. They were categorised to assess the effects of:

1. Multiple welding passes (A–D).
2. Interpass temperature (K, L).
3. Dilution of the filler with the base plate (E–G).
4. Base plate strength relative to the filler (M, N).
5. Reference fillers with a high M_S (H, J).

The base material was prepared from $500 \times 150 \times 15$ mm plates and machined with a 60 °, 8 mm deep V-groove along the long direction with a root radius of 4 mm, Fig. 3.4. The plates were clamped to the bench prior to mechanised gas-shielded metal arc welding (GMAW), which was performed horizontally in the down hand position. Details of the welding parameters are in Table 3.4. The welding speed was dependent on the particular pass number and constant across the entire range of fillers used. Diffraction experiments were performed on the welded plates in their as-received condition, i.e. no mechanical or chemical surface treatments.

Weld	Base plate	Welding alloy and deposition sequence		Pre-heat / ºC	Interpass temperature / ºC
A	BP700	LTT-1	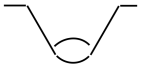	54	-
B	BP700	LTT-1 LTT-1		50	111
C	BP700	LTT-1 LTT-1 LTT-1		55	125 113
D	BP700	LTT-1 / LTT-1 LTT-1 LTT-1		48	125 / 125 110
E	BP700	LTT-1 LTT-1 LTT-2		52	125 103
F	BP700	LTT-2 LTT-2 LTT-2		55	123 117
G	BP700	LTT-2 HTT-1 HTT-1		50	118 124
H	BP700	HTT-1 HTT-1 HTT-1		55	119 120
J	BP700	HTT-2 HTT-2 HTT-2		54	125 122
K	BP700	LTT-1 LTT-1 LTT-1		45	49 50
L	BP700	LTT-1 LTT-1 LTT-1		200	240 240
M	BP960	LTT-1 LTT-1 LTT-1		50	114 108
N	BP355	LTT-1 LTT-1 LTT-1		53	120 112

Figure 3.3: Welds produced for residual stress measurements.

(a)

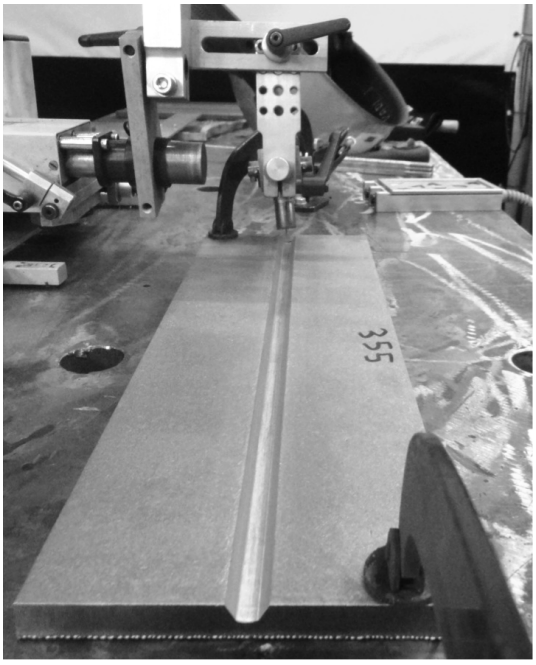

(b)

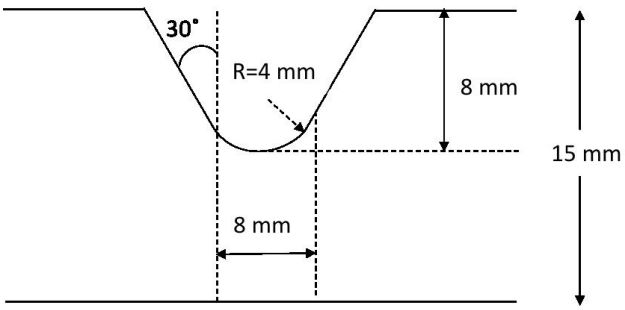

Figure 3.4: (a) Base material clamped in position and ready for automated welding (b) cross-section of the machined V-groove.

Table 3.4: Welding parameters.

Alloy	Wire type	Voltage / V	Current / A	Shielding gas	Heat input / kJ mm^{-1}	Welding speed / cm min^{-1}
LTT-1	Metal-cored	24.7	∼250	Ar+2% CO_2	∼1.0	Pass 1=36
LTT-2	Metal-cored	26.2	∼250	Ar+2% CO_2	∼1.0	Pass 2=30
HTT-1	Metal-cored	29.0	∼250	Ar+18% CO_2	∼1.5	Pass 3=23
HTT-2	Solid	29.0	∼260	Ar+18% CO_2	∼1.5	

Microstructural Analysis

One 10 mm thick section was removed from each welded plate by electro-discharge machining. Specimens were prepared for metallographic inspection, hardness testing and compositional analysis by grinding and polishing to a 1 μm surface finish. The specimens were etched prior to investigation using a solution of 2% nital to etch the ferritic base plate and ferric chloride to etch the stainless weld metal.

Composition Analysis

Energy-dispersive X-ray (EDX) spectroscopy was used to measure compositional changes across the weld with a JEOL 5800LV microscope. Quantitative analysis of the Si, Mn, Cr, Ni alloying additions in the weld deposit was performed with an electron probe microanalyser (EPMA). The electron beam was set at 20 KeV to measure the Kα energy transitions with a 1 μm spot size. The instrument used was a Cameca SX100 and the calibrant materials: Zircon (Si), Cr (Cr), Mn (Mn), NiO (Ni), Fe (Fe).

3.3 Neutron Diffraction – Stress Evaluation

Residual stresses cannot be measured directly but are calculated from the strains. As mentioned previously, diffraction techniques utilise the crystalline lattice as an atomic strain gauge, Eqn. 2.1. The presence of a tensile/compressive stress forces the interplanar spacing, d_{hkl}, within individual grains that are orientated to fulfil diffraction conditions to expand/contract. If the distance between planes of atoms is known when no stress is acting, $d_{0,hkl}$, it follows that the elastic strain can be determined:

$$\varepsilon_{hkl} = \frac{d_{hkl} - d_{0,hkl}}{d_{0,hkl}} \tag{3.1}$$

Stress σ and strain ε are tensor quantities and related to each other by the elastic stiffness C and elastic compliance tensor S:

$$\sigma_{ij} = \sum_{k,l} C_{ijkl}\varepsilon_{kl} \quad \text{and} \quad \varepsilon_{ij} = \sum_{k,l} S_{ijkl}\sigma_{kl} \tag{3.2}$$

where σ and ε have 3×3 components, but due to symmetry only 6 are independent. C and S are $3 \times 3 \times 3 \times 3$ tensors but are also symmetric and may have up to 36 independent components. Therefore, the measurement of strain is required in many directions at a single point in a sample before the stress can be inferred. However, most engineering investigations are based on isotropic continuum mechanics. Therefore, C can be expressed with just two independent components, Young's modulus E and Poisson's ratio ν. For such materials the generalised Hooke's law relationships between stress and strain may be expressed as:

$$\sigma_{ij} = \frac{E}{(1+\nu)}\left[\varepsilon_{ij} + \frac{\nu}{(1-2\nu)}(\varepsilon_{11} + \varepsilon_{22} + \varepsilon_{33})\right] \tag{3.3}$$

where i, j = 1, 2, 3 indicate the components relative to a chosen axes set. From this expression it is evident that the strain tensor must be obtained first. The six components to be measured are expressed in terms of the direction cosines l, m and n made with the orthogonal sample axes:

$$\varepsilon(lmn) = l^2.\varepsilon_{11} + m^2.\varepsilon_{22} + n^2.\varepsilon_{33} + 2lm.\varepsilon_{12} + 2mn.\varepsilon_{23} + 2nl.\varepsilon_{31} \tag{3.4}$$

and produce a system of six linear equations that can be solved. This process can be further simplified through symmetry considerations that assume the likely orientation of the principal stress and strain direction. Following this procedure, the measurement requirements are reduced to just the 3 orthogonal principal strains [29]. For a welded plate the measurement directions are:

$$\begin{aligned}
\sigma_{xx} &= \frac{E}{(1+\nu)}\left[\varepsilon_{xx} + \frac{\nu}{(1-2\nu)}(\varepsilon_{xx} + \varepsilon_{yy} + \varepsilon_{zz})\right] \\
\sigma_{yy} &= \frac{E}{(1+\nu)}\left[\varepsilon_{yy} + \frac{\nu}{(1-2\nu)}(\varepsilon_{xx} + \varepsilon_{yy} + \varepsilon_{zz})\right] \\
\sigma_{zz} &= \frac{E}{(1+\nu)}\left[\varepsilon_{zz} + \frac{\nu}{(1-2\nu)}(\varepsilon_{xx} + \varepsilon_{yy} + \varepsilon_{zz})\right]
\end{aligned} \tag{3.5}$$

where X Y and Z are illustrated in Fig. 3.5 and henceforth termed transverse, longitudinal and normal respectively.

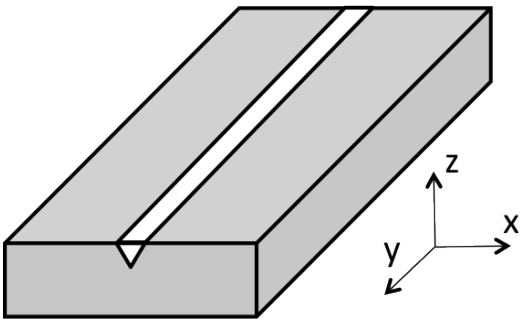

Figure 3.5: Schematic of a welded plate with a reference coordinate system where X, Y and Z are the transverse, longitudinal and normal orientations with respect to the plate geometry.

3.3.1 Measurement Positions

Strain scanning was performed across a plane perpendicular to the weld direction at the position along the plate shown in Fig. 3.6a. Also included are the X-ray and 'comb' sample locations, which are explained later. Three different neutron facilities were utilised (ISIS, FRM II, Chalk River) and by adjusting the experimental set-up, strain data could be collected from the bulk or surface of the welds. Strain measurements were taken on both sides of the weld and heat affected zone, with extension into the parent plate to identify any asymmetry in the stress fields, Fig. 3.6b. The diamonds represent the original locations that were used to determine the stresses within the bulk of the welds. These were slightly modified during the course of the investigations and are shown in Table 3.5 along with the strains recorded near the sample surface. Values in parentheses omitted measurement positions at depths of 5 and 10 mm below the surface. Thermally induced strains were not expected to extend beyond 40 mm from the weld centre line.

To examine a particular region of the weld, slits were used in the path of the incident and diffracted beams in order to define a gauge volume G_V, Fig 3.7a. Adjustment of the slit width altered the sampling region. As the diffracted signal scales with size of the illuminated gauge volume it is typically desirable to make this as large as possible. Although, it must be sufficiently small to capture changes in stress/strain and to avoid an averaging effect. The sample was then translated relative to the beam to perform strain scanning at the locations

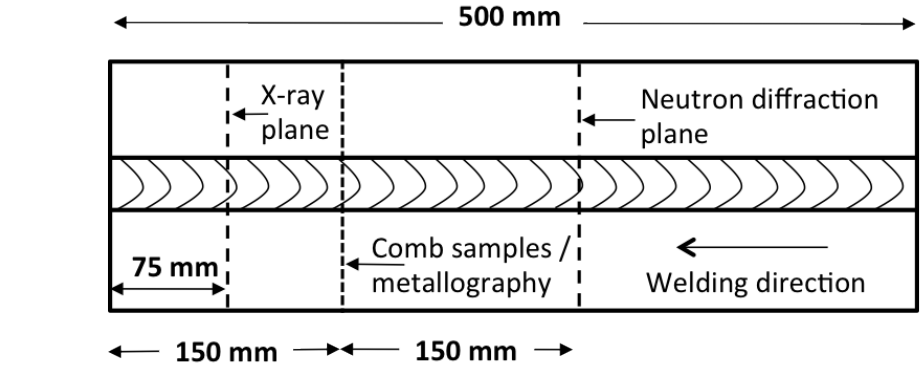

(a)

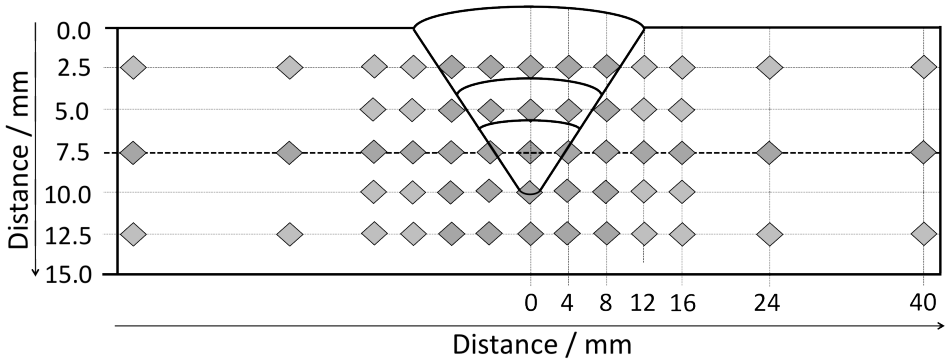

(b)

Figure 3.6: (a) Plan view of a welded plate showing the locations of the residual strain measurements and reference strain-free specimens, (b) cross section of a weld with the strain measurement positions identified by diamonds.

Table 3.5: Diffraction instruments and measurement locations.

Weld	Instument	Measurement positions / mm	
		Dist. from weld centreline	Dist. below top surface
A–C	ENGIN-X	± 0, 4, 8, 12, 16, (24, 40)	2.5, 5, 7.5, 10, 12.5
F, G	ENGIN-X	± 0, 3, 6, 9, 12, 16, (24)	
H, M, N	STRESS-SPEC	± 0, 3, 6, 9, 12, 16, (24)	2.5, 5, 7.5, 10, 12.5
K, L	STRESS-SPEC	± 0, 4, 8, 12, 16, (24, 40)	
C, G, H	L3	± 0–16 (increments of 1 mm)	0.15
C	L3	± 0, 4, 8, 12, 16	2.5
G, H	L3	± 0, 3, 6, 9, 12, 16	2.5

indicated. Also, an extended path length of the beam through the material leads to high attenuation of the signal and longer counting times. The most suitable sample orientations to counter this effect, which were adopted in this work, are in Fig. 3.7b. The arrows denote the strain direction/scattering vector. It should be noted that the uniformity of the stress field allows elongated gauge volumes to be selected for the transverse and normal strain measurements. However, the steep stress gradient with increasing distance from the weld centre line demands that a smaller gauge volume is used of the measurement of the longitudinal strains.

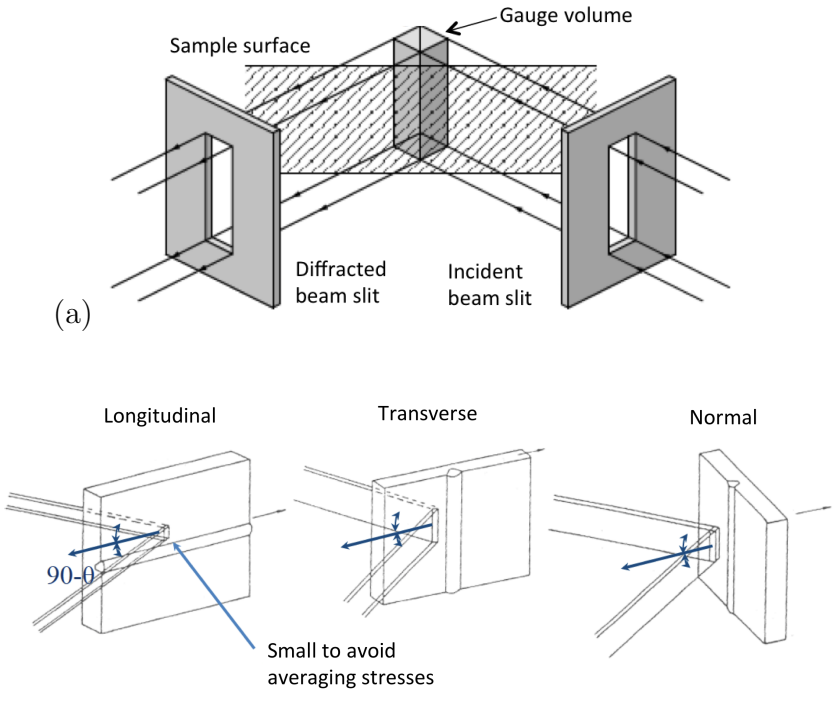

Figure 3.7: (a) Arrangement of beam slits to create the desired gauge volume [117], (b) plate orientations used to measure strain in three different directions [118].

3.3.2 Strain-Free Lattice Spacing d_0

The addition of large quantities of Cr and Ni to the welding filler results in an appreciable change of lattice spacing when compared with the low alloy steel base plate. This increase, caused by substitutional alloying, has the potential to mask thermally induced strains. For this reason, strain-free reference spec-

imens ('comb' samples) were used to account for the effect of compositional variation between the welding alloy and base material [119]. These were produced as 3 mm thick cross-sectional slices from the welded plate and further slotted at 3 mm intervals along the transverse direction using wire electro-discharge machining (EDM), Fig. 3.8. The EDM cuts create a free surface and thus relieve stresses in the region.

Measurements were taken from the strain-free specimens at the same depths as that for the welded plates, at the centre of each 'tooth'. However, as a result of the EDM cut positions, it was not possible to correlate the exact measurement locations for the comb with the welded plate in the transverse direction. Therefore, a function (described in chapter 4) was used to fit the strain-free lattice spacing measurements at each depth. A linear interpolation was then performed between the comb measurement positions to calculate the d_0 values for the relevant locations in the welded plates.

Figure 3.8: Typical *'comb'* sample (from weld C) used to determine the strain-free lattice spacing d_0.

3.3.3 ENGIN-X

Residual strains within the bulk of the material were measured at ISIS, which is a pulsed neutron source at the Rutherford Appleton Laboratory, UK. Prior to the diffraction experiment, the welded samples were co-ordinate measured using a CIMCORE portable measuring arm and digitised using the SScanSS software. This laser scanning technique allowed accurate positioning of the strain measurement points through creation of a virtual 3-D weld and programming of the X,Y,Z diffraction stage, Fig. 3.9. The attached spheres were

used as fiducial points and the plate was covered in grey primer paint to improve detection of the laser beam.

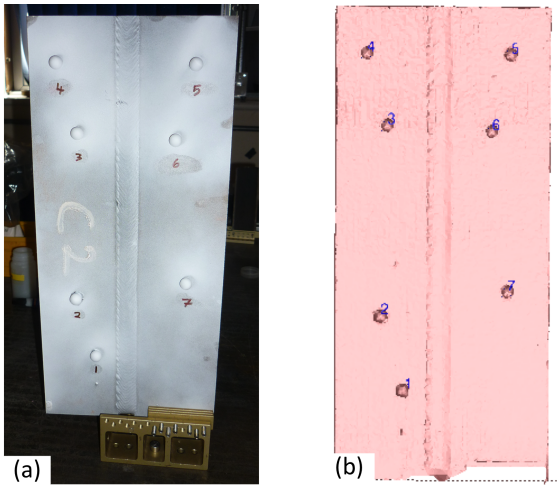

Figure 3.9: Co-ordinate measurements; (a) prepared weld, (b) virtual weld.

ENGIN-X is a time-of-flight (TOF) neutron strain scanner [120]. A pulsed beam of neutrons with a wide energy range, which corresponds to a range of wavelengths, travels to the sample. The essential components of the diffractometer are shown schematically, Fig 3.10a, where $L_1 + L_2$ is the path length. Neutrons originate from the moderator and travel down the primary beam path, L1, to the sample. The small fraction of them that satisfy Bragg's Law are scattered into the fixed detectors along the second flight paths, L2. The two detectors allows for the simultaneous acquisition of strain information in two independent directions, q_1 and q_2. The volume of sample measured at each position corresponds to the intersection of incident and diffracted beams, as defined by the slits and collimators. Since the wavelength, λ, of a neutron is related to its velocity, v, by the DeBroglie relation:

$$\lambda = \frac{h}{m_n v} \tag{3.6}$$

where h is Planck's constant and m_n is the neutron mass. Following a rearrangement of Bragg's Law and a knowledge of the neutron path length, the time-of-flight, t_n, can be converted into the interplanar spacing d:

$$d = \frac{h\, t_n}{2 \sin\theta\, m_n (L_1 + L_2)} \tag{3.7}$$

where θ is the Bragg angle (45 ° for the experimental configuration shown). Thus, if the detected neutron count is plotted as a function of time, it will exhibit a series of peaks corresponding to the different d_{hkl} lattice planes in the material [121]. The actual experimental set-up in Fig 3.10b, shows the incident beam line (red casing), which allows the stream of neutrons to pass through the slits and into the sample. The sample is oriented at 45° to the beam and detectors. A $3 \times 3 \times 3$ mm gauge volume was used for the longitudinal strain measurements, and a $3 \times 15 \times 3$ mm arrangement for the transverse and normal directions. A fixed 3 mm radial collimator was used to define one dimension of the gauge volume, with the other two defined by slits in the incident beam.

3.3.4 STRESS-SPEC

Residual strains within the bulk of the welded plates were also measured at Forschungs–Neutronenquelle Heinz Maier–Leibnitz (FRM II), Garching, Germany. This is a nuclear reactor type facility, which emits a steady stream of monochromated neutrons with a constant wavelength. The technique is akin to laboratory X-ray analysis, a plot of intensity versus theta produces a diffraction peak for a specific plane of atoms. It is then possible to calculate the strain simply from the measured diffraction angles:

$$\varepsilon = \frac{d - d_0}{d_0} = \frac{\sin\theta_0}{\sin\theta} - 1 \tag{3.8}$$

where $\sin\theta_0$ is the scattering angle from the reference stress-relieved comb sample and $\sin\theta$ from the welded plate.

Strain scanning was performed on the STRESS-SPEC instrument using a monochromatic beam with a wavelength of ~ 1.69 Å, provided from a bent Si (400) monochromator set to a take off angle $2\theta_{\mathrm{M}} = 77.3\,^{\circ}$. The diffracted intensities were recorded on a 30×30 cm position-sensitive detector. Measurements of the {211} ferrite diffraction peak were performed around a scattering angle of $2\theta_{\mathrm{S}} \approx 92.5\,^{\circ}$, which avoids errors associated with the asymmetry that

(a)

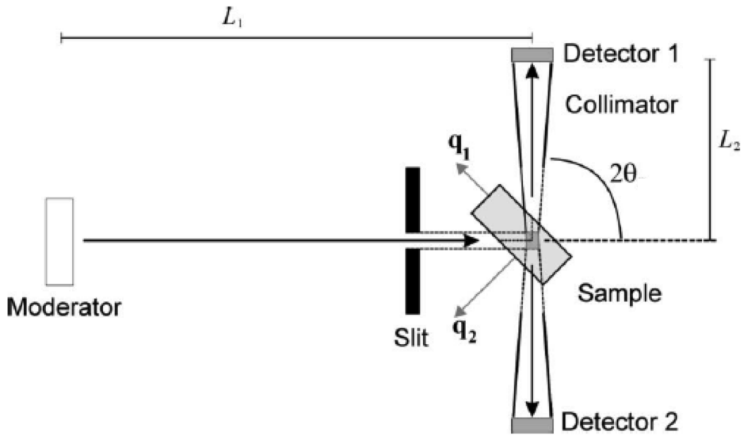

(b)

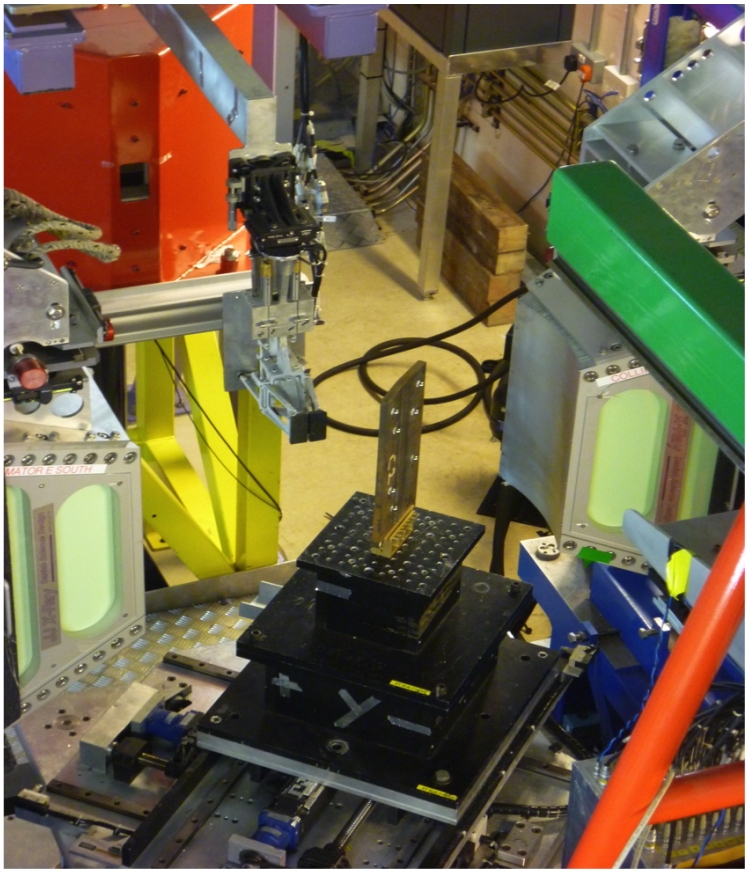

Figure 3.10: (a) Schematic illustration of ENGIN-X; positioning the sample at 45° to the incident beam allows strain to be measured along the sample axes in two directions simultaneously [120], (b) experimental set-up showing specimen C in the neutron beam oriented to measure the transverse and normal strain components. In view are the beam, slits, X,Y,Z stage and collimators leading to the two detectors.

would otherwise arise as a result of the finite height of the detector [122]. The {211} peak was selected as this reflection is known to accumulate only small compressive intergranular stresses following uniaxial tensile deformation [123, 124]. The stresses determined from the strains measured with this reflection and the appropriate diffraction elastic constants were therefore taken to be representative of the macroscopic residual stress.

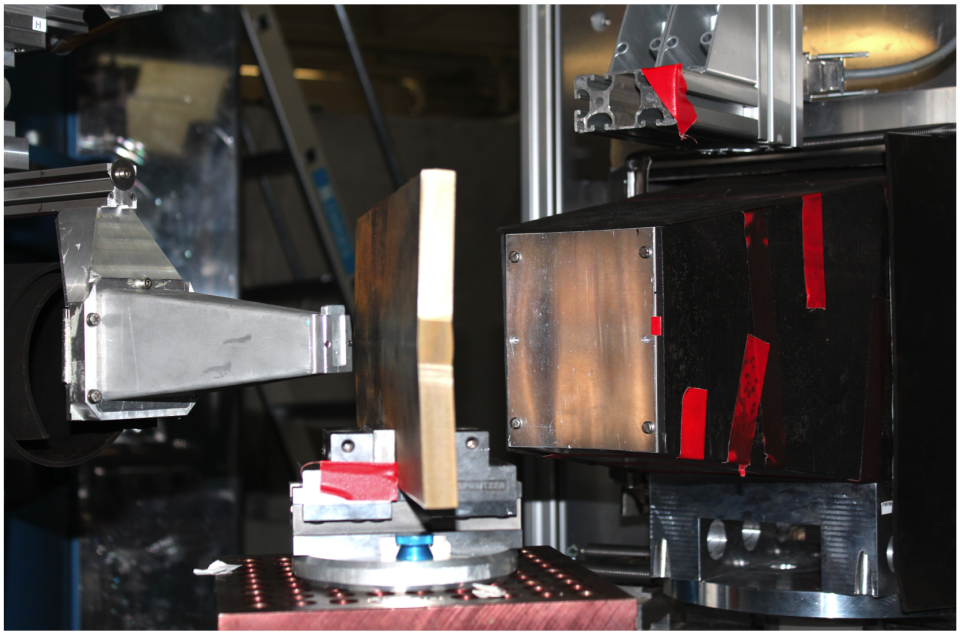

Figure 3.11: A welded plate installed on the STRESS-SPEC instrument aligned to measure the longitudinal strain component in transmission mode. From left to right is the incident beam slit, weld and collimator leading to the detector.

A gauge volume of $2 \times 2 \times 2$ mm was defined by a primary slit of 2×2 mm and a secondary 2 mm radial collimator for the longitudinal direction. The transverse and normal directions were measured using a gauge volume $2 \times 20 \times 2$ mm, with the long dimension of this volume parallel to the weld direction, Fig. 3.11. The use of an elongated gauge volume in the welding direction was deemed appropriate as the residual stress was not expected to vary significantly along the central portion of the welded plates. A theodolite was used to align the samples on the X,Y,Z translation stage with respect to the neutron beam. Wall scans were also performed to improve positional accuracy. These involve moving the sample in small increments so that the gauge volume becomes fully

immersed in the material. By observing the change in signal versus the sample coordinates the surfaces or *'walls'* of the plates could be determined to within < 50 micrometres. No signal is recorded when the gauge volume is entirely outside of the material.

3.3.5 L3 Stress-Scanning Diffractometer

Near-surface residual strains were measured on the L3 Stress-Scanning Diffractometer instrument at the Canadian Neutron Beam Centre, Chalk River, Canada [125]. This is also a reactor type facility and the general principals for the experimental conditions were as per FRM II. The major difference being the depth at which strains were evaluated. A monochromatic beam with a wavelength of $\sim 1.66\,\text{Å}$ was provided from a squeezed Ge (004) monochromator set to a take off angle $2\theta_{\text{M}} = 71.88\,^{\circ}$. The diffracted intensities were recorded on a position-sensitive detector. Measurements of the {211} ferrite diffraction peak were performed around a scattering angle of $2\theta_{\text{S}} \approx 90\,^{\circ}$.

A $0.3 \times 0.3 \times 3\,\text{mm}$ gauge volume was defined using 0.3 mm wide slits on the incident and scattered sides, with a height limiter on the incident side for the longitudinal direction. The transverse and normal directions were measured using a gauge volume of $0.3 \times 0.3 \times 20\,\text{mm}$, with the long dimension of this volume parallel to the weld direction. The experimental set-up is shown in Fig. 3.12 with the slits arranged to measure the near-surface d_0 values in the normal orientation. The gauge volume selected was deemed to be the smallest possible that was capable of producing defined diffraction peaks. The centroid of the gauge volume could therefore be positioned at 0.15 mm below the surface, whilst simultaneously avoiding partial-immersion errors.

Assessing the stress distribution at the fusion boundary/weld-toe of the welded plates was necessary as this is the predominant site of failure during fatigue experiments. In order to achieve positional accuracy, the change in full width at half maximum (FWHM) across the fusion boundary at the plate surface was analysed in 0.25 mm increments. The diffraction peak altered significantly when the gauge volume was totally immersed in the weld metal compared with the base plate and this effect was used to ascertain the fusion boundary

positions at the surface. Theodolites and 'wall' scans were implemented to determine the sample position with respect to the gauge volume.

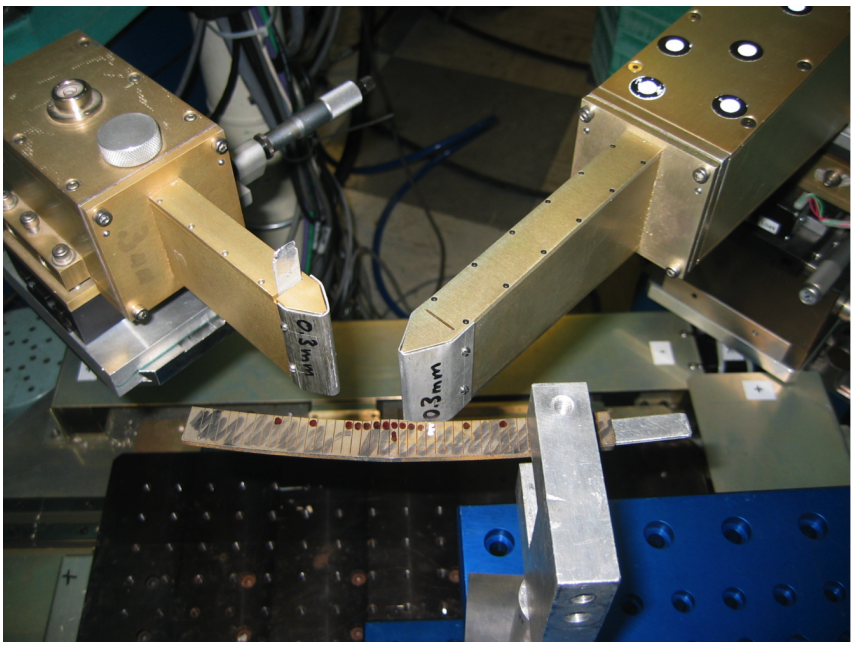

Figure 3.12: A d_0 specimen positioned in reflection mode to measure the normal strain component on the L3 Stress-Scanning Diffractometer instrument. On view are the incident (left) and scattered (right) beam slits.

3.4 X-Ray Diffraction – Surface Stresses

It is possible to measure the strains at the surface of a material using the $\sin^2\psi$ technique [118]. This is a common method for determining the stress condition in the longitudinal and transverse orientations of welded structures, where a zero stress state is assumed in the normal direction. The strains in the plane of the material are measured at a number of different angles to the surface. Considering the coordinate system in Fig. 3.13, where the principal axes are aligned with the plate geometry. The angle between the scattering vector and normal of the plate surface is denoted by ψ whilst ϕ is the measurement angle relative to the principal axes, ε_1 and ε_2, in the plane.

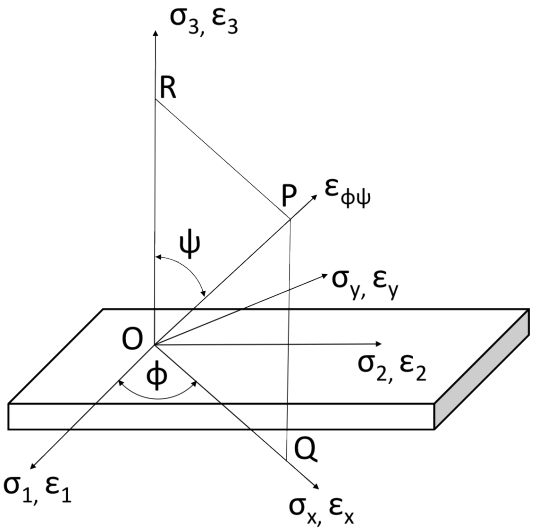

Figure 3.13: Definition of a sample coordinate system. The strain component is measured along $\varepsilon_{\phi\psi}$.

The strain $\varepsilon_{\phi\psi}$ is obtained from the principal strains:

$$\begin{aligned} \varepsilon_{\psi\phi} &= \varepsilon_1 \cos^2\phi \sin^2\psi + \varepsilon_2 \sin^2\phi \sin^2\psi + \varepsilon_3 \cos^2\psi & (3.9) \\ &= (\varepsilon_1 \cos^2\phi + \varepsilon_2 \sin^2\phi) \sin^2\psi + \varepsilon_3(1 - \sin^2\psi) & (3.10) \end{aligned}$$

The resolved component of $\varepsilon_{\phi\psi}$ in the plane of the plate (containing ε_1 and ε_2) is:

$$\varepsilon_x = \varepsilon_1 \cos^2\phi + \varepsilon_2 \sin^2\phi \tag{3.11}$$

Substitution into the previous equation:

$$\varepsilon_{\phi\psi} = \varepsilon_x \sin^2\psi + \varepsilon_3(1 - \sin^2\psi) \tag{3.12}$$

Assuming plane stress conditions:

$$\varepsilon_{\phi\psi} = \frac{(1+\nu)}{E}\sigma_x \sin^2\psi + \varepsilon_3 \quad , \quad \varepsilon_{\phi\psi} - \varepsilon_3 = \frac{(1+\nu)}{E}\sigma_x \sin^2\psi \tag{3.13}$$

The difference in strain for this equation is:

$$\varepsilon_{\phi\psi} - \varepsilon_3 = \frac{d_{\phi\psi} - d_0}{d_0} - \frac{d_3 - d_0}{d_0} = \frac{d_{\phi\psi} - d_3}{d_0} \tag{3.14}$$

An approximation that $d_0 \simeq d_3$ in the denominator introduces an acceptable error (about 0.1%):

$$\varepsilon_{\phi\psi} - \varepsilon_3 = \frac{d_{\phi\psi} - d_3}{d_3} = \frac{d_{\phi\psi} - d_{\phi 0}}{d_{\phi 0}} \tag{3.15}$$

Using this expression for the strain difference, in Equation 3.13:

$$\frac{d_{\phi\psi} - d_{\phi 0}}{d_{\phi 0}} = \frac{(1+\nu)}{E}\sigma_x \sin^2\psi \tag{3.16}$$

Rearranging:

$$d_{\phi\psi} = d_{\phi\psi}\frac{(1+\nu)}{E}\sigma_x \sin^2\psi + d_{\phi 0} \tag{3.17}$$

In order to obtain σ_x it is necessary to measure $d_{\phi\psi}$ at a number of different ψ–tilts, whilst keeping ϕ constant. Plotting $d_{\phi\psi}$ against $\sin^2\psi$; the gradient of the curve is $d_{\phi 0}(1+\nu)/E$ multiplied by the stress σ_x. The intercept gives the reference lattice spacing $d_{\phi 0}$.

The residual stresses measured using X-rays were performed on an Xstress 3000 instrument using Cr Kα radiation on the {211} for the ferrite phase. A 2 mm collimator was used and penetration depths were $< 10\,\mu$m from the sample surface, along the plane identified in Fig. 3.6a. The ψ angle was varied between -45° and $+45^\circ$ (8 angles in total). Measurements were performed on the as-received welded plates, with no prior grinding or polishing.

Chapter 4

Material Characterisation

4.1 LTT Alloys

The M_S of the undiluted LTT fillers were calculated from the dilatometry heating/cooling curves shown in Fig. 4.1. The gradient of the linear portion of the cooling curve was determined and a parallel straight line added to the plot, that is off-set by a fixed strain of 1 vol.% martensite formation. The point at which these lines cross is the M_S, this procedure ensures reproducibility of results between investigators, despite instrument noise [126]. There is a significant difference in the shape of the plots which can be attributed to the extent of phase transformations occurring. LTT-1 transforms to austenite during heating, $Ac_1 \sim 650$°C, and reverts back to martensite during cooling, $M_S = 163 \pm 12$ °C. The curve produced by the LTT-2 alloy does not display such obvious dilatations. The absence of an apparent transformation to austenite during heating would suggest that LTT-2 is austenitic at ambient temperature and therefore cannot transform during heating. The cooling cycle is in agreement with this theory and indicates that the transformation to martensite may not begin until room temperature or below is attained. The deviation from constant expansivity during the cooling cycle, evident for the LTT-2 alloy at approximately 850–750 °C, was caused by experimental error and occurred during the initial stages of quenching. It is also a feature of the LTT-1 curve and is not representative of a phase transformation.

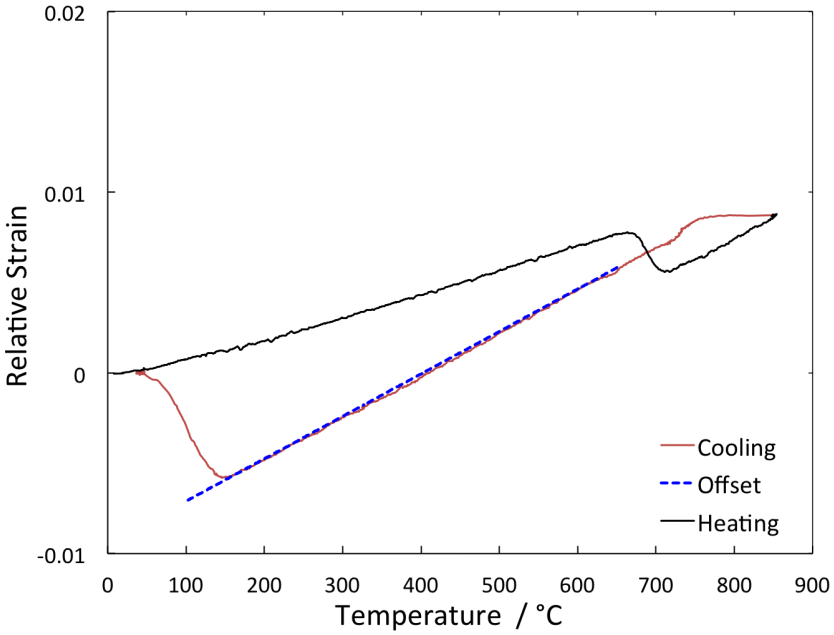

(a)

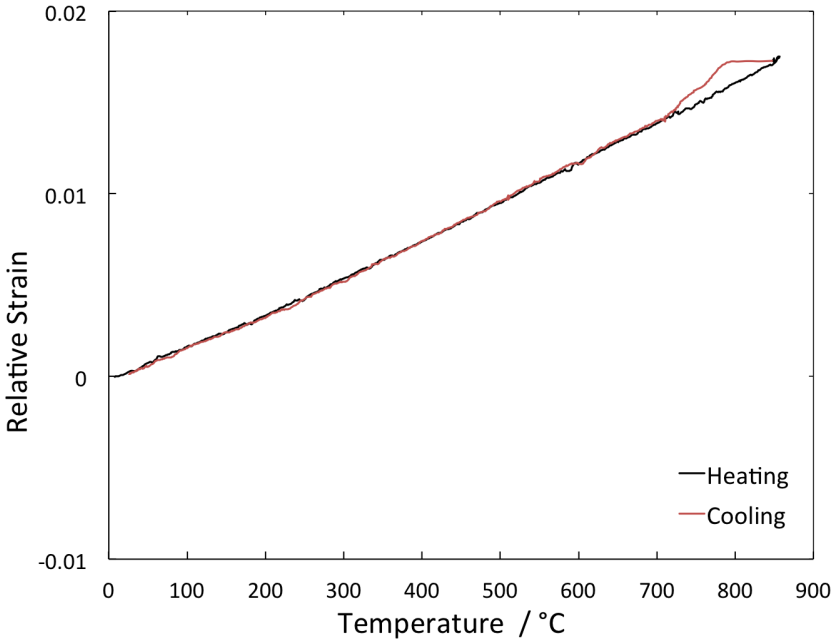

(b)

Figure 4.1: Dilatometric curves; (a) LTT-1 transforms to martensite at around 160 °C, (b) LTT-2 does not appear to undergo transformation within the temperature range of experimentation.

The micrographs in Fig. 4.2, taken after polishing and sub-zero cooling of the LTT-2 specimen, show evidence of surface displacements that are characteristic of the $\gamma \rightarrow \alpha'$ transformation. Decreasing the temperature shows significant relief changes up to $-20\,^{\circ}\mathrm{C}$. Although the M_{S} cannot be determined from the results, they indicate that transformation is still occurring below ambient temperature. The transformed LTT-2 specimen was further cooled to $-196\,^{\circ}\mathrm{C}$ and re-tested in the dilatometer, Fig. 4.3. The $\alpha' \rightarrow \gamma$ transformation is evident during heating at approximately $650\,^{\circ}\mathrm{C}$ but there is no indication of $\gamma \rightarrow \alpha'$ transformation during cooling. This is in agreement with the initial dilatometric results and morphological observations.

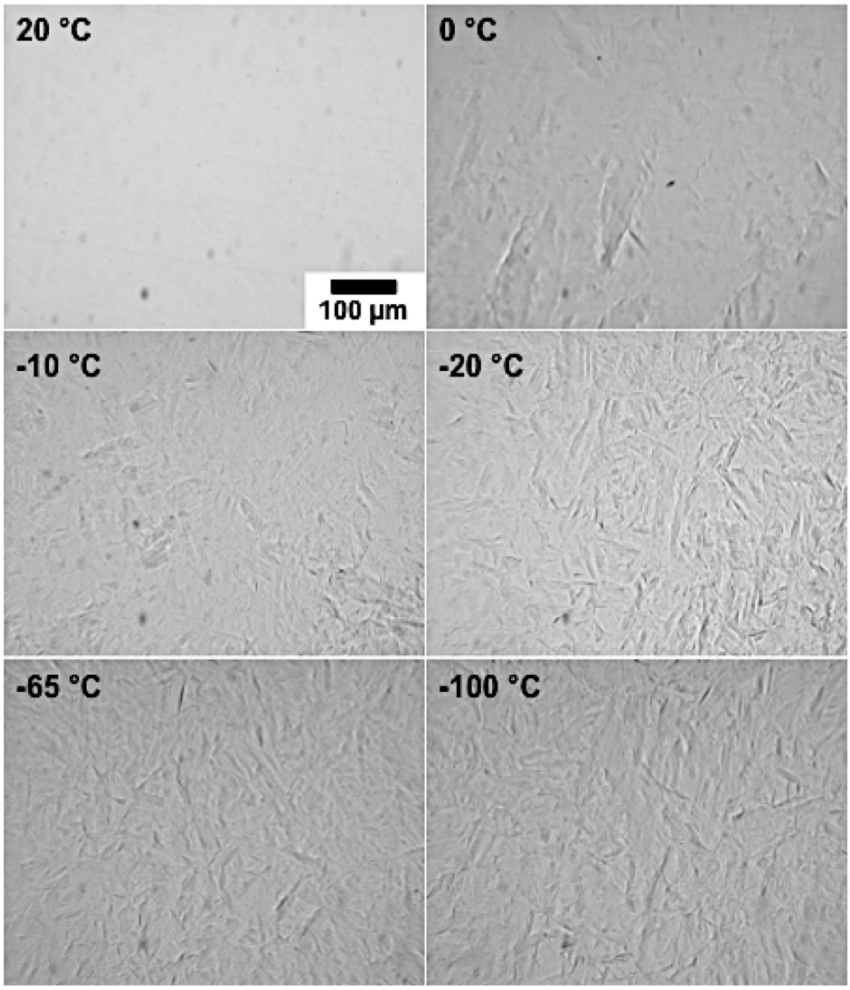

Figure 4.2: Cooling a polished LTT-2 specimen revealed surface morphology changes at different temperatures caused by the unconstrained $\gamma \rightarrow \alpha'$ transformation.

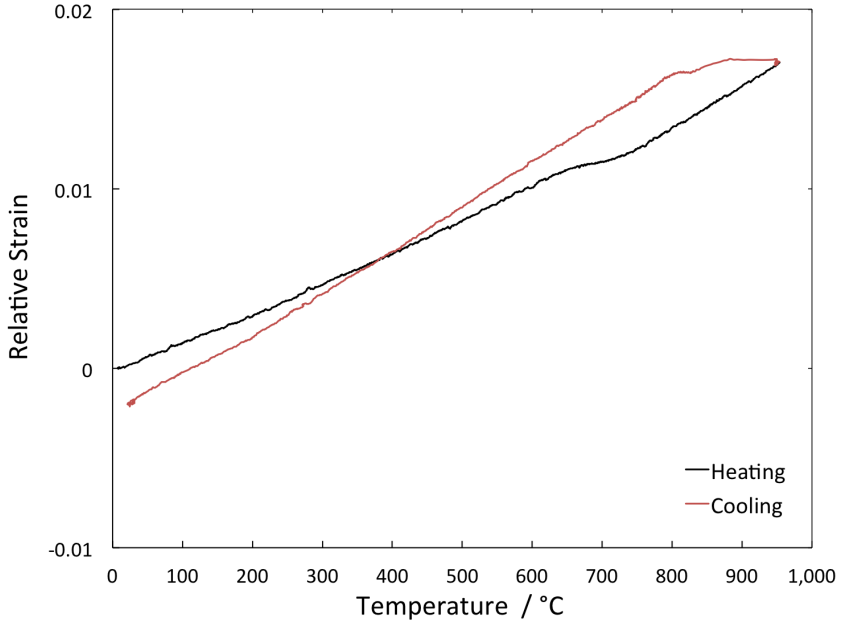

Figure 4.3: Dilatometric curve of LTT-2 that was cooled to −196 °C prior to testing.

The M_S and hardness values for the LTT alloys are in Table 4.1. The M_S of LTT-1 is consistent between specimens and is most comparable to the prediction by Kung *et al.*, Table 3.3. The undiluted LTT-2 M_S was undetermined using dilatometry because of its suppression to around ambient temperature or below, the neural network supplied by Sourmail *et al.* being the most accurate estimate here. This could present the problem of insufficient $\gamma \rightarrow \alpha'$ transformation for stress relief. However, the M_S measured using dilatometry will be lower than that for a weld due to the effects of dilution and constraint. Indeed, the LTT-2 filler was developed with the specific purpose of accounting for dilution and is expected to have a composition, and hence M_S, similar to LTT-1 following dilution with the base plate. In addition, the material will be constrained during welding and transform at a higher temperature because the mechanical work done by the applied stress contributes to the free energy change calculation [127]. This phenomenon will also have the effect of raising the M_S of LTT-1. Thermo-mechanical simulation combined with synchrotron X-ray diffraction would provide a more accurate M_S representative of welding conditions. Although, dilatometry and models should be sufficient to develop fillers capable of compensating for thermal contraction strains because a wide range of M_S are capable of inducing compression into specimens, Fig. 2.18.

Table 4.1: M_S and hardness values of the undiluted welding alloys.

Specimen	Alloy	Condition	M_S / °C	Hardness / HV30
1A	LTT-1	As-received	160 ±12	322 ±17
1AR	LTT-1	Repeat of 1A	163 ±12	-
1B	LTT-1	As-received	170 ±12	349 ±6
2A	LTT-2	As-received	Undetermined	157 ±6
2AR	LTT-2	2A cooled to −196 °C	Undetermined	254 ±11
2B	LTT-2	As-received	Undetermined	178 ±13

Hardness results indicate higher quantities of retained austenite for the LTT-2 alloy compared with LTT-1. Specimen 2A had an initial hardness of 157 ± 6 HV30, which changed to 254 ± 11 HV30 (2AR) after cooling to −196 °C. This would suggest an increase in martensite content with undercooling below its M_S. The microstructures, Fig. 4.4, reveal (a) martensite for LTT-1 and (b) untransformed dendritic austenite for LTT-2 (specimen 2A).

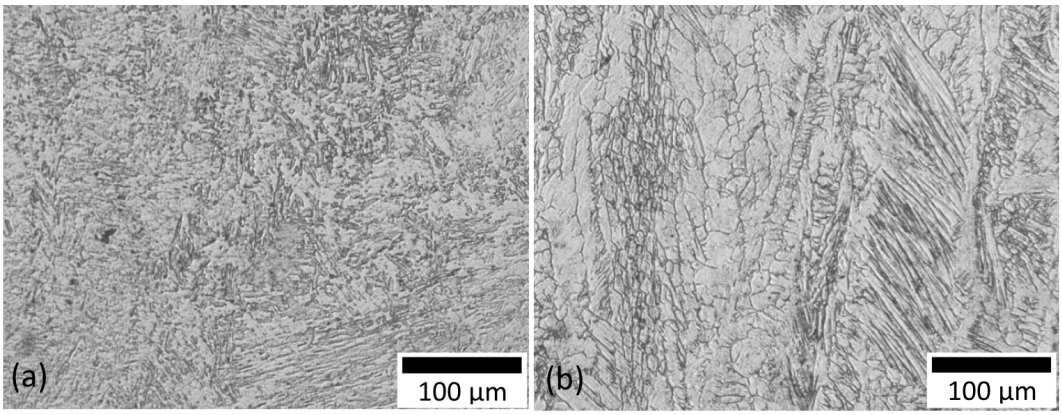

Figure 4.4: Microstructures of undiluted alloys; (a) LTT-1, (b) LTT-2.

4.2 Welded Plates

Macrostructures of welds A, B and C highlight the fusion boundary, heat-affected zone and the effects of multiple welding passes, Fig. 4.5. The cross-

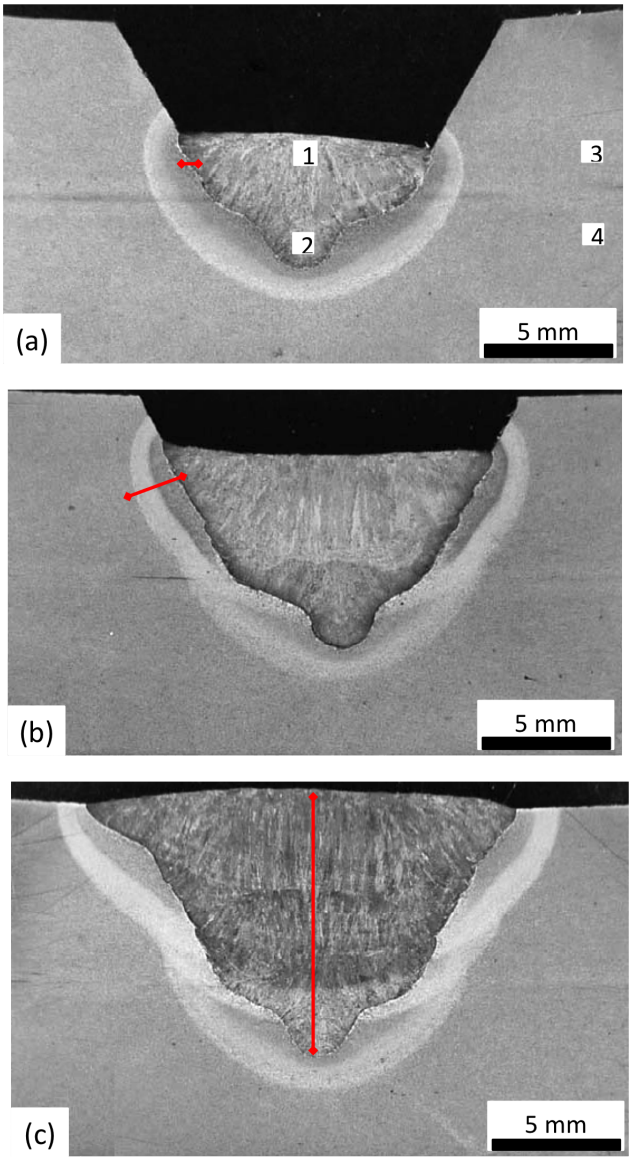

Figure 4.5: Weld macrostructures; (a) weld A is a 1–pass weld showing the EDX composition measurement positions including the line profile across the fusion boundary (b) weld B is a 2–pass weld, the line corresponds to the microstructural investigation across the HAZ, (c) weld C is a 3–pass weld locating the hardness profile along the weld centreline.

section of the original V-shape, machined along the length of the plates, has changed geometry where the base plate has been melted by the molten filler. The microstructural changes that occur across the neighbouring HAZ as a result of heat dissipation from the weld deposit are shown for weld B, Fig. 4.6. The characteristic zones associated with welding are a result of the temperature gradient from the weld to the unaffected base material. Especially evident is the effect on grain size, which reduces moving away from the fusion boundary.

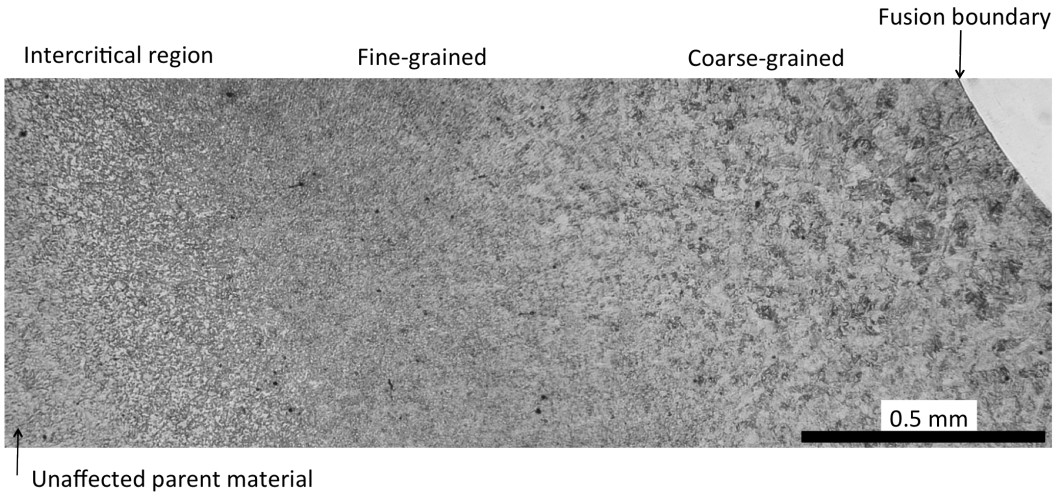

Figure 4.6: Weld microstructure across the heat-affected zone.

Metallography verified the presence of martensite in the weld metal, Fig 4.7, the image was taken from the final pass of weld C. The hardness values in Table 4.2 show consistency between the three welds and are representative of a martensitic structure. The rapid decrease for welds A and B is due to measurements in the base plate, whereas the weld deposit for weld C extended for 10 mm.

It is necessary to understand the extent of filler dilution with the base plate for microstructural control and M_S prediction. It is also a prerequisite for accurate strain evaluation to ensure that changes in the lattice spacing are caused by thermal contraction/transformation and not variations in composition. The heavily alloyed LTT fillers will naturally assume internal lattice strains due to the imperfect inclusion of substitutional and interstitial elements. This is the

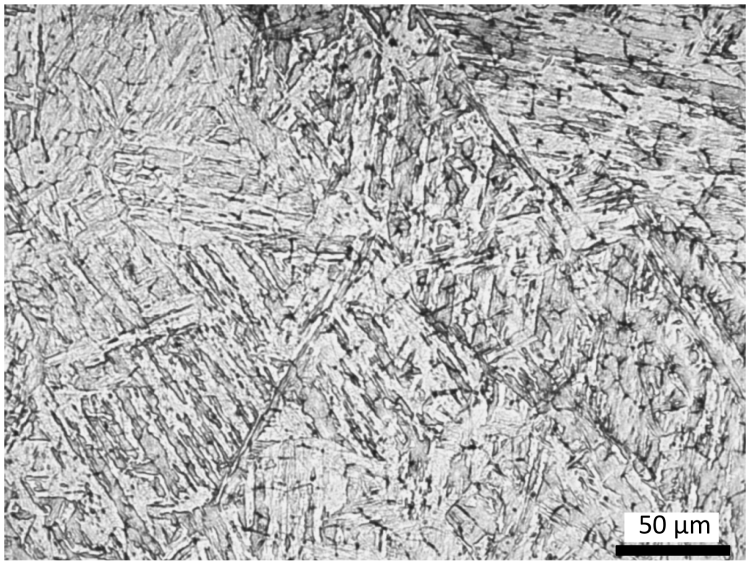

Figure 4.7: Martensite in the LTT-1 weld deposit.

Table 4.2: Hardness profiles / HV10.

Position below surface/ mm	Weld A	Weld B	Weld C
1	393	374	372
2	394	375	375
3	387	374	376
4	383	364	379
5	377	397	376
6	294	387	384
7	246	299	375
8	266	265	393
9	274	230	366
10	280	255	382

principal behind the use of strain-free specimens cut from the weld and their purpose is to exclude errors that could potentially arise through compositional mis-match between d and d_0.

The locations of the EDM cuts to create the strain-free specimens do not allow perfect correlation with the strain measurement positions in the welded plates. This necessitates an interpolation between the measured d_0 values, and one of the assumptions associated with applying this method is a constant composition in each layer of weld material. Although the bulk weld metal is essentially homogeneous, some studies have shown that macrosegregation can exist near the fusion boundary of welds made with dissimilar filler metals [128].

The extent of dilution for the single-pass weld, A, is the order of $\sim$ 20–25% when compared with the original Cr–Ni values for the LTT-1 alloy, Table 4.3. A line profile across the fusion boundary, Fig. 4.8, shows that the compositional change between the base plate and weld material occurs over a distance of $\sim 20\,\mu$m. Once the transition is complete, the weld material records elemental values that fluctuate about a nominal composition (10Cr–4.5Ni).

Table 4.3: Compositions (wt %) of the weld deposit and base material for weld A. The original undiluted filler value is included for reference.

Position	Material	Si	Mn	Cr	Ni
1	Weld	0.6	1.6	10.2	4.5
2	Weld	0.7	1.8	10.1	4.8
3	Base plate	0.3	1.2	0.2	0.0
4	Base plate	0.3	1.2	0.2	0.0
Table 3.1	LTT-1	0.8	1.6	12.7	6.0

Further studies were conducted using EPMA in order to assess the concentrations of the major alloying elements across the entire weld deposit at measurement depths equivalent to the neutron diffraction positions, Fig. 4.9. Data collected at 7.5 mm was not usable due to instrumental errors. Measurements at depths of 10, 5 and 2.5 mm correspond to the three different welding passes, 1, 2 and 3 respectively. The 12.5 mm reading was taken from the base plate

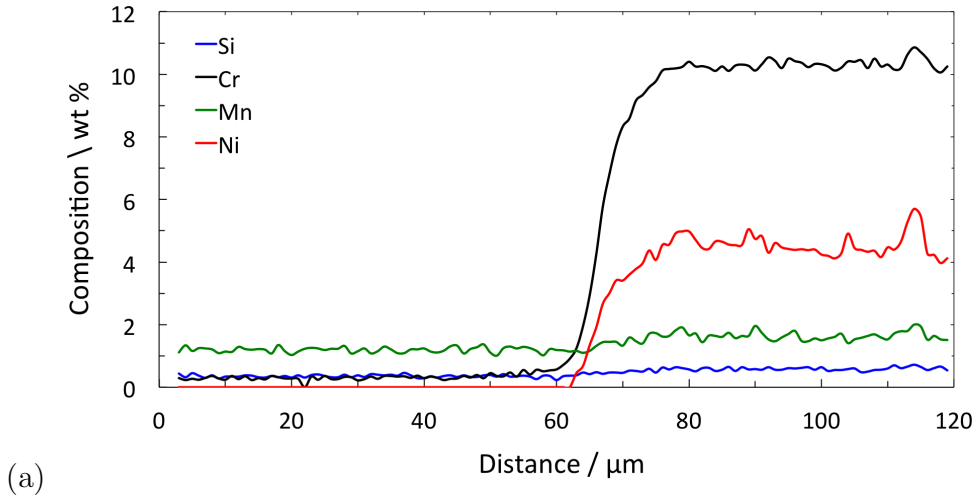

(a)

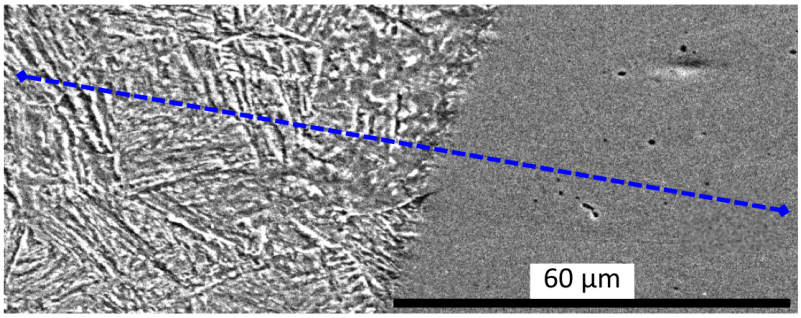

(b)

Figure 4.8: Base plate (etched) → weld deposit; (a) composition profile across the fusion boundary, (b) EDX measurement positions.

only. The general shape of the plots, where the weld metal is included, show a rapid transition of element concentration from the low alloy base material to the filler. The composition then remains at a constant mean level across the weld deposit, although the Cr–Ni values fluctuate within a range of ~ 2.5 wt%. This is caused by microsegregation during solidification and influences the lattice spacings at these positions.

The mean compositions of the weld metal are presented in Table 4.4, along with their calculated lattice parameter [129]. Also included are the maximum/minimum elemental concentrations of Cr–Ni at a depth of 2.5 mm (Si and Mn were kept at their average levels). The difference in lattice parameter between these two values would be equivalent to 10^3 microstrain and highlights the potential for composition variation to influence the perceived '*residual stress*'. Considering the alloying additions and calculated lattice parameter of the base plate versus the LTT filler, the microstrain would be more than double this magnitude. The necessity for accurate d_0 values that correspond to the measurement locations in the welded plate is essential for stress determination because this is the single greatest opportunity for error.

Table 4.4: Average composition (wt %) and associated lattice parameter of the weld deposit at different depths below the surface; weld C. Included are the maximum and minimum values for Cr–Ni at 2.5 mm.

Depth / mm	Si	Mn	Cr	Ni	Lattice Parameter / Å
2.5	0.60	1.69	12.20	5.24	2.87781
5.0	0.60	1.70	11.96	5.08	2.87758
10.0	0.54	1.55	10.10	4.40	2.87611
2.5_{min}	0.60	1.69	11.00	3.84	2.87626
2.5_{max}	0.60	1.69	13.40	6.64	2.87936

Comparing the composition of the 1$^{\text{st}}$–pass measured at a depth of 10 mm for weld C (EPMA) versus the single-pass, weld A (EDX), there is excellent agreement between the results. The underlying layers of weld metal that are not re-melted remain at a constant composition. The extent of dilution is also apparent and the difference between pass 1–3 is approximately 20 wt%.

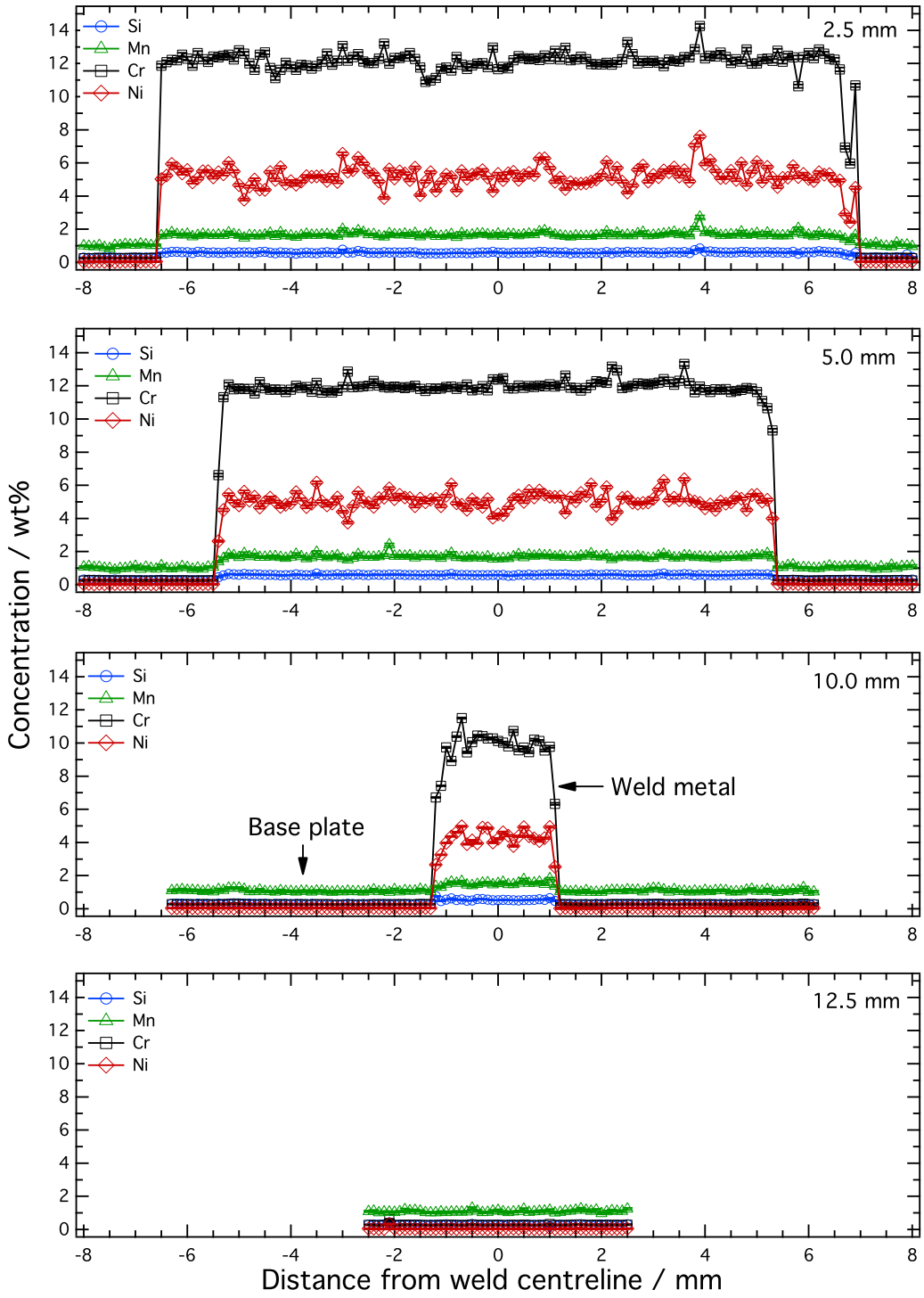

Figure 4.9: Composition profiles measured by EPMA across the weld deposit at different depths below the top surface.

4.3 Gauge Volume

Although the there is a fluctuation of elemental concentration within the weld metal, this is not expected to contribute to error with respect to strains recorded in both the d_0 and welded plates. This is due to the lattice spacings being measured from a volume at each location, which is sufficient in size to diminish the effects of microsegregation. Indeed, the gauge volume plays an influential role in stress determination, if it is too large then important stress gradients and peaks will be averaged. The diamonds in Fig. 4.10 represent the sampling volume and provide an indication of the quantity and locations of material assessed for a 3–pass welded plate on ENGIN-X; $G_V = 3 \times 3 \times 3\,\text{mm}$. When evaluating stresses using neutron diffraction, it is imperative to consider the gauge volume for their correct interpretation. A potential source of error can result from this volume being partially immersed in the specimen and may occur for the d_0 references because of their relative size ($3 \times 3\,\text{mm}$ width). This issue was negated by positioning the centroid of the gauge volume in the centre of each tooth such that any extension beyond the material was equally distributed either side. This eliminated false readings at the fusion boundary.

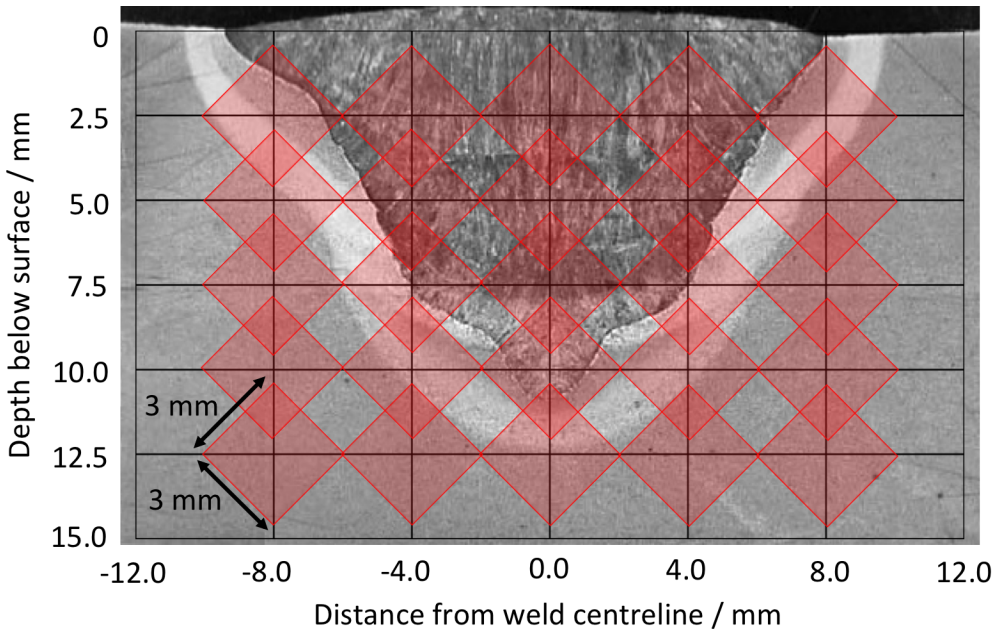

Figure 4.10: Projection of the gauge volume (red diamonds) onto a section of weld C as measured in the normal orientation at the ISIS facility. The diamonds would also extend 3 mm out of the plane of the page.

4.4 Strain-Free Reference Specimens

Each of the welded plates that were subjected to neutron diffraction had a corresponding strain-free '*comb*' sample that was used to produce the d_0 values. The lattice parameters recorded in the longitudinal and normal directions for comb C are presented in Fig 4.11, measurements were taken at depths below the surface following the same convention as the welded plates. Immediately apparent is the abrupt increase in atomic spacing for the weld metal. This is most appreciable at depths of 2.5–7.5 mm where the sampling volume is fully immersed in the weld metal. Partial immersion will render a lattice spacing somewhere between the maximum and minimum, depending on the percentage illuminated, as at 10 mm. A minor reduction in the maximum lattice parameter is observed at 7.5 mm, compared with 2.5 mm, this is due to the effects of filler dilution with the base material. When measuring d_0 values, the lattice spacings are expected to be equal in the orthogonal directions at each position. There would appear to be an error associated with the two sets of detectors which has caused a systematic shift in lattice parameter between the normal and longitudinal orientations. However, this error is cancelled if the same detector is used for both the d_0 and d measurements.

The points were fitted at each depth using a function to accommodate for the effects of partial immersion in the weld deposit:

$$\text{output} = \frac{\text{Area}}{2A}\text{erf}\left(\frac{2(x - x_0) + A}{2\sqrt{2}S}\right) + \text{erf}\left(\frac{2(x_0 - x) + A}{2\sqrt{2}S}\right) + C \qquad (4.1)$$

where the *output* is the lattice parameter/spacing as a function of distance from the weld centreline. A is the width of the weld deposit at a given depth, S is a constant based on the gauge volume width, x is the distance from the weld centreline, x_0, and C is lattice parameter/spacing of the base plate. The gauge volume was located in the centre of each tooth with respect to the transverse orientation (for all measurement directions) but the function allows alignment between the d and d_0 measurement positions. This principle was also applied for data collected at FRM II and Chalk River.

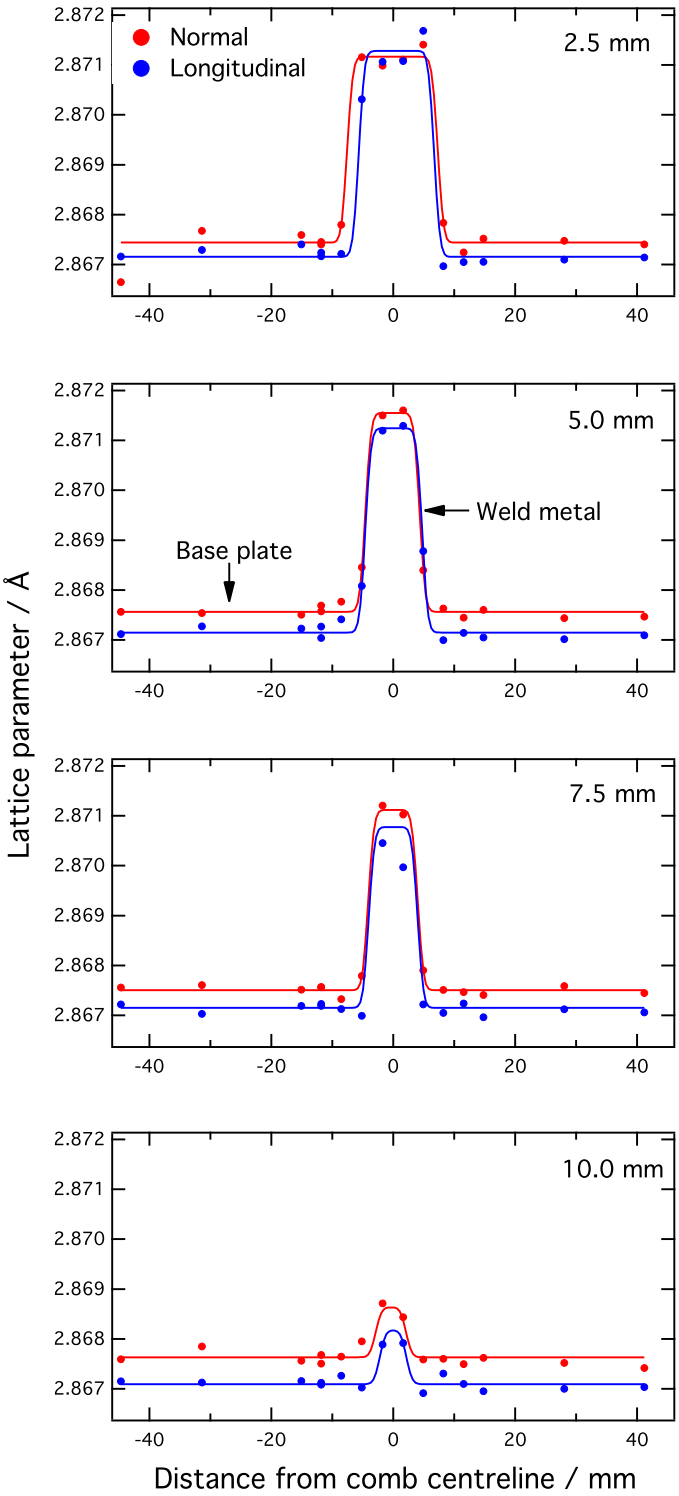

Figure 4.11: Lattice parameters measured at different depths below the surface of comb C.

4.5 Neutron Diffraction – Data Analysis

ENGIN-X is a time-of-flight instrument that generates a range of wavelengths and allows a number of diffraction peaks to be recorded simultaneously, Fig. 4.12. The individual peaks can be analysed separately, as for continuous flux sources, but in this work, information from the entire spectra was used to derive the average unit cell parameter. This Rietveld refinement technique, involves a least-squares fitting procedure to the whole diffraction pattern [130]. It was first applied to untextured powder specimens and has subsequently been modified by Pawley for textured materials such as welds [131]. Strain analysis is primarily concerned with peak position rather than intensity and the Pawley refinement is able to accommodate the intensity variations associated with texture. By fitting an average lattice spacing to all of the diffraction peaks, the value is close to the macroscopic strain and therefore bulk elastic constants can be used to calculate the stresses. The Kröner model, which assumes an ellipsoidal single crystal in an isotropic matrix of bulk material, was adopted for the ferritic steel specimens where $E = 212.7$ GPa and $\nu = 0.30$ [29].

The instruments at FRM II and Chalk River were restricted to one wavelength and as such only a single peak was recorded for a specific reflection, Fig. 4.13. Once the background was removed, the intensities were fitted with a gaussian profile in order to determine 2θ. The two profiles were taken from the weld metal at 2.5 mm depth along the weld centreline and highlight the effects on 2θ of a compressive stress in the welded plate (K) compared with the strain-free specimen. Data were recorded from the $\{211\}$ because this reflection is known to accumulate only small compressive intergranular stresses following uniaxial tensile deformation [123, 124]. Bulk elastic constants would not be suited for a singular family of planes so diffraction elastic constants are used for stress calculation, where $E = 220$ GPa and $\nu = 0.28$ [132].

The practice of strain measurement through diffraction techniques is reliant on the identification of peak shifts. Varying composition will effect this significantly but errors are also introduced through peak broadening, asymmetry, large grain size and texture. These all lead to less accurate peak locations through difficulties in fitting an appropriate profile. Generally, peak shapes

from steady-state reactors are gaussian in nature and not prone to asymmetry, however, those from pulsed sources can be, due to the moderation process. Peak intensity can be effected by texture or a large grain size, these conditions mean that fewer crystallites are able to satisfy Bragg's Law, reducing the number of reflections. Broadening is caused by less than perfect instrumentation and specimens, some of the microstructual influences are:

- Inhomogeneous microstrain as described in Fig. 2.5.
- Concentration gradients caused by microsegregation.
- Large stress gradients within the gauge volume such as at the fusion boundary.

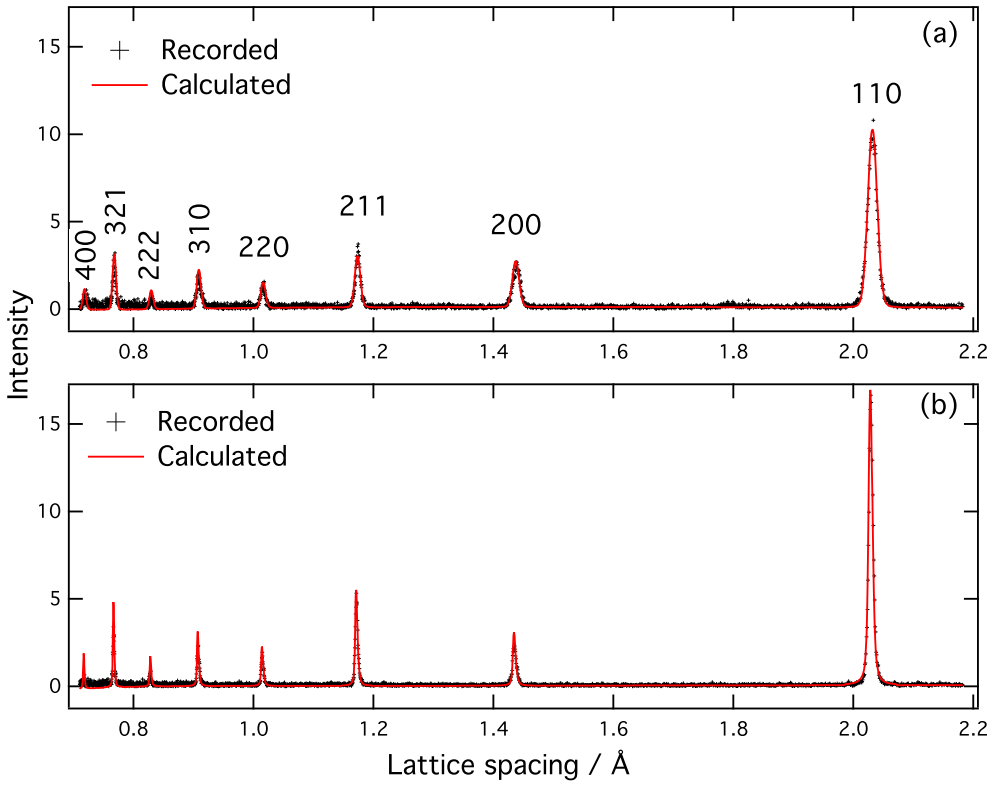

Figure 4.12: Indexed diffraction spectra generated using the ENGIN-X instrument; weld C (a) the weld deposit, (b) base plate.

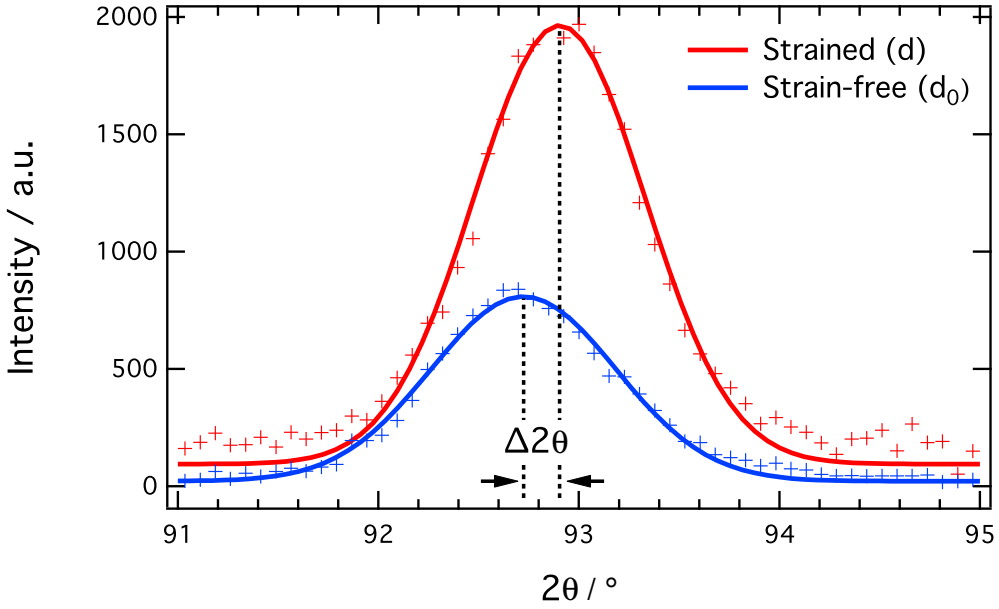

Figure 4.13: Diffraction angles for an as-welded and strain-free specimen. The peak shift to the right (increase of 2θ) corresponds to an induced compressive residual stress.

4.6 Conclusions

The LTT fillers have been characterised in terms of their microstructure and martensite-start temperature. Element concentrations were measured across the weld section. Experimental conditions have been defined along with a robust analysis procedure.

LTT-1 has a $M_S \simeq 165\,^{\circ}\mathrm{C}$ and the predicted value by Kung *et al.*, $169\,^{\circ}\mathrm{C}$, was the most accurate. The M_S of LTT-2 was undetermined as a result of its suppression to ambient temperature or below, the estimate by Sourmail *et al.*, $31 \pm 33\,^{\circ}\mathrm{C}$, was the most satisfactory in this instance. Dilatometry, microscopy and hardness studies all indicate the presence of retained austenite in the undiluted LTT-2 weld metal. Analysis of the welded plates A,B,C revealed martensite in the deposited weld metal.

Compositional variation between welding passes is caused through dilution of the filler with the base material, and under the specific welding conditions stated the difference was approximately 20–25% (pass 1–3). The filler alloying additions fluctuated about a mean level across the weld metal, due to microsegregation during solidification. Both of these phenomena significantly effect the lattice spacings and have the potential to mask measured thermal contraction strains. The compositional transition at the fusion boundary was abrupt and occurred over a distance of $\sim 20\,\mu\mathrm{m}$.

The influence of gauge volume size on stress determination was considered and has the potential to average steep gradients. Although, a relatively large sampling volume has the capacity to reduce errors caused by microsegregation.

Analysis conditions for the three instruments used for neutron diffraction have been presented along with their representative spectra. Peak position relative to an unstrained reference were used to infer stresses, however, broadening and asymmetry contribute to errors during curve fitting.

An accompanying strain-free reference specimen was measured alongside each welded plate in an effort to minimise internal strains caused by extensive substitutional alloying. It was necessary to use an interpolation function to match the strain measurement positions in the weld with the combs. This was due to the cuts made in the comb for stress relaxation and the weld centreline was used as the reference position. The function applied accounted for the change in lattice spacing associated with transition of the gauge volume into the weld metal from the base material. It included the width of the weld deposit, the size of the gauge volume and was capable of determining the lattice spacing at any distance from the centreline during partial immersion of the weld metal.

Chapter 5

Multipass Welds

5.1 Introduction

Diffraction data and fatigue tests have demonstrated that the use of LTT weld filler alloys can be beneficial in mitigating residual stresses and their consequences, chapter 2. However, the majority of engineering fabrications require the deposition of multiple layers in order to fill the weld joint and the literature to date has concentrated on single-pass welds. For multipass welds, much of the LTT material deposited in underlying passes will not be reheated into the austenitic phase by the heat of a subsequent layer [10]. Therefore thermally-induced strains will accumulate, which will be retained to room temperature.

A possible way of avoiding this issue is through the use of an interpass temperature T_{I} in excess of the M_{S}. This enables the whole of the multilayer, filled weld joint to remain austenitic. On subsequent cooling at the end of the welding operation the entire deposit can then transform into martensite in order to cancel the development of contraction stresses. The process is illustrated in Fig. 5.1. In this chapter, data are presented from the sequential changes of residual stress distribution for a 1–, 2– and 3–pass weld, Fig. 3.3, generated using neutron diffraction. Further measurements were performed on two multipass welds fabricated with an LTT filler to assess the effect of interpass temperature relative to the M_{S}. An initial, high M_{s} welding alloy was also investigated for comparison with the LTT alloy.

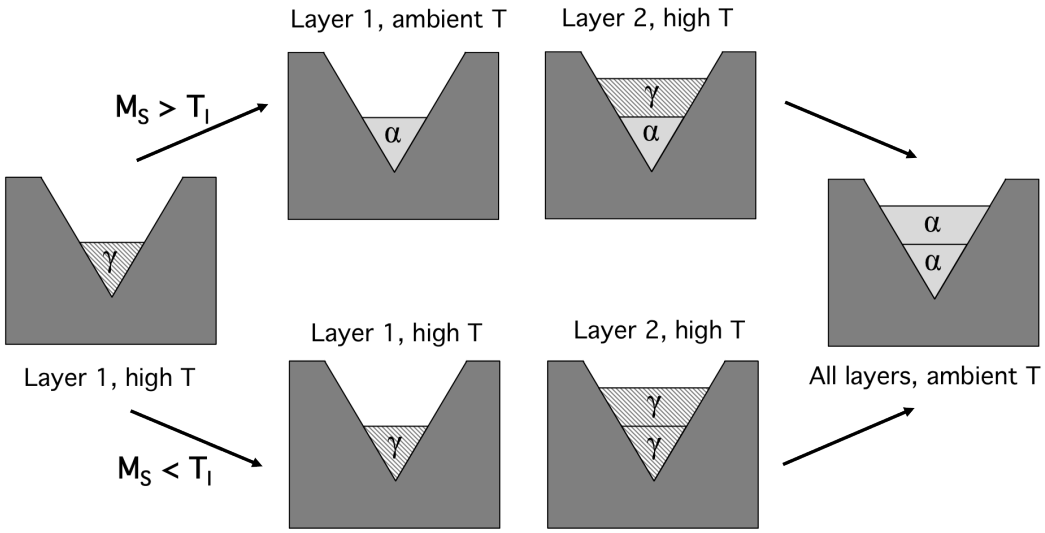

Figure 5.1: The influence of the difference between the interpass temperature T_I and the M_S temperature on the development of structure in the weld. When $M_S > T_I$, the multilayer weld does not transform homogeneously, whereas for $M_S > T_I$, all the layers remain austenitic until the weld is completed. Note that partial austenitisation that is likely for $M_S > T_I$ is not illustrated for the sake of clarity [133]

The residual stress measurements are presented as stress contours overlaid on their respective macrographs for the longitudinal, transverse and normal directions for each of the welded plates, e.g., Fig. 5.2. The crosses represent the original strain measurement positions and the stress contours have been restricted to the minimum (2.5 mm) and maximum (12.5 mm) measurement positions below the top surface. Extrapolation to the surface would not be appropriate due to potentially steep stress gradients that would need to be taken into account. It is noted that the measured strains are averaged over the gauge volume, which represents the spatial resolution of the technique used. This will have the effect of smoothing variations, particularly where the gradients are steep.

5.2 Conventional Welding Alloy

The longitudinal, transverse and normal stress contours for a plate welded with a standard, high M_s welding alloy (weld H) are presented in Fig. 5.2. The calculated M_s of the undiluted filler (HTT-1) is 372 °C. Considering the V–shaped weld, the contours follow the fusion boundary and display remark-

able symmetry reflected across the weld centreline. This is not surprising, given the geometry of the weld and has been seen in similar experiments [76]. There is a clear difference in the magnitude of stresses developed for the three different measurement orientations. The longitudinal direction displays the highest tensile stress ($> 600\,\text{MPa}$), predominantly occupying the HAZ region. The residual stresses for the transverse and normal orientations are significantly lower, with peak tensile stresses $\sim 200\,\text{MPa}$, also occurring in the vicinity of the HAZ. It is, perhaps, to be expected that the longitudinal stresses are greatest because this is the direction of maximum thermal constraint during cooling. The body of cooling weld metal (plus melted surrounding baseplate) is seeking to contract in all directions but the longitudinal orientation restrains contraction along the greatest length. This relationship between the longitudinal, transverse and normal stresses is evident for all of the welds assessed in this work.

A very small magnitude ($-100\,\text{MPa}$) of stress at singular points are measured in the weld metal in the transverse and normal directions. No compressive stress is observed in the longitudinal direction, although the stress is much lower in the fusion zone ($\sim 200\,\text{MPa}$) compared with the HAZ. The weld metal itself will benefit from transformation plasticity as it transforms from $\gamma \rightarrow \alpha'$ but this occurs at a relatively high temperature, thus allowing further thermal contraction strains to develop following its completion.

The stress magnitude for all three orientations is highest in the HAZ but then decreases, moving away from this region and into the unaffected baseplate. The trend is more apparent in Fig. 5.3, which is for the longitudinal direction only, but highlights the peak tensile stresses and their sharp decline. This reduction continues, moving away from the weld centreline, until there is a reversal in sign and compressive residual stresses are generated in the base plate to equilibrate the tensile stresses. The profiles join specific measurement locations at different depths below the top surface and additionally emphasise symmetry across the weld centreline.

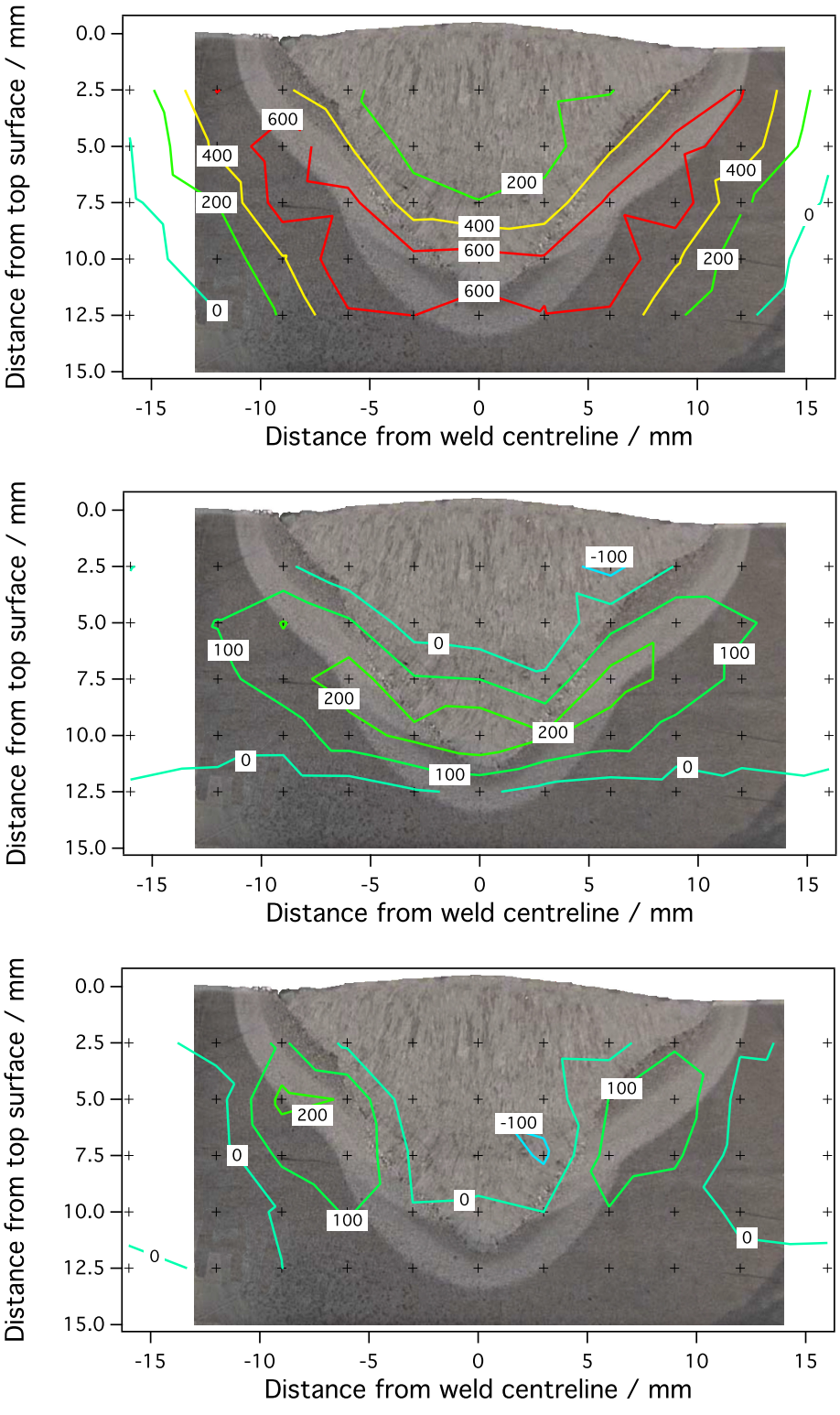

Figure 5.2: Residual stress contours for a standard, high M_s welding alloy (weld H), in MPa; (a) longitudinal, (b) transverse, (c) normal orientation.

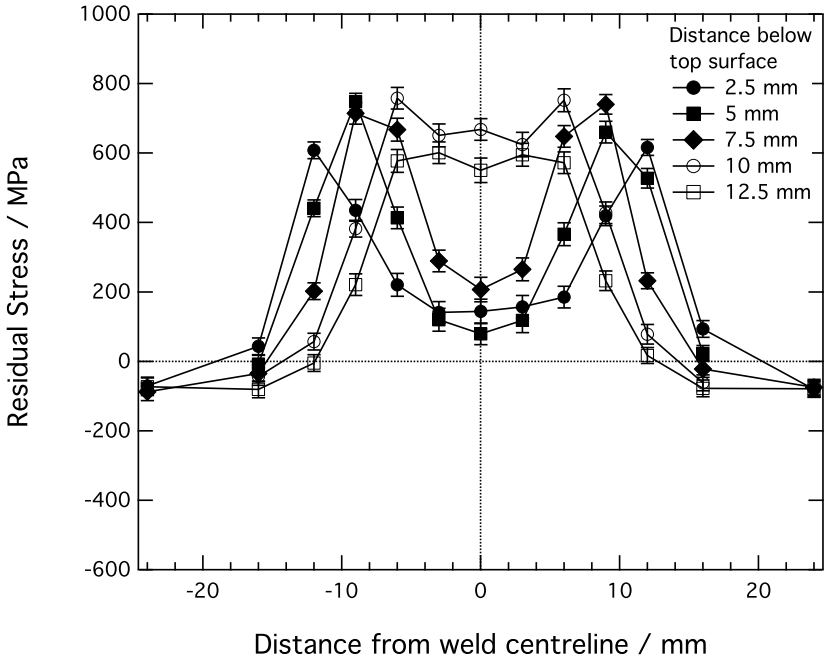

Figure 5.3: Longitudinal residual stress profiles as a function of distance from the weld centreline for a standard, high M_s welding alloy (weld H).

5.3 Multipass LTT welds

Stress contour maps for three welds (A, B and C), welded with a low M_S alloy (LTT-1) are presented in Figs. 5.4, 5.5 and 5.6, showing the longitudinal, transverse and normal stresses respectively. This allows the sequential, redistribution of stresses with additional welding passes to be assessed for each of the different orientations. Welds A–C follow the general trends that were identified for weld H. The stress contours follow the fusion boundary, display symmetry across the weld centreline and are greatest in the longitudinal direction, when compared with the transverse and normal.

Immediately apparent, and in direct contrast to weld H, are the compressive stresses that are observed in the weld metal for all three specimens welded with LTT-1. Compression in both the longitudinal and transverse directions, regardless of the number of passes, provides comprehensive evidence for the benefits of transformation plasticity. The shape deformation and net expansion associated with the $\gamma \rightarrow \alpha'$ transformation have proved sufficient in negating the tensile stresses accumulated during constrained cooling [27]. Although

weld H is subject to the same transformation mechanism as welds A, B and C, the differences in residual stresses are directly related to the difference in filler transformation temperature. Whereas previously stated, the high M_s filler used to produce weld H continues to cool after transformation, the LTT welds complete their transformation at ambient temperature and fully realise the available stress relief.

5.3.1 1–Pass

The longitudinal residual stress contours for weld A are shown in Fig. 5.4a. Compressive stresses, the order of -200 MPa, develop in the central portion of the weld metal and reduce in magnitude, moving radially away from this region. The contours follow the weld geometry and the stress at the fusion boundary is between 0–200 MPa. This value increases, moving into the HAZ where the stress is typically 400 MPa. The highest region of stress (> 600 MPa) is measured below the weld, on the cusp of the HAZ.

The transverse stresses in Fig. 5.5a are similar in distribution to the longitudinal but much smaller in magnitude, around half the values. Minor compression is evident in the weld metal (-100 MPa), covering a very small region and the maximum tensile stress (300 MPa) is again located below the weld deposit on the boundary of the HAZ. Only nominal stresses were registered for the normal orientation, Fig. 5.6a, which were between -100 and 100 MPa. It would appear as though stress generation in the normal orientation is much less effected compared with the longitudinal and transverse orientations. This is due to the top surface of the weld being a free surface, which will have zero stress in the normal direction and reduce constraint during cooling.

Although the direct comparison of weld H with weld A may not be entirely appropriate due to the differing number of welding passes, the change in stress distribution is profound. A conversion from $200 \rightarrow -200$ MPa in the weld metal highlights the significance of the M_s. During the welding process, the surface of the base plate in contact with the deposited molten filler will melt. The liquified base plate, which has a low concentration of alloying elements, will mix with the richly alloyed LTT-1 filler. This will have the effect of reducing

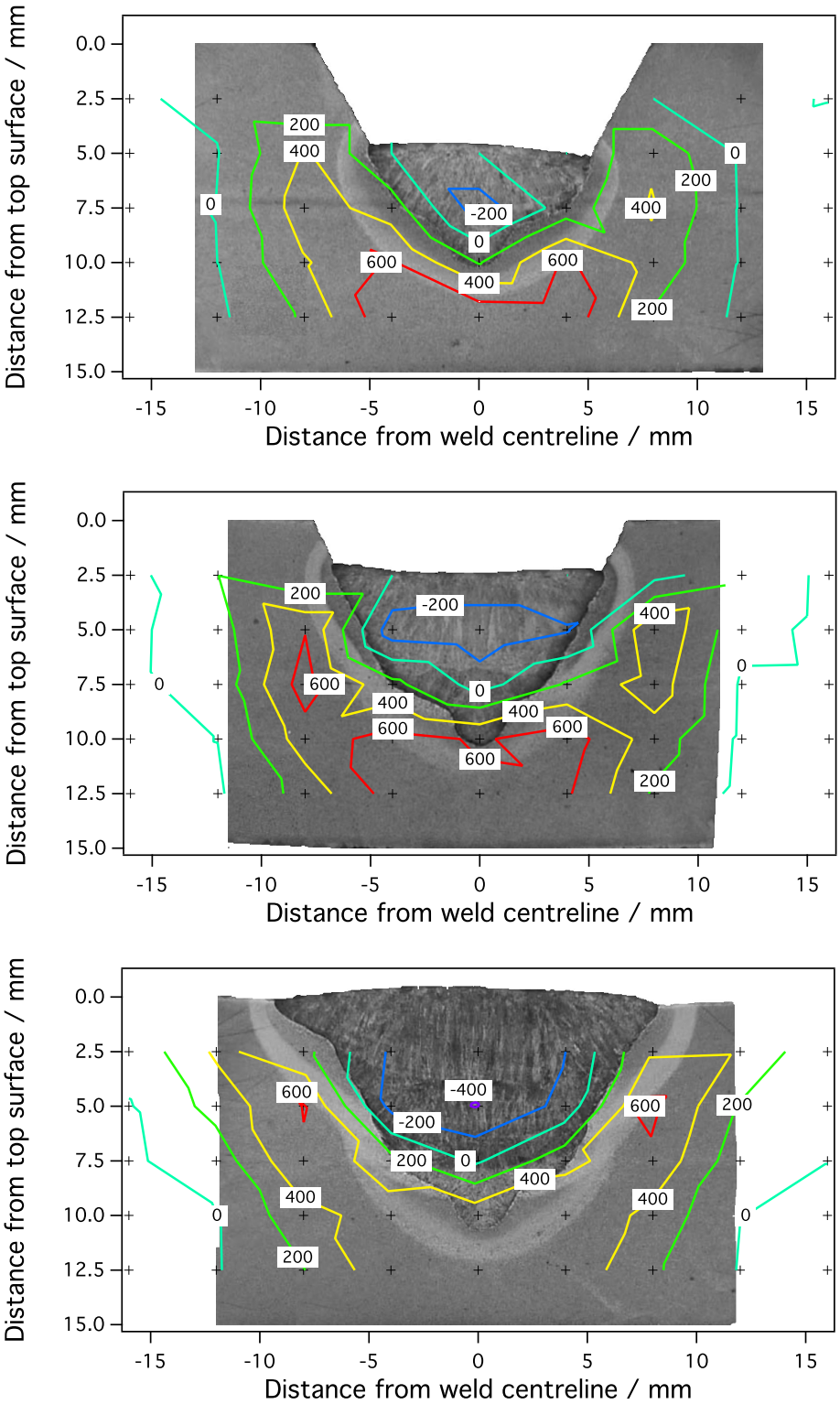

Figure 5.4: Longitudinal residual stress contour maps, in MPa; (a) weld A: 1–pass, (b) weld B: 2–pass, (c) weld C: 3–pass.

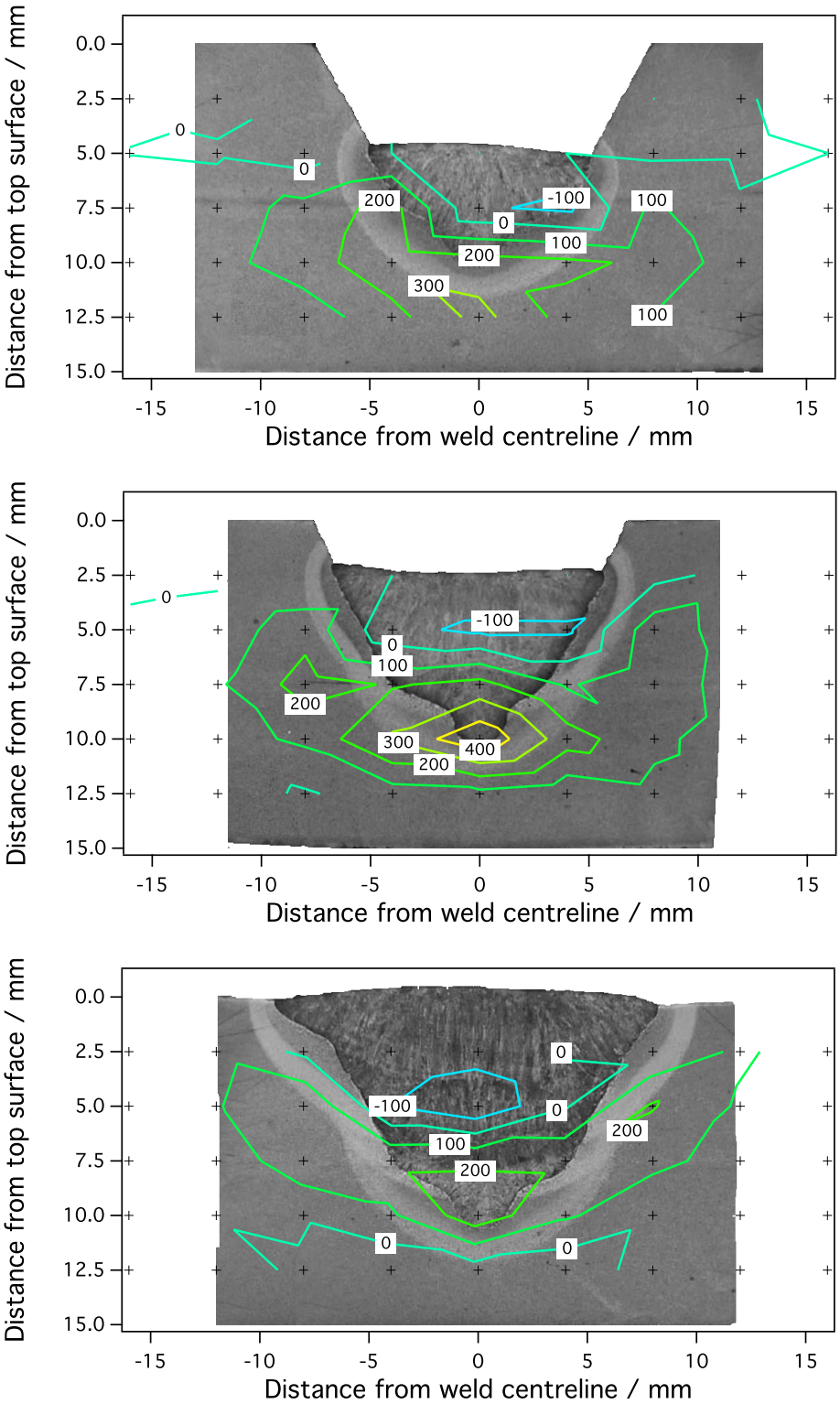

Figure 5.5: Transverse residual stress contour maps, in MPa; (a) weld A: 1–pass, (b) weld B: 2–pass, (c) weld C: 3–pass.

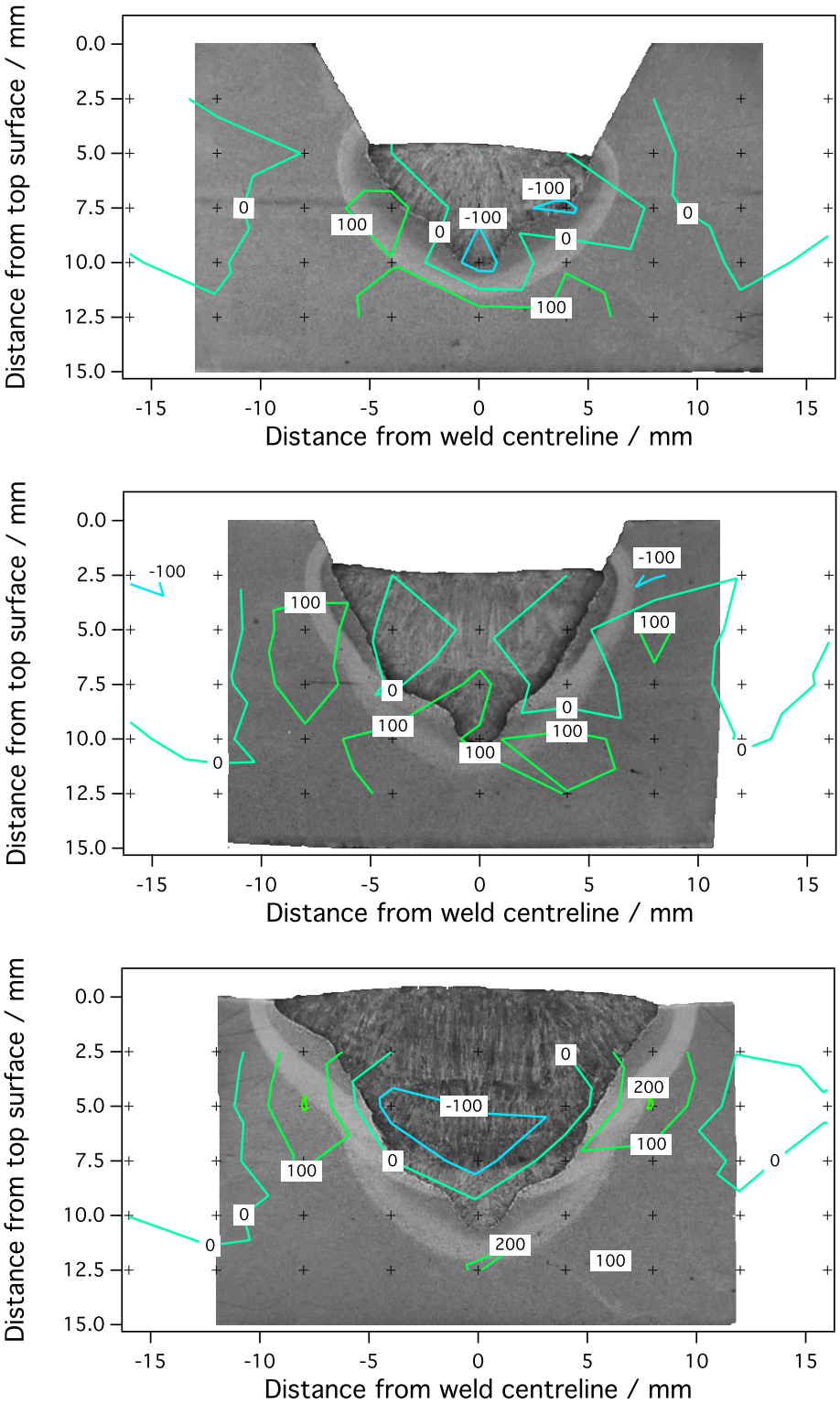

(a)

(b)

(c)

Figure 5.6: Normal residual stress contour maps, in MPa; (a) weld A: 1–pass, (b) weld B: 2–pass, (c) weld C: 3–pass.

the elemental concentration within the weld deposit. The alloying elements in the LTT-1 filler were introduced to suppress the M_s, hence a reduction in alloying concentration equates to an increase in M_s. The extent of dilution associated with a single welding pass (LTT-1 deposited on BP700) is the order of 25% and this equates to an estimated $M_s \sim 230\,^{\circ}\mathrm{C}$ for the material within the confines of the fusion zone. The reduction in M_s from approximately $400 \rightarrow 230\,^{\circ}\mathrm{C}$, (comparing weld H with A) is sufficient to drive regions of the weld deposit into a compressive state.

5.3.2 2–Pass

The longitudinal, transverse and normal stress contours for weld B are presented in Fig. 5.4b, 5.5b and 5.6b respectively. The deposition of an additional layer of weld metal does not disrupt the contours from following the fusion boundary or being reflected about the centreline. The region of compression ($-200\,\mathrm{MPa}$) is enlarged for weld B (cf. weld A), which may be expected due to the increase in quantity of material deposited for the 2–pass weld. Peak tensile stresses ($> 600\,\mathrm{MPa}$) remain below the weld metal and also develop at the side, adjacent to the HAZ. Besides these subtle differences, and of much greater significance, are the changes in stress levels at different depths at 0 mm from the weld centreline. There is a large compressive stress measured for weld A at 7.5 mm below the top surface. This stress is closer to zero for weld B, following a second welding pass. More detail is provided by the longitudinal stress profiles, Figs. 5.7–5.8, which show measurements at exact locations (rather than smoothed contours) and are discussed along with weld C, Fig. 5.9, in the next section.

The transverse stresses for weld B have a slightly larger range ($-100 \rightarrow 400\,\mathrm{MPa}$) compared with weld A ($-100 \rightarrow 300\,\mathrm{MPa}$), with the peak tensile stresses occurring below the weld metal in the vicinity of the HAZ. There is also a small region of compression ($-100\,\mathrm{MPa}$) in the weld metal, similar to weld A. The stress at 7.5 mm below the top surface, along the weld centreline is mildly compressive for weld A and tensile ($\sim 200\,\mathrm{MPa}$) for weld B. Thus promoting the idea that underlying welding passes benefit from transformation plasticity when first deposited but behave as inert base material for subsequent layers.

The range of normal stresses in weld B are relatively low ($-100 \rightarrow 100$ MPa) compared with the longitudinal and transverse orientations.

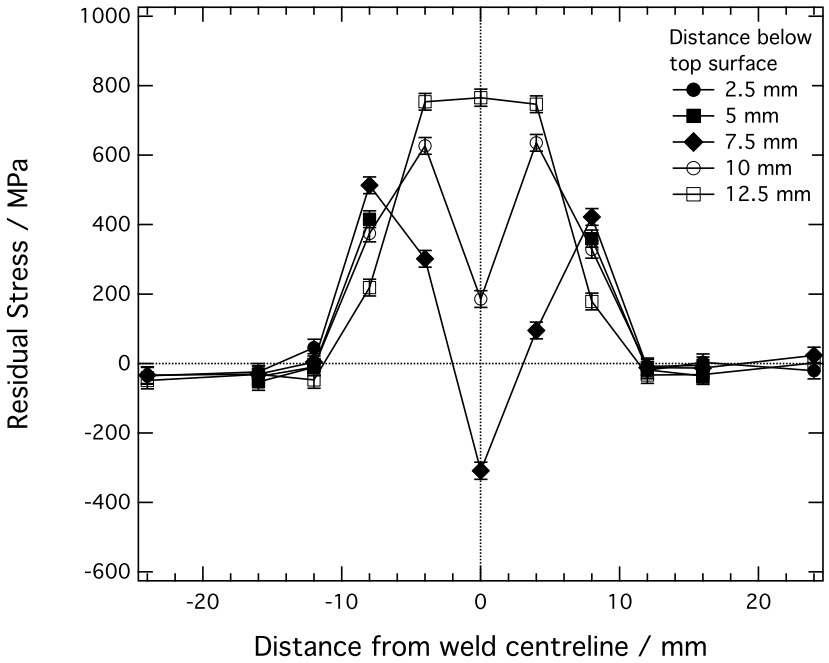

Figure 5.7: Longitudinal residual stress profiles as a function of distance from the weld centreline (weld A: 1–pass).

5.3.3 3–Pass

The longitudinal stress contours for weld C are presented in Fig. 5.4c. The addition of a third layer further increases the quantity of LTT-1 weld metal and contributes to an increase in size of the compressive region (-200 MPa), when compared with the 1– and 2–pass welds. The magnitude of compression is also increased, recording -400 MPa at a single measurement location. The results would indicate that the LTT-1 welding alloy is capable of inducing compressive residual stresses in the weld metal for both single and multipass welds. The contour arrangements for all three welds in this orientation are also very similar.

The only minor difference are the high stress levels (> 600 MPa) that previously accumulated below the weld deposit for the 1– and 2–pass welds, which are no longer present with 3–passes. High tensile stresses are expected to de-

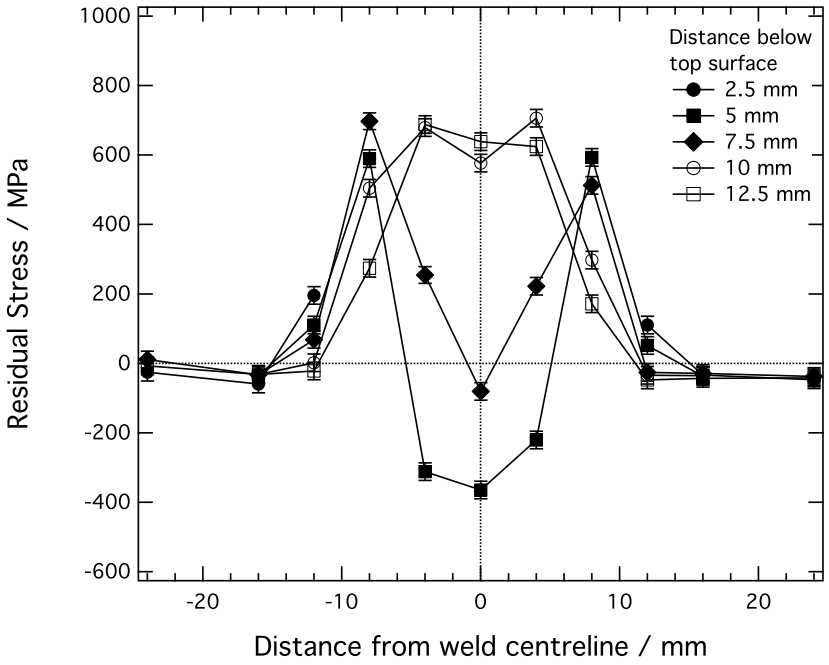

Figure 5.8: Longitudinal residual stress profiles as a function of distance from the weld centreline (weld B: 2–pass).

velop below the weld, as this region restricts shrinkage of the cooling weld metal [134]. However, a slight alleviation of stress in this region would be sufficient to reduce it below the 600 MPa value. The contour maps in isolation do not fully represent the stress distribution and should be viewed in conjunction with the stress profiles. These show a gradual decline in stress at depths of 10 and 12.5 mm below the top surface, at the weld centre, with increasing numbers of passes. The tensile stresses at these positions are actually ~ 550 MPa for weld C.

The transverse stresses measured for weld C, Fig. 5.5c, develop lower tensile peaks ($-100 \rightarrow 200$ MPa) compared with weld A and B. This follows the same trend as the longitudinal stresses in the region surrounding the bottom of the weld deposit. As for the previous welds, the residual stresses are very low in the normal orientation, $-100 \rightarrow 100$ MPa, with a few single measurements at 200 MPa.

Through comparison of the contour maps for weld C and H it is possible to assess the extent of weld filler M_s on the stress distribution for butt–welded

ferritic steel plates. The difference is profound. With respect to the longitudinal stress, the weld deposit for weld H is entirely tensile in nature, whilst the same region measured in weld C is almost completely in compression. In addition, the effect of transformation plasticity in the fusion zone is able to influence the stress distribution in the surrounding HAZ. The large region of tensile stress ($> 600\,\text{MPa}$) that developed in weld H has diminished significantly in weld C. Crucially, the peak tensile stresses have shifted from the location approaching the top surface (weld H, 2.5 mm depth) to deeper within the bulk of the base plate (weld C, 5 mm depth). This is pertinent from a fatigue performance perspective because of the propensity for crack initiation at the weld toe. Moving away from the weld centreline beyond the HAZ, the contours are relatively similar for both welds. The difference in residual stress arrangement for the two welds is also minimal in the transverse and normal orientations.

It has already been noted in Section 5.3.2 that the underlying layers in multipass welds are affected by subsequent deposits. This concept is more fully appreciated by studying the stress changes at specific measurement locations in the 1–, 2– and 3–pass welds, welded with the LTT-1 filler, Figs. 5.7–5.9. Considering the initial longitudinal stress at 7.5 mm below the top surface for weld A, which is $\sim -300\,\text{MPa}$. The stress in weld B following the 2nd pass at the same position is $\sim -80\,\text{MPa}$. For the 3–pass weld (weld C), the stress is less affected but further reduces to $\sim -30\,\text{MPa}$. At a depth of 10 mm, the stress changes from $\sim 185\,\text{MPa}$ for 1–pass to $\sim 550\,\text{MPa}$ for both the 2– and 3–pass welds. Although the gauge volume at this depth would include some base plate, the two sets of results indicate that underlying passes become more tensile in nature following additional deposits.

Whilst the $\gamma \rightarrow \alpha'$ solid-state transformation of the filler has relaxed the residual stresses in a single pass, the thermal cycles of subsequent weld deposits have not provided sufficient heat to retransform previous layers. Therefore thermally-induced strains have accumulated in the previous welding passes. However, considering the error bars, there is no apparent stress change at a depth of 5 mm for the 2– and 3–pass welds and it remains at $\sim -400\,\text{MPa}$. This is not consistent with the above theory but may be explained in terms of the

interpass temperature in the next section. The results would also suggest that there is a greater change in stress between passes 1–2 compared with passes 2–3. This latter observation is consistent for a limited number of welding layers but may require further investigation with many more passes to establish a clear trend with respect to the stress change between different passes.

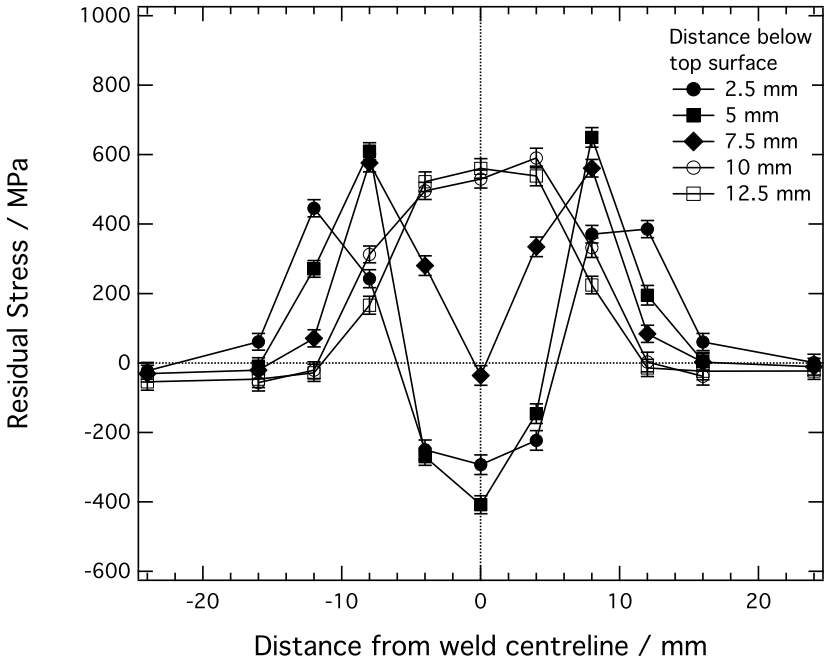

Figure 5.9: Longitudinal residual stress profiles as a function of distance from the weld centreline (weld C: 3–pass).

5.4 Interpass Temperature

Integral to the multipass welding procedure is the interpass temperature, i.e. the temperature at which the weld is maintained between layers being deposited. As introduced in Fig. 5.1, the interpass temperature has the capacity to significantly influence the residual stress distribution. This is based on whether the $\gamma \rightarrow \alpha'$ transformation occurs for each individual layer following their deposition or all layers transform simultaneously as a complete weld deposit after the final pass. In order to investigate this phenomenon, welds K and L were produced with different interpass temperatures but otherwise subjected to the same manufacturing conditions. For weld K the $M_S > T_I$

causing each layer to transform individually but for weld L where the $M_S < T_I$ the entire weld deposit will transform as a single entity.

Both welds, although being identical in geometry and composition, show profoundly different residual stress distributions, Figs. 5.10–5.12. Weld K produces a notable region of longitudinal compression, the order of −400 MPa, at depths of 2.5–5 mm at the weld centreline. This changes abruptly into a large tensile stress ($\sim$ 600 MPa) at a depth of 7.5 mm, which continues through the weld metal and into the HAZ below. The compressive stress in weld L is comparatively lower in magnitude, ~ -200 MPa, but covers a much larger region and remains in compression at 7.5 mm. These differences in stress distribution are a consequence of the selected interpass temperatures with respect to the M_S temperature (Fig. 3.3).

For weld K, the undiluted filler $M_S \simeq 165\,^{\circ}$C and the interpass temperature was set at $T_I = 45 - 50^{\circ}$C, producing $\sim 90\%$ of the product phase. Following deposition, each layer transforms into martensite before another is added. Only those regions of the first layer which happen to reaustenitise due to the heat from the subsequent layer can contribute to transformation plasticity. The remainder of the first layer simply contributes to constraint and accumulates thermally-induced strains. The beneficial stress system introduced when the first layer was deposited, is therefore lost or reduced. In contrast, the interpass temperature of weld L was kept between the range of 200–240 °C. The weld metal should remain fully austenitic, only to form martensite after all of the layers are deposited and the welded plate is finally allowed to cool below the M_S. The martensitic transformation of the entire weld then ensures that the benefits of transformation plasticity are optimally exploited, thus producing persistent compression in the weld metal at the weld centreline.

The transverse stresses, Fig. 5.13, measured for welds K and L replicate the trends displayed in the longitudinal direction but over a less extreme stress range $\Delta\sigma$. For weld K, $\Delta\sigma \sim -200 \rightarrow 400$ MPa, compared with weld L, $\Delta\sigma \sim -400 \rightarrow 600$ MPa. Weld K once again has a region of high compressive stress at the centreline at a depth of 5 mm, which changes abruptly to a high tensile stress by 7.5 mm below the surface. Weld L has milder compression in

the weld metal and gradually changes to tension with increasing depth. Similar to the longitudinal orientation, weld L develops its highest transverse stresses at a depth of 7.5 mm in the HAZ. This is useful information when designing a welding procedure to improve fatigue performance. Weld K has its peak tensile stresses at 5 mm depth, which may indicate that weld K is more likely to experience higher tensile stresses at the surface of the weld. Remarkably, even the stresses measured in the normal orientation, Fig. 5.14, are in accord with the longitudinal and transverse. The magnitude of the normal stress range for weld K and L continues to diminish to almost half that of the transverse direction but the same relative stress gradients exist.

The fact that weld L does indeed remain largely austenitic prior to cooling to ambient temperature after the final pass is clear from the images presented in Fig. 5.15. The columnar austenite grains terminate at layer junctions in weld K, whereas they are continuous across the second and third layers in the case of weld L. A more detailed view of the grain continuation across the layer boundaries is provided in Fig. 5.16. This is a classic replication of the effect observed when welding austenitic stainless steels, where the lengthy columnar grains extend completely across welds by epitaxial growth since no nucleation is needed when subsequent layers are deposited [135].

On a thermodynamic basis, the first solid to form is δ-ferrite, which is subsequently replaced by columnar austenite grains [136]. For the LTT alloys, solidification usually consists of a mixture of δ-ferrite and austenite at the fusion surface [26, Chapter 9]. When the interpass temperature is sufficiently high, such that the substrate consists of columnar austenite grains, the increase in temperature due to the deposition of a subsequent layer leads to the formation some δ-ferrite. However, the original austenite grains continue to grow and eventually consume the δ-ferrite, thus leading to a continuity of γ grains across weld beads. In contrast, when an interpass temperature below the M_S is implemented, new austenite grains are generated during heating, thus destroying any possibility of γ-continuity across the layers.

It should be noted that the M_S of the first deposited layer is higher than the subsequent layers by virtue of compositional dilution with the base plate.

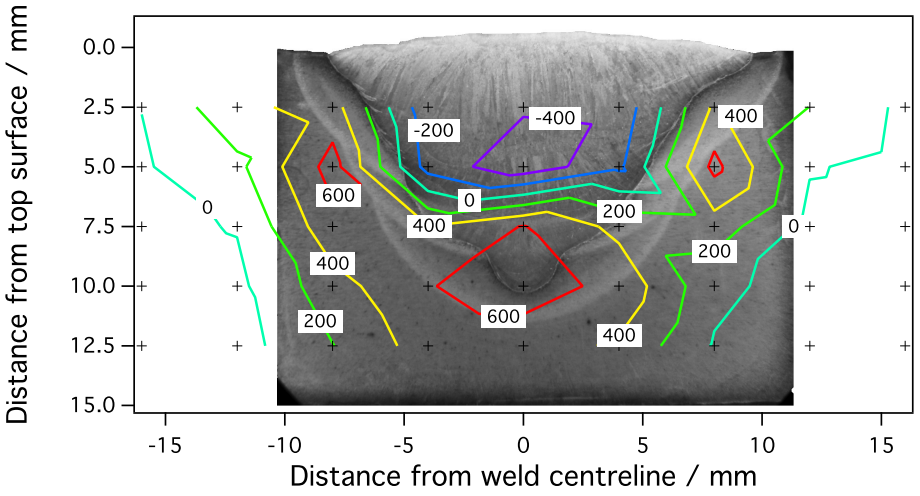

Figure 5.10: Longitudinal residual stress contour maps, in MPa; (a) weld K: $M_S > T_I$, (b) weld L: $M_S < T_I$.

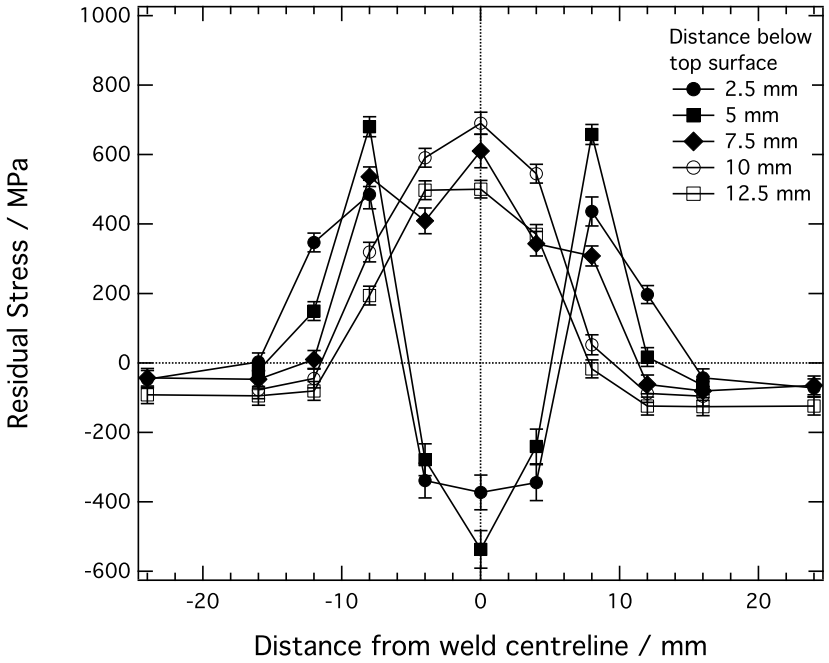

Figure 5.11: Longitudinal residual stress profiles as a function of distance from the weld centreline (weld K: $M_S > T_I$).

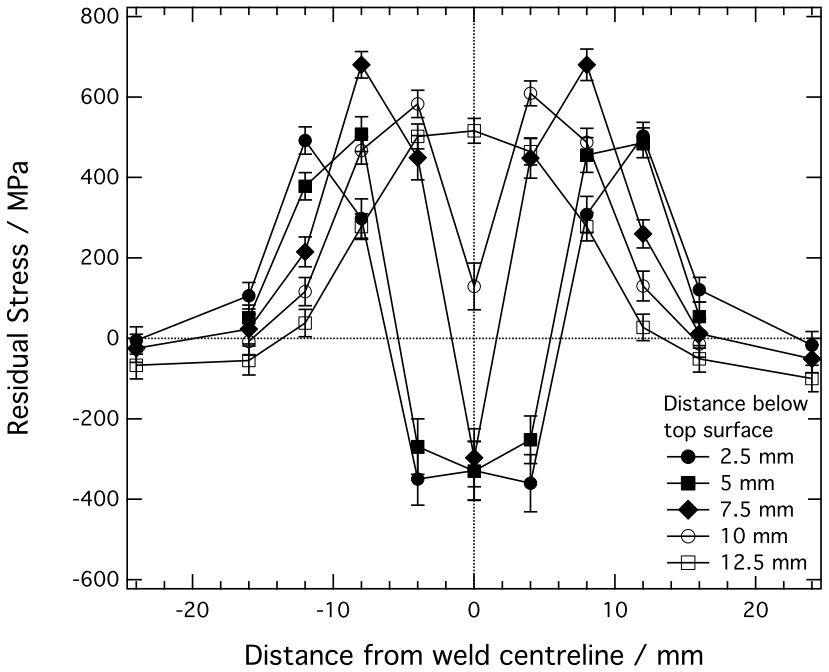

Figure 5.12: Longitudinal residual stress profiles as a function of distance from the weld centreline (weld L: $M_S < T_I$).

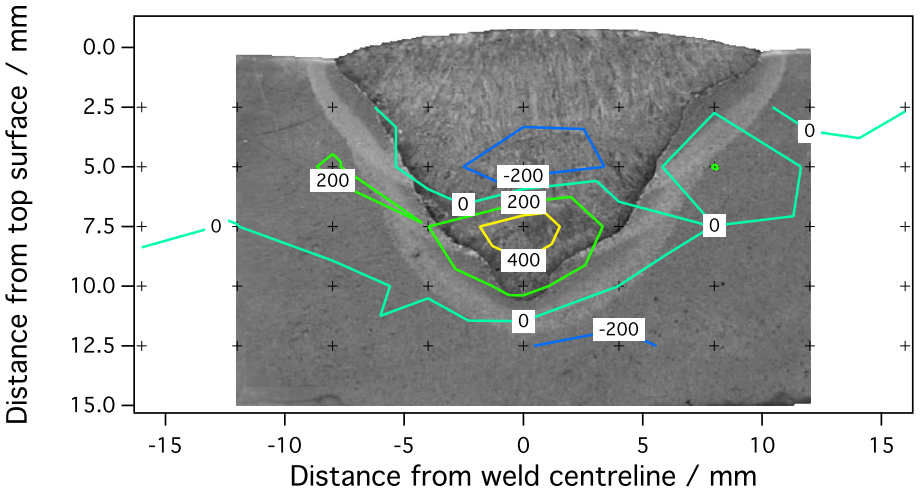

(a)

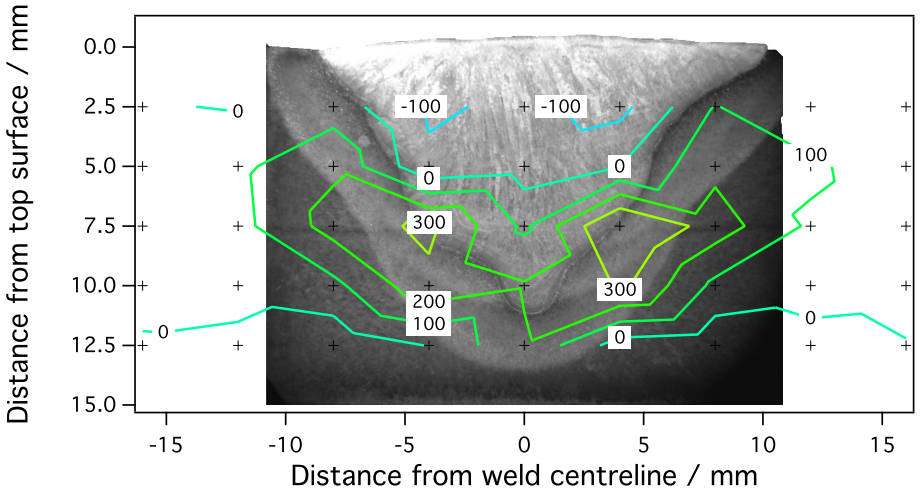

(b)

Figure 5.13: Transverse residual stress contour maps, in MPa; (a) weld K: $M_S > T_I$, (b) weld L: $M_S < T_I$.

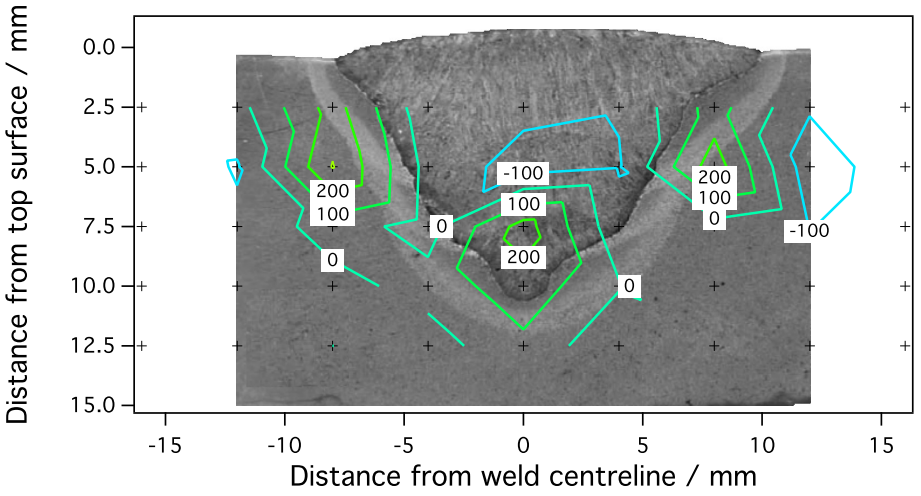

(a)

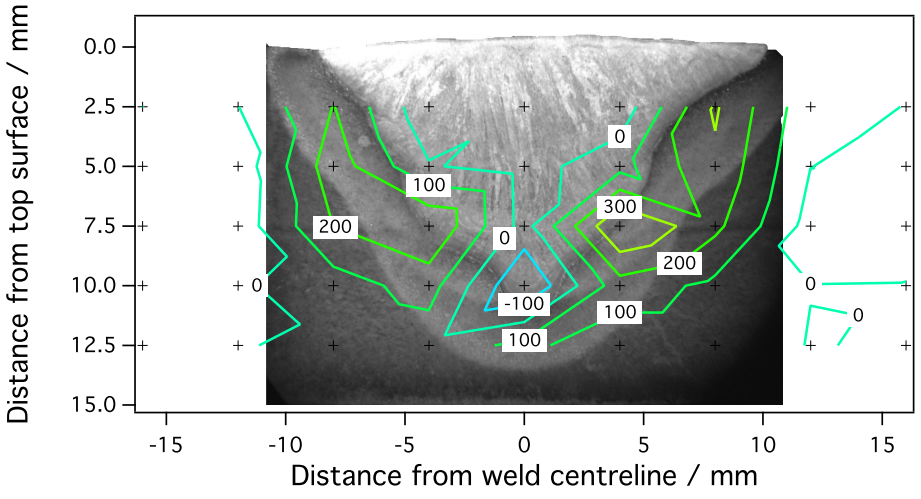

(b)

Figure 5.14: Normal residual stress contour maps, in MPa; (a) weld K: $M_S > T_I$, (b) weld L: $M_S < T_I$.

(a)

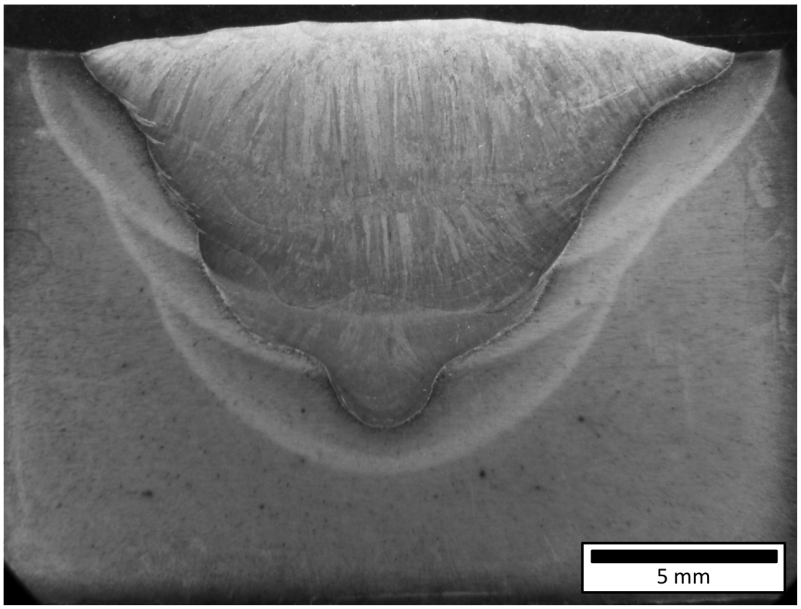

(b)

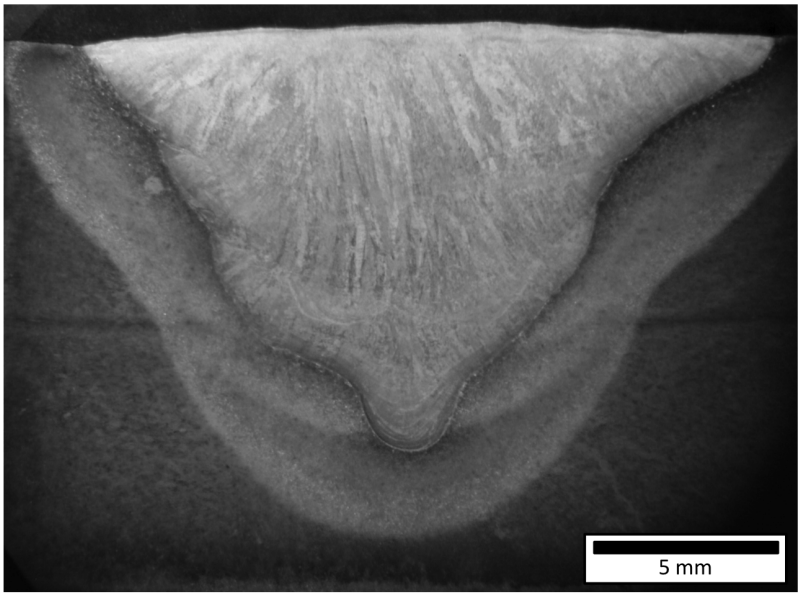

Figure 5.15: Macrostructures of (a) weld K: $M_S > T_I$, (b) weld L: $M_S < T_I$.

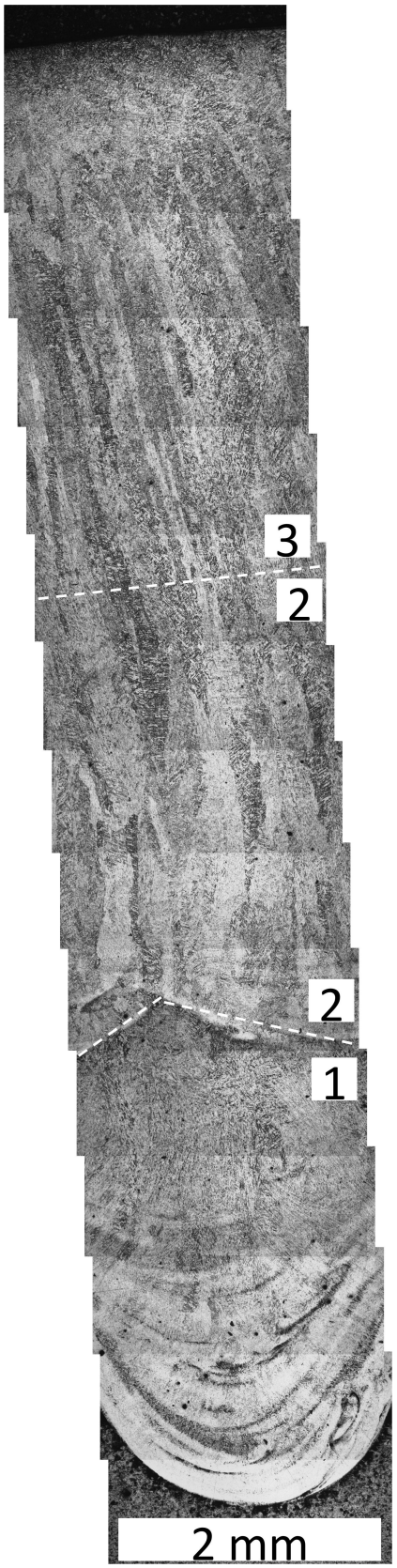

Figure 5.16: Microstructure of weld L at the centreline, from the weld root to the top surface highlighting the boundaries between layers.

Considering the reduction of filler alloy concentration measured by EMPA for weld C, the M_S may increase to around the interpass temperature for weld L. If the $M_S > T_I$, continuity of columnar grains across the fusion boundary into the second layer will not occur. However, the M_S is in very close proximity to the T_I so that the majority of the first pass will remain as untransformed γ until all three layers have been deposited and transformation to martensite occurs with final cooling. This is indicated by the residual stress contours. In order to maintain a more uniform M_S across the multipass weld, a more highly alloyed weld filler, such as LTT-2, should be used for the first layer. Indeed, dilution will occur with the deposition of each new layer, causing the M_S to vary, but it is most significant for the first layer and reduces with the number of passes.

There is a good correlation between the changes in the longitudinal stress profiles across welds C, K and L (Figs. 5.9, 5.11-5.12) and their varying interpass temperatures. Weld K ($T_I \approx 50\,^{\circ}\mathrm{C}$) shows compressive residual stresses of around $-400\,\mathrm{MPa}$ in the weld material at depths of 2.5 and 5.0 mm along the weld centreline, which change abruptly to a large tensile stress of $\sim 600\,\mathrm{MPa}$ at a depth 7.5 mm and remains tensile with increasing depth into the base plate. Weld C ($T_I \approx 120\,^{\circ}\mathrm{C}$), displays slightly less extreme stress values in the weld material but the profiles follow the same trend as for weld K, the only difference being the approximately zero stress value recorded at 7.5 mm depth.

As the interpass temperature is raised above the M_S in weld L ($T_I \approx 240^{\circ}\mathrm{C}$) the stress at 7.5 mm depth becomes compressive, being $\sim -300\,\mathrm{MPa}$, and the value at 10 mm depth falls to below 150 MPa. Weld K has an interpass temperature sufficiently below the M_S to cause each individual welding pass to transform to martensite prior to the next layer being deposited. Weld L has a sufficiently high interpass temperature such that all passes transformed collectively. Weld C, with an intermediary interpass temperature displays stress profiles between the two extremes, this is explained by the transformation of austenite to martensite occurring over a temperature range, rather than at an absolute value [64]. Applying an interpass temperature between M_S and M_F permits the formation of some martensite, which will be tempered by the subsequent welding pass and contribute towards improved toughness.

The intermediary interpass temperature associated with weld C would also explain the apparent anomaly of a constant compressive stress at a depth of 5 mm at the weld centreline for the 2– and 3–pass welds in Section 5.3.3. If $T_{\mathrm{I}} \approx 120\,^{\circ}\mathrm{C}$, the 2nd pass would not have completed its transformation to martensite. Therefore, some of the benefits of stress-relief in the 2nd pass will remain until the final pass is deposited. It is also fascinating to note the initial longitudinal residual stress distribution created by the deposition of a single welding pass, Fig. 5.4a, and then to observe the subsequent contrasting evolution of stresses, as the weld is filled, based on the preheat/interpass temperature.

5.5 Conclusions

A study of the residual stress distributions produced around arc welds fabricated with a martensitic weld filler, that transforms at a low temperature have been performed using neutron diffraction; specifically identifying the evolution of stress with increasing number of passes and varying interpass temperatures.

A low M_s welding alloy has been shown to be capable of inducing compressive residual stresses in the weld metal of both single and multipass welds. This is in direct contrast to the tensile residual stresses developed in the weld metal of a standard, high M_s filler for a multipass weld.

The measurement of sequential changes in residual stress distribution for a low M_s 1–, 2– and 3–pass weld have shown how the stress state of underlying layers can be altered. Compressive stresses developed in the first welding pass can be eradicated by the deposition of additional layers if the majority of the underlying weld material is not austenitised by the heat input of the new layer.

If $T_I > M_S$ for all welding passes, the entire weld remains austenitic until all of the layers have been deposited. It therefore becomes possible to exploit the stress reduction benefits that can be derived from the transformation plasticity of each and every layer. Conversely, if $T_I < M_S$ the deposition of new weld metal leads to increasingly tensile stresses in the underlying layers, thus reducing or eliminating the beneficial stress state previously created.

A more highly alloyed weld filler should be used for the first deposited layer to compensate for dilution with the base material and maintain a uniform M_S across all welding layers. A uniform M_S would also ensure that the initial layer transforms simultaneously with any subsequent passes for a specified preheat/interpass temperature.

Steep stress gradients exist across the weld, especially at fusion boundaries. This may necessitate a smaller gauge volume and an increased concentration of measurement points in these regions to accurately determine the abrupt changes in stress for welded components.

Chapter 6

Weld Optimisation

6.1 Introduction

The effect of multiple depositions on the residual stress generation for ferritic steel welds joined with an LTT filler has been established along with the influence of interpass temperature. This has provided a basis for further investigation in order to understand the consequences of different filler arrangements and base plates in an effort to optimise stress distribution. A welding electrode is not used in isolation but is selected for specific applications, in combination with the material to be joined. The strength of the welded fabrication is often of particular interest and will dictate its industrial usage. It is therefore necessary to identify stress evolution as a function of base plate strength.

In addition, the effects of fillers with different alloying concentrations is pertinent to weld optimisation. The use of an extensively alloyed weld metal (LTT-2) has been proved to enhance fatigue performance in single-pass joints [18]. However, the extent of stress relief that can be derived from transformation plasticity may be reduced due to incomplete austenite–martensite reaction when further layers are deposited. Dilatometry results for LTT-2 suggest that the M_S occurs at approximately ambient temperature. Although dilution of the filler with the base plate will occur in the initial deposits, this could be problematic with regards to untransformed austenite, and hence reduced stress relaxation, in the final welding passes (weld F).

The purpose of the work presented here was to elucidate these issues through characterisation of the residual stresses produced as a function of the transformation characteristics of the different weld metal combinations and the mechanical strength of the base plate. Four 3–pass welds (F, G, M, N) were prepared from three different steel plates with three different welding consumables, Fig 3.3. The results are also compared with the two welds (C, H) from the preceding chapter. Weld N has a base plate (BP355) that has a yield strength lower than that of the LTT-1 filler, for weld M (BP960) the reverse is true, Table 3.2. Weld G has underlying layers deposited from a standard, high M_S electrode with a final LTT-2 capping pass to assess the stress benefits while limiting the use of these relatively expensive LTT consumables.

Stress Characterisation

Lattice spacings were recorded in the longitudinal, transverse and normal directions for each of the welded plates and reference comb specimens. Again, the original measurement locations are indicated with crosses and the strains at these positions were used to map the stresses across the weld bead, HAZ and into the base plate at depths of 2.5–12.5 mm below the surface. The stress contours show symmetry across the weld centreline and follow the geometry of the weld, Figs. 6.1, 6.6, 6.8, 6.9. They are complemented by longitudinal stress profiles, Figs. 6.2, 6.7, 6.10, 6.11.

Compressive stresses are evident in the LTT weld metal for all four specimens (longitudinal direction). This confirms the effect of the shear and dilatational strains associated with the $\gamma \rightarrow \alpha'$ transformation. The stresses developed in the transverse and normal directions show evidence of compression in the LTT weld material but they are much lower in comparison. With respect to the longitudinal direction, the four welds have a common stress distribution with compression in the weld metal nearer the surface and peak tensile stresses in the HAZ both below and either side of the weld. The tensile stresses are generated as a result of stress equilibration and a high M_S at these locations. The re-austenitised regions in the base plate that surround the fusion boundary will transform to martensite at an elevated temperature, thus accumulating tensile residual stresses during the subsequent thermal contraction on cooling.

Particular attention should be paid to the stresses nearest the specimen surface and at the fusion boundary, where fatigue failure predominantly occurs. An additional investigation was completed regarding the issue of steep stress gradients across the fusion boundary/HAZ and the number of measurement positions necessary to adequately describe the stress change.

6.2 Dilution Effects

The longitudinal stress contours for weld F, Fig. 6.1a, are between the range of $-200 \rightarrow 600$ MPa. Although, the region of compression that is evident in the weld metal is for a single point. Also, the peak tensile stress (600 MPa) covers a relatively small area in the HAZ or in its vicinity and are recorded as being away from the sample surface. The large band of stress at 400 MPa surrounds the HAZ while the majority of the fusion zone is approximately zero stress, Fig. 6.2. This is in contrast with weld H, Fig. 5.2a, which was fabricated with a high M_S filler, and develops tensile stresses in both the weld deposit and surrounding base material. The contours for weld F are more akin to weld C, Fig. 5.4c, in terms of the tensile stress distribution in the HAZ and regions away from the weld. The major difference is that a significant portion of the weld metal in weld C is in a compressive state.

The transverse stresses for weld F, Fig. 6.1b, are within a much tighter range ($-100 \rightarrow 300$ MPa) compared with the longitudinal orientation. The most extreme values are restricted to individual points and the vast proportion of measurements fall between $0 \rightarrow 200$ MPa. There are regions of tension in the central bulk of the weld metal and the contour arrangement is less symmetrical than for welds C and H. The normal direction (weld F), Fig. 6.1c, has an even lower stress range ($-100 \rightarrow 100$ MPa), which is similar to welds C and H. There are a few points that record the slightly higher stress of 200 MPa for the latter two samples in the normal orientation.

Welds H, C and F were welded with increasingly alloyed fillers and hence, decreasing M_S. Due to the tensile stresses developed in the weld metal for weld H (HTT-1) and the compression in the same region for weld C (LTT-1),

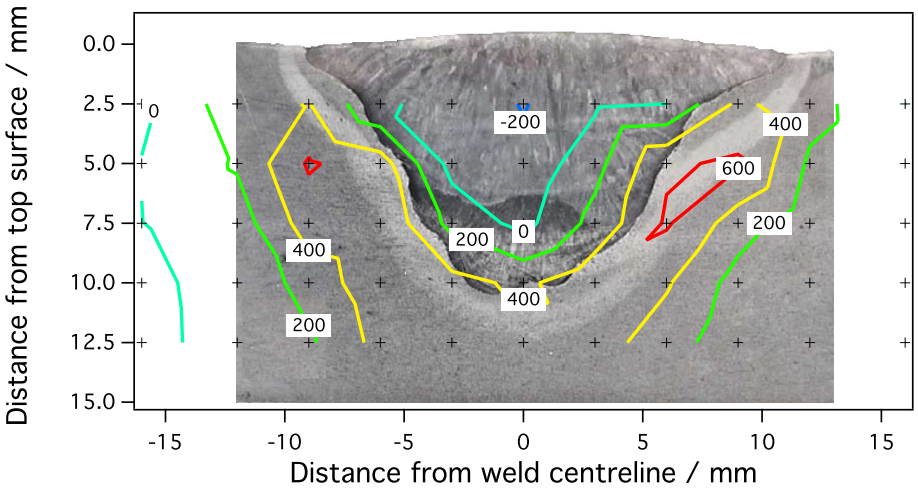

(a)

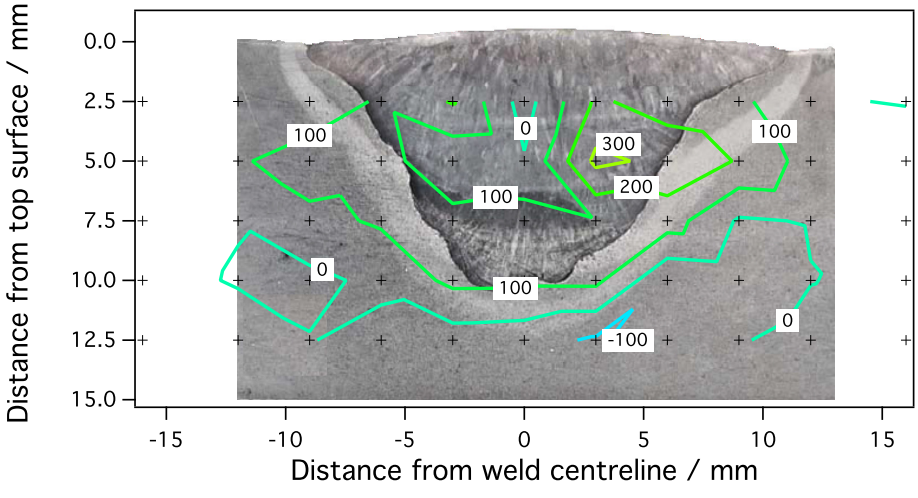

(b)

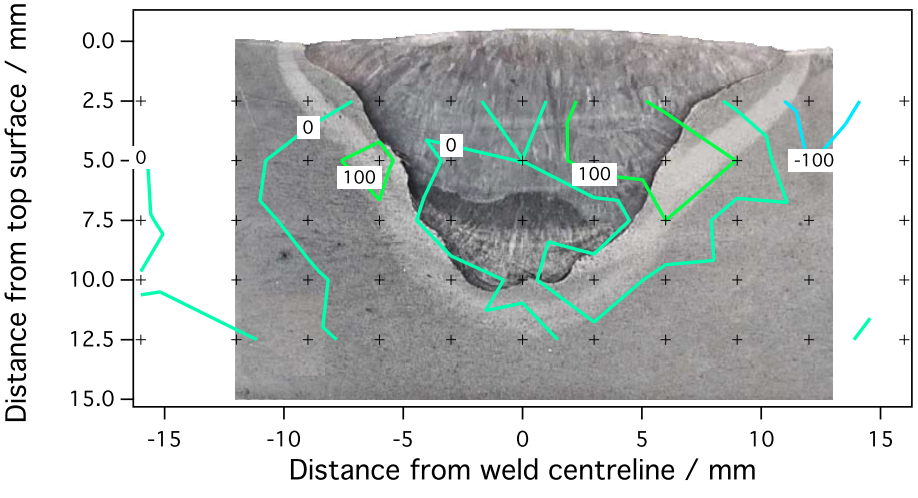

(c)

Figure 6.1: Residual stress contours for a very low M_s welding alloy (weld F), in MPa; (a) longitudinal, (b) transverse, (c) normal orientation.

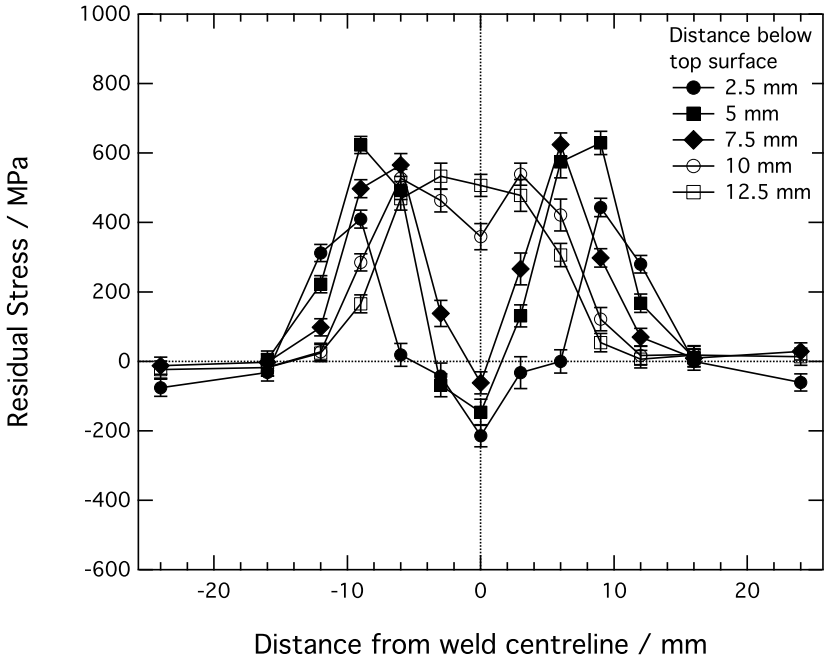

Figure 6.2: Longitudinal residual stress profiles as a function of distance from the weld centreline for a very low M_{s} welding alloy (weld F).

it might be expected that weld F, which has an even lower M_{S}, exhibit greater compressive stresses. The longitudinal stress profiles measured at a depth of 2.5 mm for welds H, C and F, Fig. 6.3, are inconsistent with this hypothesis; weld G is also included but discussed later.

All of the specimens welded with an LTT electrode display the same characteristics with compression in the weld metal and peak tensile stress in the adjacent HAZ. The magnitude of compression in weld C is greater than weld F. This is caused by untransformed austenite in the deposited metal for weld F, resulting from the heavily alloyed LTT-2 filler that has an overly suppressed M_{S} [11]. The full exploitation of transformation plasticity cannot be achieved through the partial transformation of austenite–martensite, so only minor compressive stresses can develop. Both weld C and F have lower peak tensile stresses than weld H.

In order to illustrate this point, Fig. 6.4 provides a schematic diagram of the effect of M_{S} on the residual stresses produced in three different welding alloys during a constrained cooling situation. A bar of each alloy is cooled from a

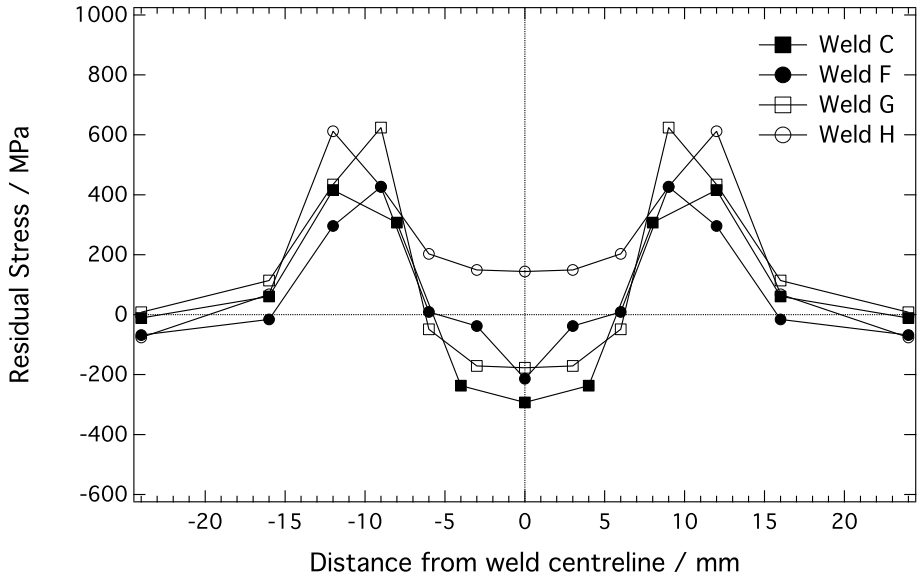

Figure 6.3: Averaged longitudinal residual stress profiles at 2.5 mm below the top surface as a function of distance from the weld centreline. Welds H, C and F had a decreasing M_S, weld G had an LTT-2 capping pass.

stress-free state at high temperature with the ends of the bar fixed, preventing any thermal shrinkage. This is an idealised model of the constrained cooling that occurs in the weld and HAZ during welding [137]. The welding filler with a high M_S transforms prematurely, which leads to tensile residual stress in the weld metal as it continues to thermally contract until it reaches ambient temperature.

The filler with an overly suppressed M_S, such that the $\gamma \rightarrow \alpha'$ transformation is largely incomplete at ambient temperature, achieves only partial stress relaxation. Although, this is preferable to a tensile residual stress being generated. The curve is shown to pass through zero stress at ambient temperature, generalising the results from weld F. The 'ideal' filler transforms at the optimum temperature to allow complete transformation, which results in maximum stress alleviation to the extent of inducing large compressive stress in the weld metal. The triaxial stress state that exists in a welded body will influence the shape of the schematic, uniaxial curves but the concept of setting an appropriate M_S that is neither too high or low remains applicable.

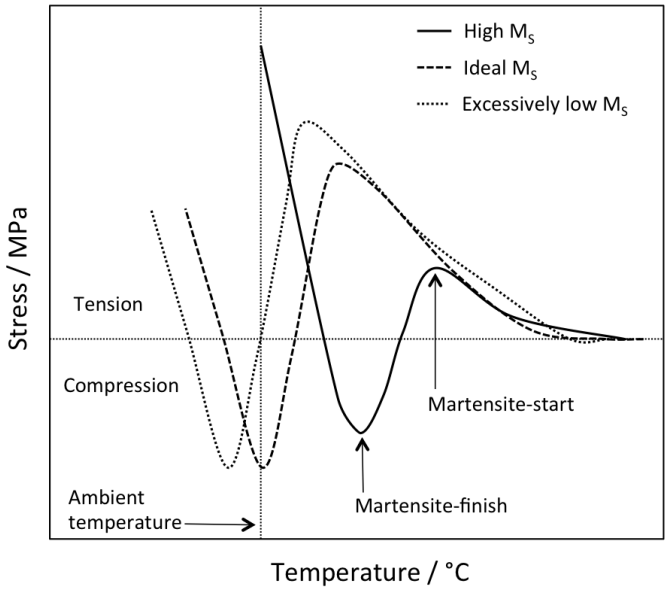

Figure 6.4: Schematic illustration of the residual stresses for three welding alloys with differing M_S, highlighting the effect of an overly suppressed M_S.

The macrograph in Fig. 6.5 shows evidence of continuous columnar grains growing across the fusion boundary between welding passes 2–3, which would indicate that the M_S of the weld bead in this region is similar to the interpass temperature. The welding alloy developed by Karlsson *et al.* [18] to compensate for dilution with the base plate displays greater fatigue performance than the standard LTT alloy. Importantly, this is for single-pass welds where the extent of dilution is typically 30% and elevates the M_S. However, LTT-2 may be not suitable as the sole filler for multipass welds since its undiluted M_S is too low for complete transformation.

6.3 LTT Capping Pass

The stress contours for weld G, which incorporated a single capping pass of LTT-2, are displayed in Fig. 6.6 and the boundary between the LTT-2 surface layer and the preceding HTT-1 deposit is clearly evident (c). Observing the longitudinal stress distribution, it is interesting to note that the contours follow the geometry of the fusion boundary but are additionally influenced by the LTT/HTT interface. The desired accumulation of compressive stress is

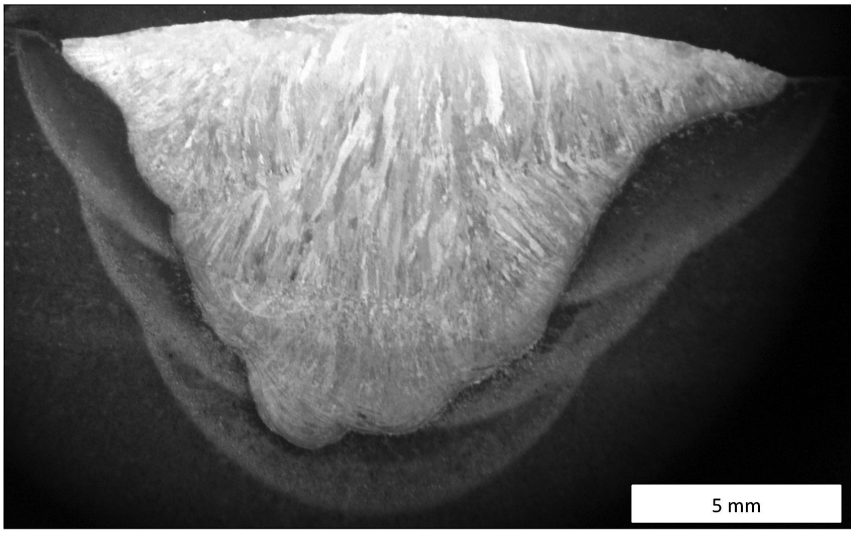

Figure 6.5: The macrostructure of weld F reveals the boundary between layers and the growth of columnar grains across passes 2–3.

developed in the LTT weld metal (−100 MPa) but the surrounding material is tensile in nature. Almost the entire HAZ is in a state of tension (> 600 MPa) and adopts an arrangement synonymous with weld H. In fact, the peak tensile stresses for weld G are ∼ 700 MPa, Fig. 6.7, and it is striking how the measurements in the HTT filler are all tensile and only the LTT alloy is in compression (at a depth of 2.5 mm).

The contours in the transverse direction of weld G reveal a large band of tensile stress (> 200 MPa) right across the HTT-1 deposit, into the HAZ and base material. The zero stress contour follows the LTT-2 surface pass interface very closely. Although there were similarities between the longitudinal stress arrangements between weld G and H, this is not observed for the transverse orientation. An unusual tensile peak of 600 MPa was detected along the fusion boundary at a depth of 5 mm (weld G), the value was not repeated at the corresponding location on the other side of the weld centreline. This presents an anomaly and could potentially be either the result of an experimental error or a microstructural feature that has influenced the lattice spacing. However, the size of the gauge volume means that a region of excessive segregation or

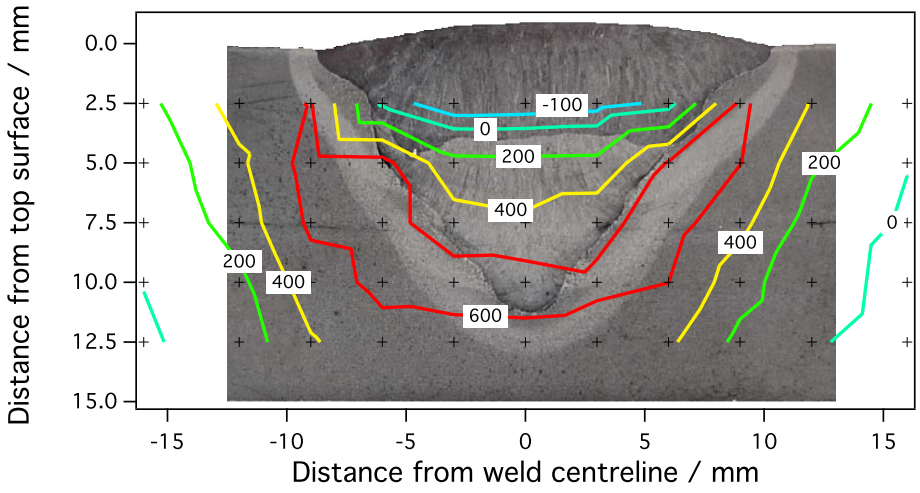

(a)

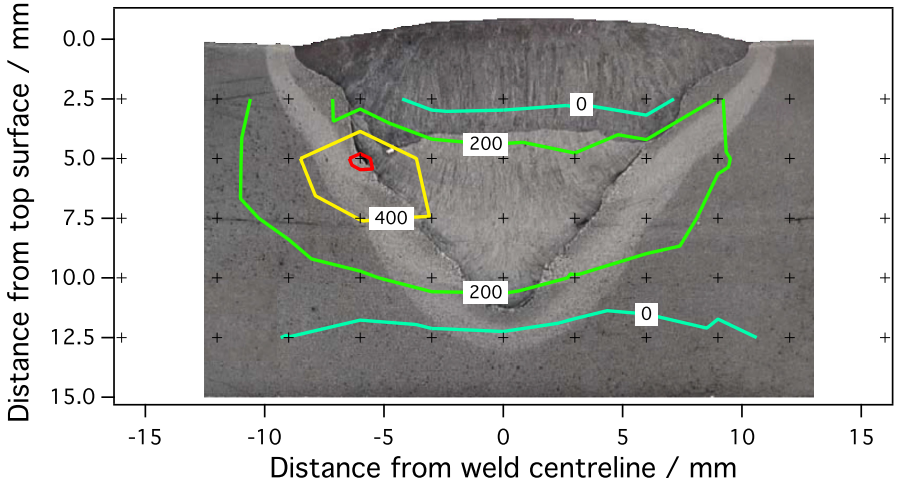

(b)

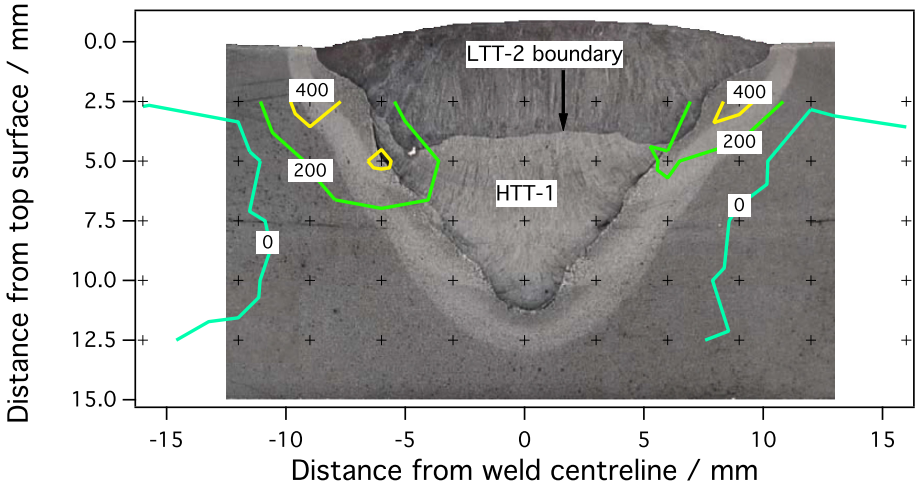

(c)

Figure 6.6: Residual stress contours for a standard, high M_s welding alloy with an LTT-2 capping pass (weld G), in MPa; (a) longitudinal, (b) transverse, (c) normal orientation.

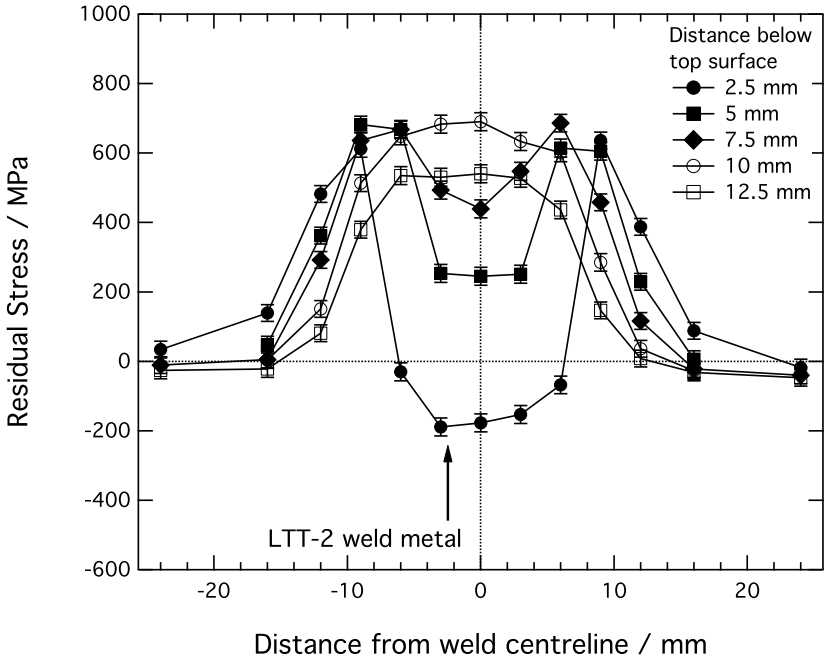

Figure 6.7: Longitudinal residual stress profiles as a function of distance from the weld centreline for a standard, high M_s welding alloy with an LTT-2 capping pass (weld G).

an inclusion would be averaged over a substantial quantity of material, thus compensating for the extreme strains recorded in a localised region. If the feature is large enough, it will effect the lattice strains apart from residual stress.

The stress contours in the normal direction of weld G are also unrepresentative of the other welds investigated in this work. There are expected low levels of stress throughout the bulk of the weld metal and base plate ($0 \rightarrow 200$ MPa) but then three points at 400 MPa. One of these measurements is at the identical position as for the 600 MPa transverse stress but the other two are situated such that they are mirrored about the weld centreline. This suggests that they are real values and that for the filler deposition sequence outlined, relatively large tensile stresses develop in HAZ towards the sample surface. The mechanism by which this phenomenon occurs is unclear and it should be replicated in weld A, which is essentially a single LTT layer deposited on a high M_S base. Although the weld G longitudinal stress distribution is substantiated by weld H, some of the points in the transverse and normal directions are seemingly anomalous and it may be necessary to repeat these measurements and verify their validity.

Referring to the longitudinal profiles, Fig. 6.3, the maximum tensile stress measured at the position nearest to the sample surface is the same for weld G and H. Although the final LTT-2 capping pass is capable of inducing compression in to the surface weld layer, it appears unable to influence the peak tensile stress in the adjacent HAZ/base plate. These peaks are not at identical locations with respect to the distance from the weld centreline because the weld widths differ slightly. This is a feature of arc welding and beyond the control of even the mechanised experimental conditions. Of interest is the level of compressive residual stress in the weld metal for weld G, compared with the other samples. Weld F (3–pass LTT-2) is less compressive because it cannot receive the full extent of stress alleviation through transformation plasticity. Weld C (3–pass LTT-1) has a M_S such that it transforms entirely to martensite. For weld G, the dilution of the LTT-2 alloy with the base material and underlying 'lean' HTT-1 filler leaves it a with a composition between weld F and C. The increase in M_S is sufficient to allow significant transformation induced strain and hence compressive stress.

Although the level of compression in the weld metal is slightly more enhanced for Weld G when compared with weld F, the latter appears to have a more favourable stress distribution based on smaller regions of high tensile stress further below the top surface. In fact, if minimising tensile stress in the region approaching the sample surface is the criteria for evaluating the effectiveness of a welding alloy/deposition sequence, then weld C and F are superior to weld H and G. It must be noted that the residual stress state at the actual surface is likely to deviate from the values measured in the bulk region during this investigation.

Despite the stress distribution and benefits to fatigue performance that are attainable with a single-pass, multipass welds produced with the highly alloyed LTT-2 may not be appropriate in service. This is due to the mechanical properties associated with high levels of retained austenite that cannot transform at such a low temperature in the almost undiluted surface layers of the weld deposit. There will be a decrease in strength in the dual-phase (austenite–martensite) weld metal but this will be combined with improved toughness.

Depending on the final composition and microstructure its behaviour may characterise that of a transformation-induced plasticity (TRIP) steel following welding [28]. This may prove effective in relieving local stress concentrations that arise during the fatigue process.

Additionally, results from the preceding chapter for the filler LTT-1 showed a further improvement of stress distribution when the $T_{\mathrm{I}} > M_{\mathrm{S}}$. Depending on the welding speed and number/geometry of passes, it is possible that the entire weld will subsequently transform simultaneously on cooling, thus realising the full benefits of transformation plasticity across the entire weld. The heavily suppressed M_{S} of LTT-2 would mean that a lower T_{I} is required to achieve this.

Hardness profiles along the weld centreline, Table 6.1, confirm the changes of microstructure with dilution of the LTT alloys. The mechanical properties of the undiluted fillers and base metals are in Table 3.2. Welds C, M, N were all welded with LTT-1 and have consistent readings with each other ($\sim 380\,\mathrm{HV}$). Weld F has significant levels of retained austenite in the passes nearer the surface and therefore a much lower hardness ($\sim 270\,\mathrm{HV}$), this increases with dilution in the initial pass at $> 7\,\mathrm{mm}$ below the surface ($\sim 390\,\mathrm{HV}$). Weld G, although having an LTT-2 surface pass, records a high hardness in this layer similar to LTT-1 ($\sim 390\,\mathrm{HV}$). This confirms the extent of dilution with the surrounding material. The hardness then drops significantly ($\sim 300\,\mathrm{HV}$) as data were collected from the lower strength underlying HTT-1 filler. Weld H comprised of thee HTT-1 passes and experienced minimal dilution with the base plate such that no significant change in hardness was detected throughout the individual layers ($\sim 280\,\mathrm{HV}$).

6.4 Base Plate Strength

In order to determine the versatility of the LTT alloys with regards to welding steel plates of varying strength, two base materials were selected that had yield strengths above (weld M, Fig. 6.8) and below (weld N, Fig. 6.9) that of the filler alloy. For weld C, the yield strength of the filler was comparable to the base plate, Table 3.2. Both welds develop compression in the weld metal

Table 6.1: Hardness profiles / HV10.

Position below surface/ mm	Weld C	Weld F	Weld G	Weld H	Weld M	Weld N
1	372	277	400	279	372	373
2	375	263	402	295	372	378
3	376	261	395	288	377	377
4	379	273	391	283	367	375
5	376	292	304	283	387	383
6	384	296	319	290	390	395
7	375	406	315	301	392	400
8	393	394	285	317	400	411
9	366	374	273	266	368	385
10	382	397	278	278	389	387

and peak tensile stresses in the vicinity of the HAZ that correlate with the yield strength of the associated base plate. The maximum residual stresses for weld M are > 800 MPa, Fig. 6.10, but these were recorded at depths of 5–7.5 mm below the surface, away from the weld toe. The 600 MPa contours encapsulate the HAZ in the regions adjacent to and below the weld metal, which displays compressive stresses > -400 MPa. Lower levels of compression are evident in the weld metal in both the transverse (-200 MPa) and normal (-100 MPa) directions. However, these same values of stress are found in the base plate for each orientation. The peak tensile stresses are 200 MPa (transverse) and 300 MPa (normal), and are located in the HAZ.

The maximum tensile stress generated in the HAZ of weld N, Fig. 6.11, is significantly lower (400–500 MPa) compared with weld M. This would suggest that the thermal stresses generated in the constrained weld metal and surrounding base plate approach or exceed the yield strengths of the respective materials. There will to be some adjustment to the microstructure in the HAZ that will change the original properties of the pre-welded base plates and effect the residual stresses that can be sustained. The martensitic transformation in the LTT weld metal is sufficient to negate the tensile stresses that develop in regions of the fusion zone. However, the accumulated tensile stresses in the base plate remain, although expansion of the weld metal will inevitably lead to some alleviation and re-distribution.

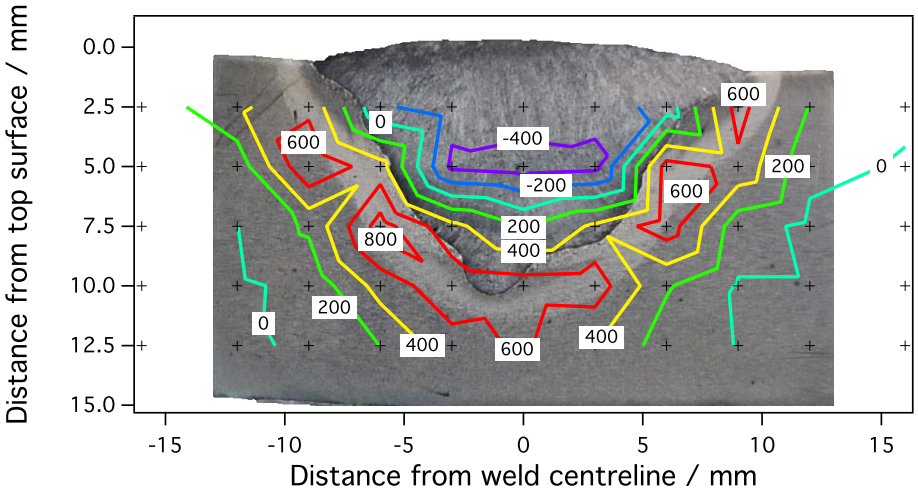

(a)

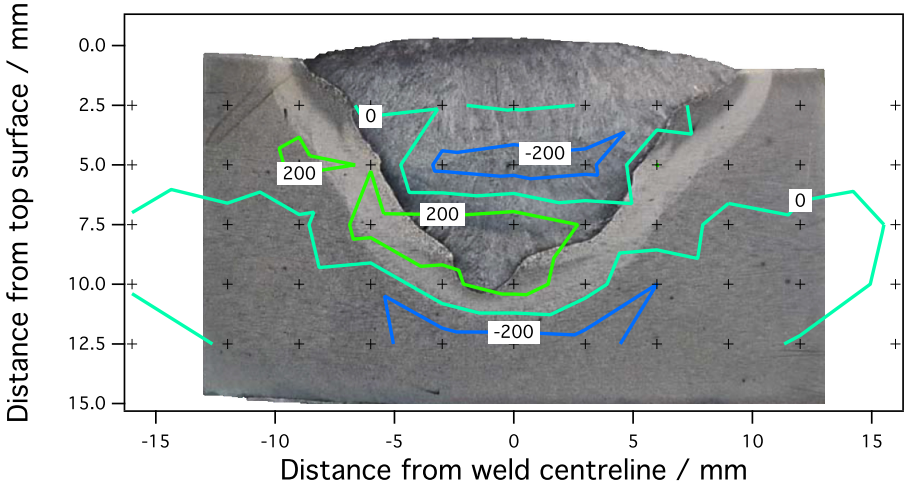

(b)

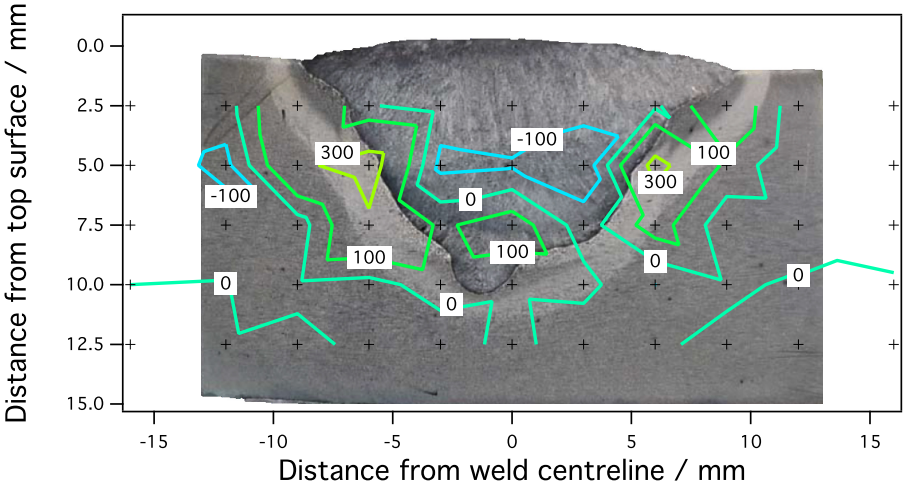

(c)

Figure 6.8: Residual stress contours for a low M_s welding alloy deposited on a high strength base plate (weld M), in MPa; (a) longitudinal, (b) transverse, (c) normal orientation.

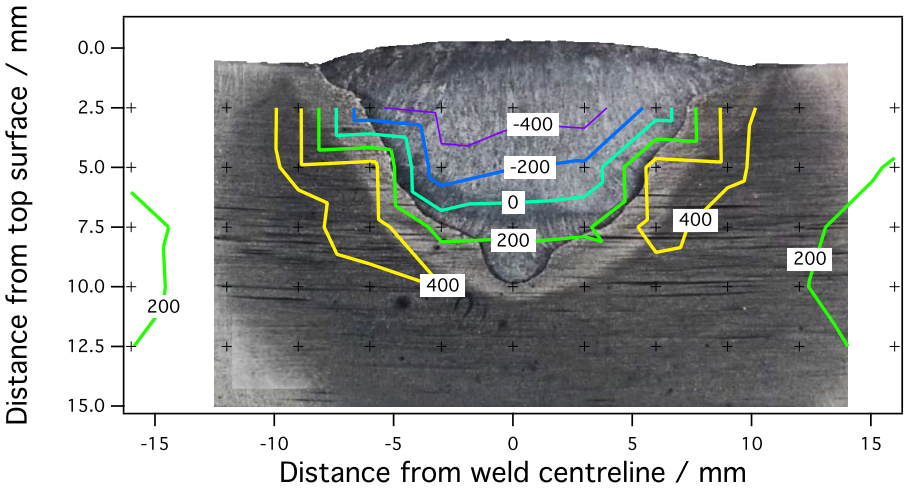

(a)

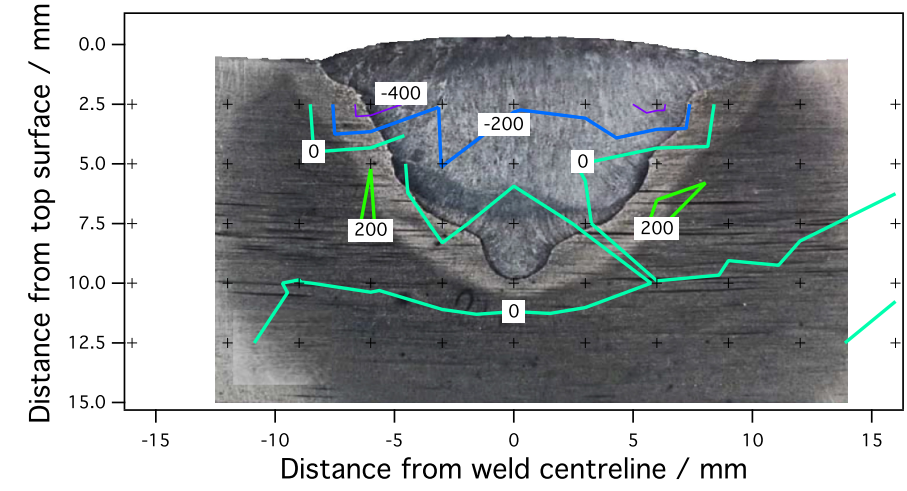

(b)

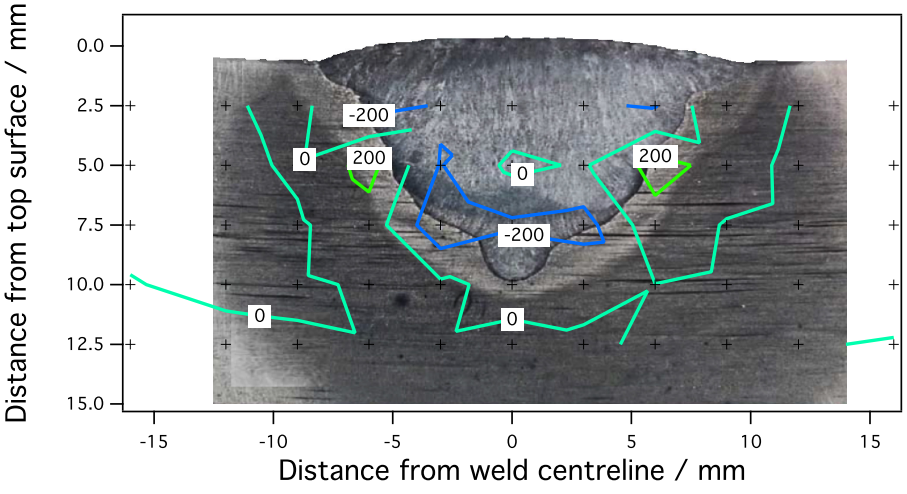

(c)

Figure 6.9: Residual stress contours for a low M_s welding alloy deposited on a low strength base plate (weld N), in MPa; (a) longitudinal, (b) transverse, (c) normal orientation.

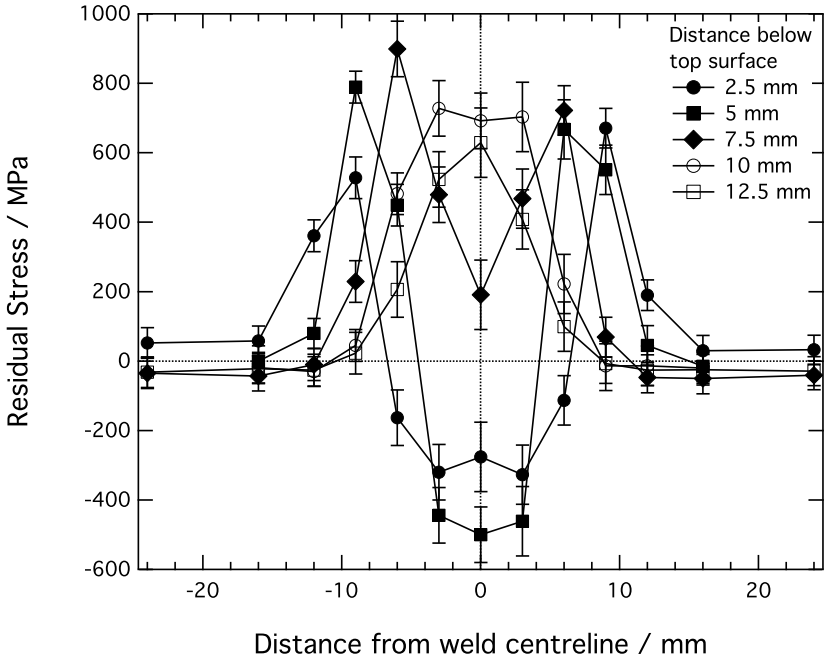

Figure 6.10: Longitudinal residual stress profiles as a function of distance from the weld centreline for a low M_s welding alloy deposited on a high strength base plate (weld M).

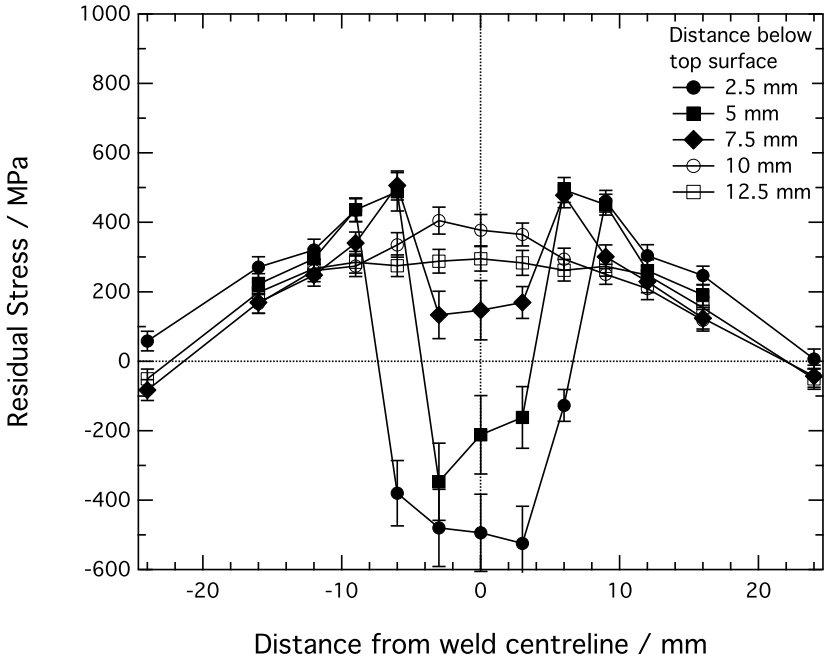

Figure 6.11: Longitudinal residual stress profiles as a function of distance from the weld centreline for a low M_s welding alloy deposited on a low strength base plate (weld N).

The contours in all three orientations show compression in the weld metal, for a few locations this stress state traverses the fusion boundary into the HAZ. This is not as pronounced for the higher strength base plates and may be caused by the expanding weld metal plastically deforming the relatively weak surrounding material, thus forcing it into a state of compression. To verify this theory, it would be necessary to use a smaller gauge volume and increase the number of measurement points at the specific sites of interest. Inducing a compressive stress at the weld toe may be possible when joining low strength material, which would improve fatigue performance.

6.5 Strain Measurement Positions

As a result of the time limitations associated with strain scanning using neutron diffraction, a compromise usually exists between the number of measurement points and the number of specimens that can be analysed. Additional strain data were taken for weld M, Fig. 6.12. This was to ensure that the initial concentration of measurement positions was sufficiently adequate to capture the stress profiles across regions of abrupt change, such as the fusion boundary and HAZ. For the collection of welds in this work, readings were taken every 3 mm, signified by the solid markers. Extra locations have been included (open markers) to show the change in profile that occurs when the number of measurement positions is increased to every 1 mm. The original distribution of points provides a satisfactory representation of the stress changes that occur for the scope of this work, but they do not capture the exact locations of the inflections and the maximum/minimum values, which can deviate over 100 MPa from those initially measured.

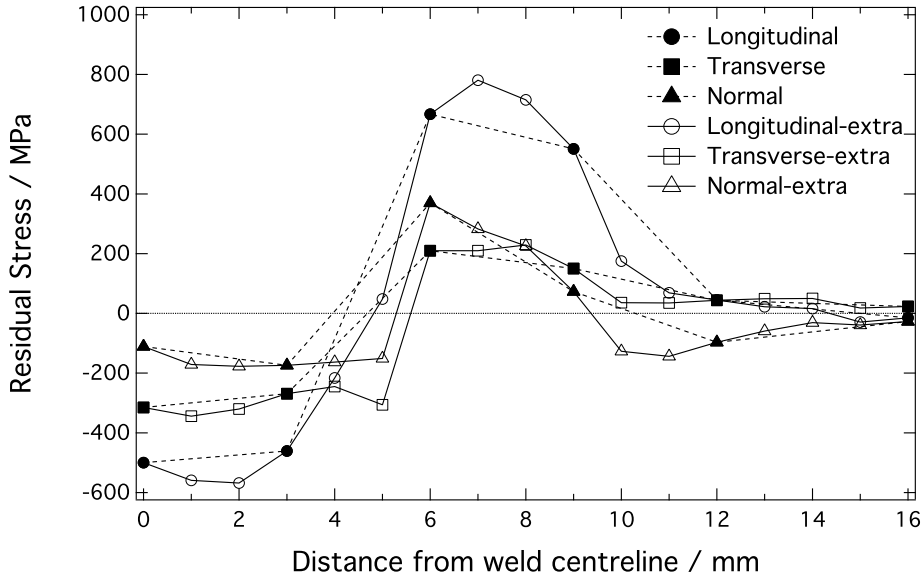

Figure 6.12: Weld M; longitudinal, transverse and normal residual stress profiles as a function of distance from the weld centreline highlighting the change in profile with additional strain measurement positions at 5 mm below the surface.

6.6 Conclusions

Neutron diffraction has been employed to measure the triaxial strain evolution for a series of arc welded plates, fabricated with two martensitic fillers which transform at a low temperature. The stresses inferred were used to create contour maps that identify the effects of dilution and base plate strength with a view to optimising the welding process for enhanced fatigue performance.

There is no additional benefit to stress relief by using a highly enriched welding filler (LTT-2) to compensate for compositional dilution with the base plate for a multipass weld. This is due to an overly suppressed M_S such that the martensitic reaction is incomplete and the effects of transformation plasticity cannot be fully exploited at ambient temperature in the final passes.

The use of a highly enriched welding filler (LTT-2) as a final capping pass, successfully imparts minor compression into the surface regions of the deposited weld metal. Large areas of tensile residual stress remain in the surrounding HAZ, akin to the contours displayed by the 3–pass, high M_S welding alloy.

Weld C displayed the optimum stress distribution in terms of the relative size and positions of the maximum tensile stress generated; considering the yield strength of the base plate. Weld F produced a comparable stress distribution but the retained austenite in the final deposits will reduce the strength of the weld metal in this region. This would be beneficial if a particularly tough and ductile weld was preferred, it may also enhance fatigue performance through its TRIP properties relieving local stress concentrations in service.

If more uniform mechanical properties were desired throughout the mulitpass weld deposit, the appropriate procedure may be to begin welding with the highly enriched (LTT-2) alloy followed by deposition of the lower alloying content filler (LTT-1). This sequence would also have the effect of permitting the majority of the austenite to transform into martensite at the point where the weld metal reaches ambient temperature and theoretically maximise the stress-relief benefits of transformation plasticity.

Two base plates were selected that had a yield strength above and below that of the LTT-1 filler alloy. Both welds developed compression in the weld metal and peak tensile stresses in the vicinity of the HAZ that correlated with the yield strength of the associated base material.

For all welded specimens, the re-austenised material surrounding the fusion boundary will transform to martensite at a temperature governed by the base plate. This will lead to the accumulation of tensile stress in these regions due to the elevated M_S. The use of a low strength base material may negate these thermal stresses further because the expanding LTT filler induces compression through plastic deformation into the adjacent plate as shown by weld N.

Additional diffraction data indicate that measurement positions every $\sim 1\,\text{mm}$ are necessary to accurately capture the locations of inflection and the maximum/minimum stresses across the fusion boundary and HAZ. For the purposes of stress characterisation in the material bulk, measurements recorded at 3 mm intervals proved satisfactory and were able to identify the changes associated with different welding conditions.

Chapter 7

Surface Residual Stresses

7.1 Introduction

The welded joints of engineering structures are known to limit the service loads that can be applied and their fatigue tolerance. Tensile residual stresses at the surface compromise fatigue resistance through the accelerated initiation of microcracks, especially at the boundary between the weld metal and base material. This is caused by geometrical changes leading to stress concentrations, coupled with local microstructural variability, and increases the susceptibility to microcrack initiation/propagation. In order to increase the longevity of welded components, post-weld treatments may be applied that are either mechanical or thermal in nature. Heat treatments are able to relax internal stresses while mechanical processes tend to impart compression into the component surface or modify the weld toe geometry to reduce stress concentration.

Investigations in the preceding chapters have identified the generation of compression in the weld metal for the LTT fillers. It is these compressive residual stresses that are accepted as responsible for enhanced fatigue performance. However, the exact mechanism by which they achieve this has not been fully verified. Neutron diffraction results from the material bulk show tensile residual stresses approximating the base plate yield strength in the adjacent HAZ, at locations tending towards the specimen surface. The predominant site for fatigue failure is the weld toe and the tensile stresses at this discontinuity may not be alleviated through transformation plasticity.

Fig. 7.1a shows the weld deposit in compression, the adjoining base metal in tension and the fusion boundary at a stress level between the two extremes. The contours have been restricted to a depth of 2.5 mm below the surface but the weld line registers a value of 0 MPa at this position. Referring to Fig. 5.2a, identical positions for weld H are in tension, ~ 400 MPa. The transformation temperature determines the stress state in the weld metal but also, clearly influences the value at the weld/base plate interface. Fig. 7.1b illustrates the opposing forces across the fusion boundary following martensitic reaction.

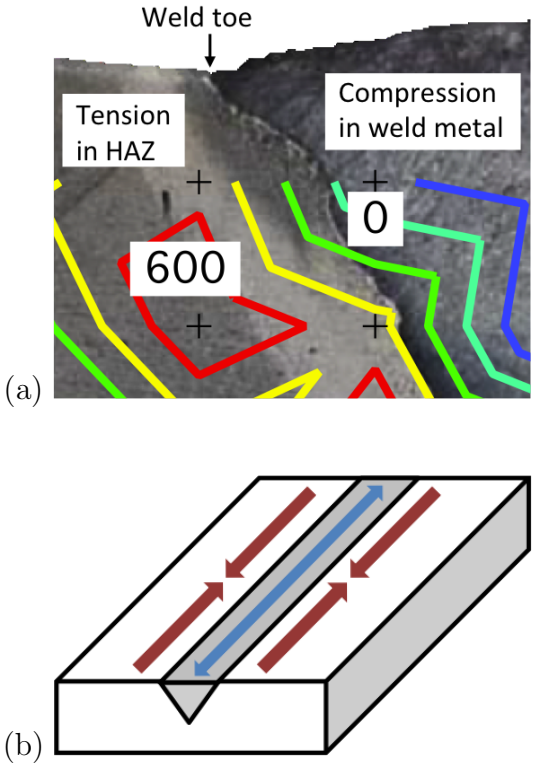

Figure 7.1: Longitudinal residual stress accumulation in a welded plate following transformation of a low M_S filler; (a) enlarged region of the fusion boundary at the surface with stress contours (weld M), (b) transformation expansion of the weld metal and thermal contraction of the base plate.

Compression at the weld toe, or even a reduction in tensile stress, would explain the reported improvements in fatigue performance but the bulk neutron diffraction data cannot be allowed to extrapolate to the surface due to possible steep stress gradients. Stresses inferred from synchrotron X-ray data are seemingly in contradiction with measurements made in the bulk, as they reveal tension in the weld metal surface [19, 20]. In this work, near-surface neutron

diffraction has been performed at the Canadian Neutron Beam Centre (CNBC) and used to probe the residual stress state in the vicinity of the free surface in order to rationalise the apparent disparity.

7.2 X-Ray Diffraction

Residual stresses, inferred from X-ray data using the $\sin^2\psi$ method, for the longitudinal and transverse orientations are presented in Figs 7.2–7.5. The full complement of 13 welded plates, Fig. 3.3, were analysed and the respective fusion boundaries have been added to the surface stress profiles. The errors fall within $\sim \pm 50$ MPa but there were other uncertainties in some of the results recorded and they have been omitted, hence a discontinuous profile. The weld microstructure contains regions of large grains and solidification texture, which contribute to difficulties in producing a reliable stress value at these positions [32]. Although the welding conditions specific to each specimen will influence the residual stress, there are some general trends that appear to be common to the LTT fillers.

With respect to the transverse orientation, welds produced with the LTT alloys show mild compression in the base plate in the range of $\sim -200 \rightarrow 0$ MPa. There is a sharp transition from compression to tension in the vicinity of the fusion boundary that leads to high tensile stress in the weld metal. These are the order of $\sim 600 \rightarrow 800$ MPa but there are peak values recorded up to 900 MPa. The only exception to this trend is weld C, Fig. 7.2c, which also displays a small magnitude of compression in the base plate but records a much lower level of tensile stress in the weld deposit (~ 200 MPa). This could be an anomaly, the data do not fit particularly well with the other results and further readings may be necessary to establish their authenticity. The longitudinal stress profiles of the LTT welds are flatter, compared with the transverse orientation. They have lower peak tensile stresses (< 400 MPa), which occur in the HAZ, and are < 200 MPa in the weld metal. Weld C displays lower than average peak tensile stress at the base plate/filler interface (~ 100 MPa) and the entire weld deposit is in compression.

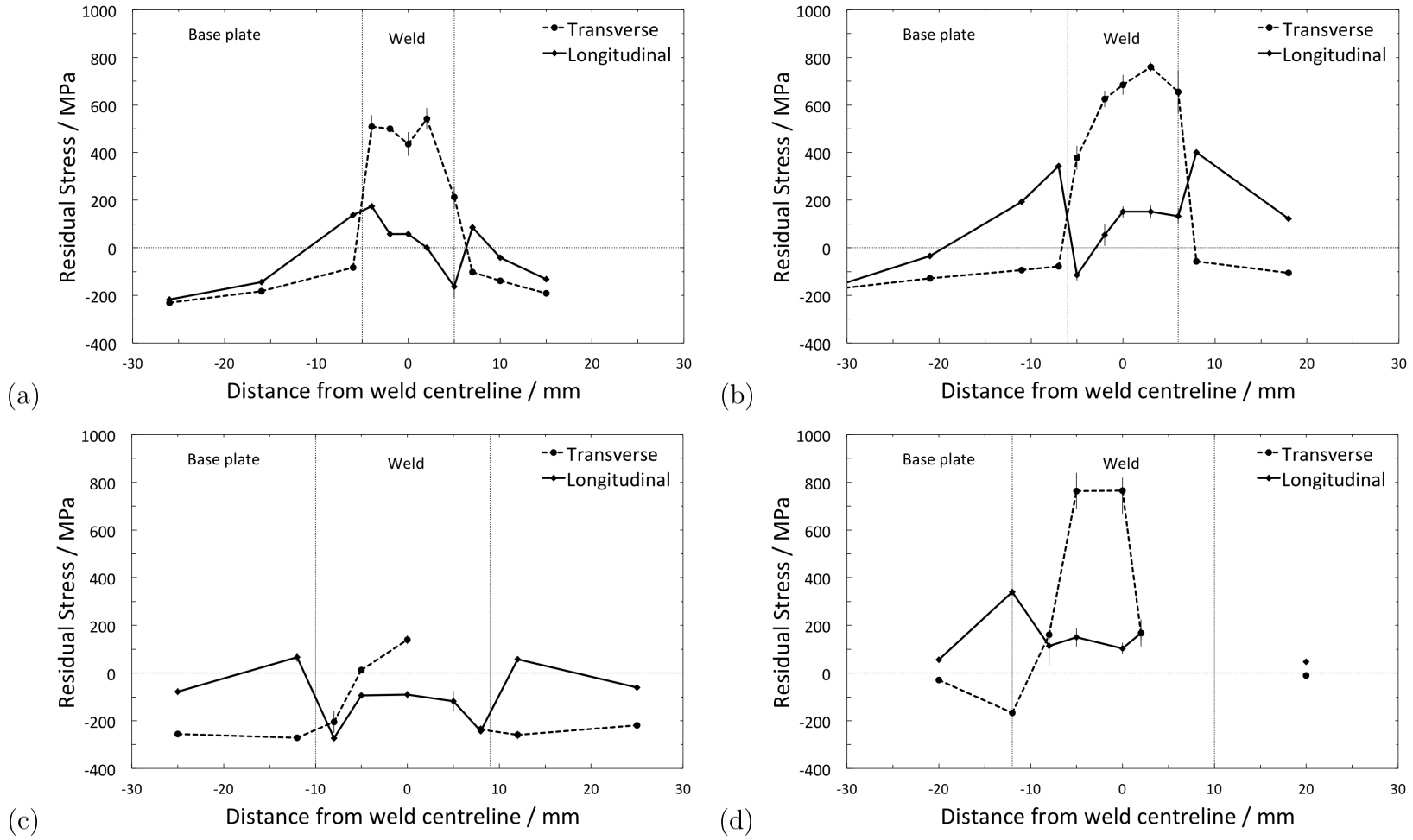

Figure 7.2: Surface X-ray residual stress profiles; (a) weld A, (b) weld B, (c) weld C, (d) weld D.

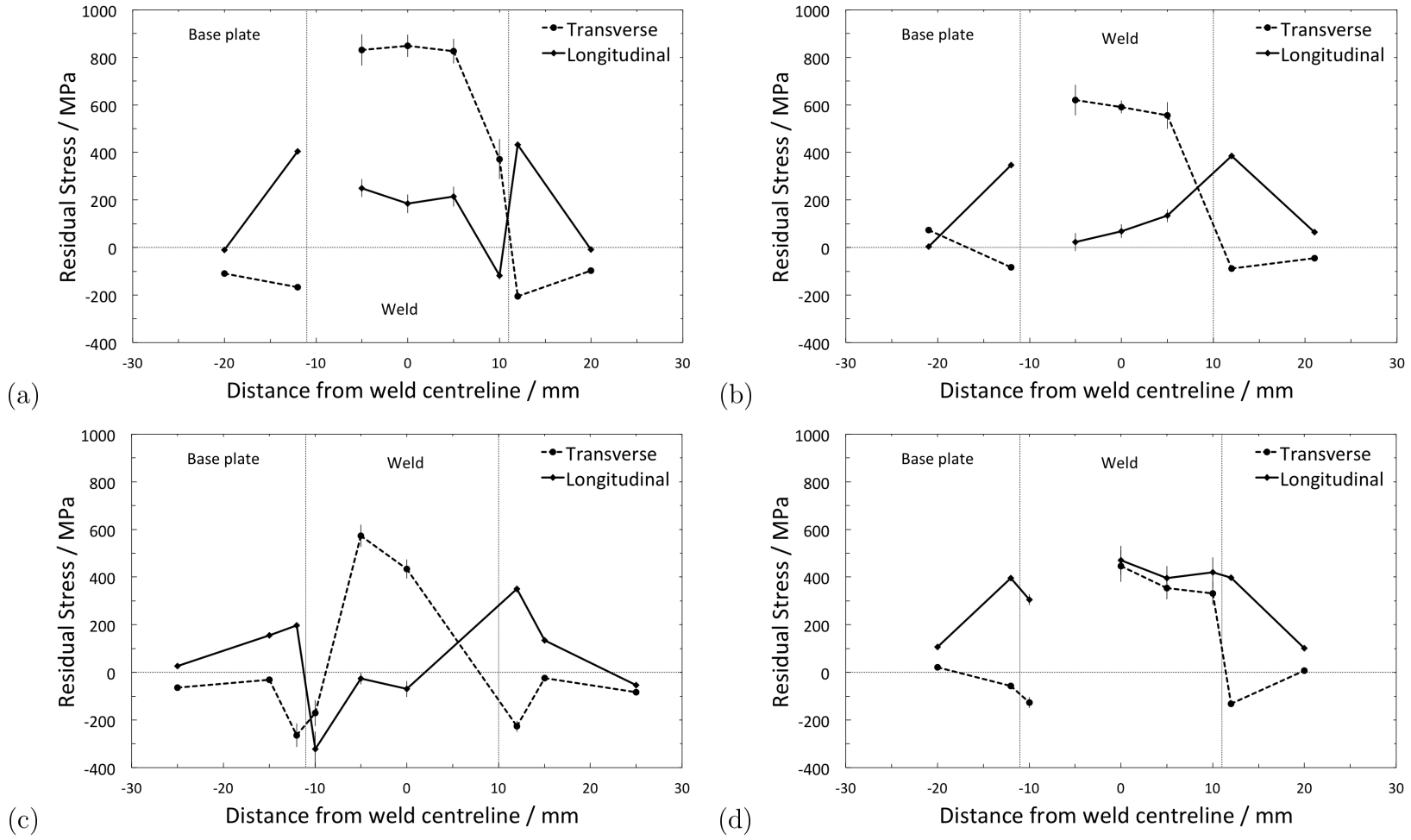

Figure 7.3: Surface X-ray residual stress profiles; (a) weld E, (b) weld F, (c) weld G, (d) weld H.

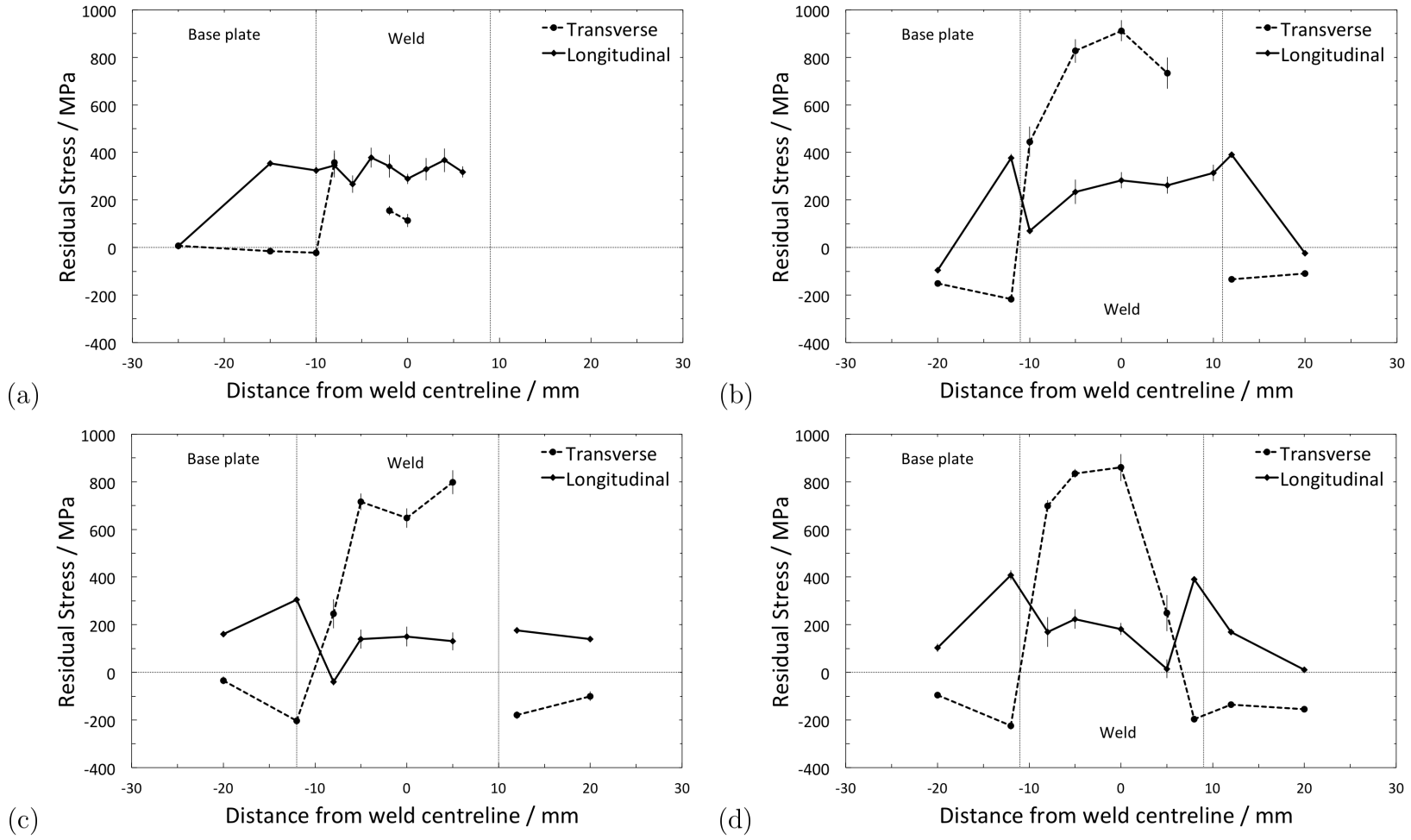

Figure 7.4: Surface X-ray residual stress profiles; (a) weld J, (b) weld K, (c) weld L, (d) weld M.

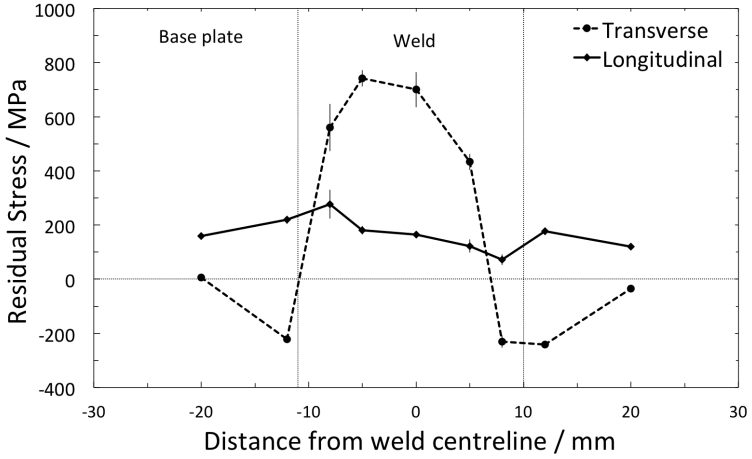

Figure 7.5: Surface X-ray residual stress profiles; weld N.

Welds H, Fig. 7.3d, and J, Fig. 7.4a, were made with high M_S fillers. The peak tensile transverse stresses are located in the weld metal but are half of the value ($\sim$ 400 MPa) found in the LTT fillers. The maximum longitudinal stress is also around 400 MPa and this level remains constant across the weld deposit, unlike the LTT welds that showed a moderate reduction when passing through this region. The stress profiles across the base material are almost identical to the LTT welds.

The surface X-ray profiles are distinct when compared with the neutron diffraction data measured at 2.5 mm depth (chapters 5 & 6). The gauge volume at 2.5 mm will extend into the surface regions to a depth of $\sim$1 mm, Fig. 4.10, but it is evident that the bulk and surface stresses are inherently different, Fig. 7.6a. The maximum tensile stress (transverse direction) is measured in the weld deposit at the surface, and in the adjacent base plate (longitudinal direction) at 2.5 mm depth. Equally significant is the transition from longitudinal compression to tension, in the low M_S weld metal, that occurs between the two different measurement depths. Weld H, Fig. 7.6b, shows similar disagreements between the stress profiles with varying depth but not to the same extent as weld M. The M_S of the welding alloy affects the residual stress distribution both at the surface and in the material bulk.

The surface stress data are unexpected, especially the presence of tension in the weld metal, but it has precedence in the work completed by Kromm *et al.* [19].

(a)

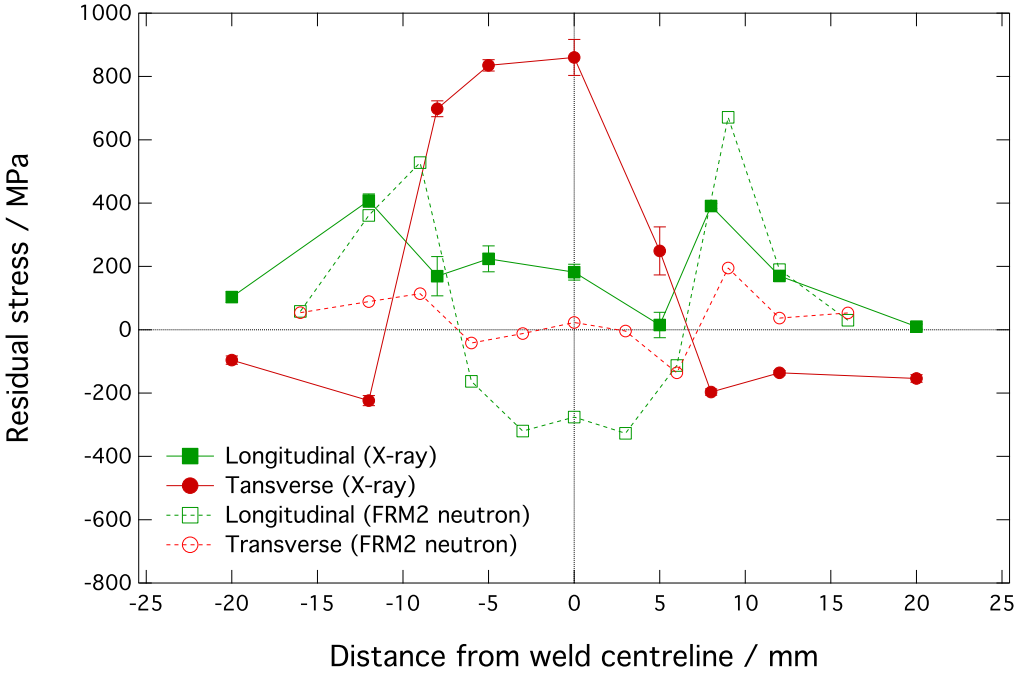

(b)

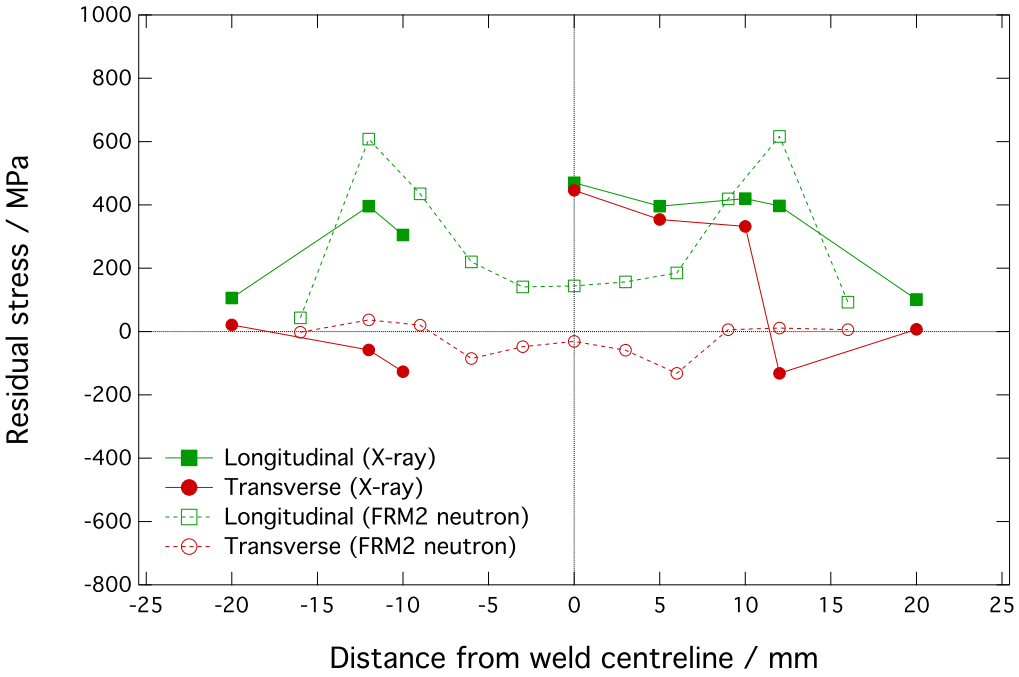

Figure 7.6: Residual stress profiles for the longitudinal and transverse orientations measured using X-rays and neutrons; (a) weld M, (b) weld H.

They used high-energy synchrotron X-rays to measure the surface strains in a multipass butt weld, welded with a 10Cr–10Ni wt% alloy, Table 2.4. The M_S of the undiluted filler was 90 °C and the other welding conditions were comparable to those adopted for weld F. The longitudinal and transverse stress profiles of weld F have been overlaid on those recorded using the 10Cr–10Ni wt% alloy, Fig. 7.7. Overlooking the differences in weld width, there is agreement between the stresses. This may be improved by increasing the number of measurement points for weld F but the key factor in correlating the two data sets are the stress values in the weld metal, which are essentially equal in magnitude. Weld F was selected as the most appropriate comparison because of its higher nickel content and more equivalent M_S, *cf.* the LTT-1 alloy.

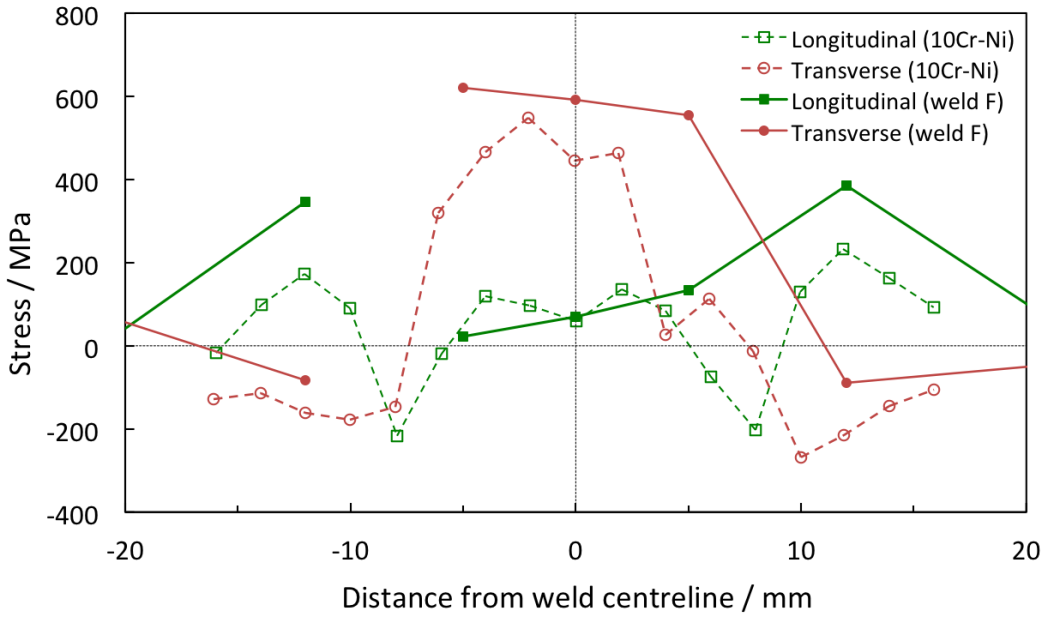

Figure 7.7: X-ray determined residual stress profiles for the longitudinal and transverse directions of two welds, welded with similar M_S fillers [19].

7.3 Neutron Diffraction

X-ray results from this work, and the literature, provide overwhelming evidence for the existence of large tensile residual stresses in the surface regions of the low M_S weld deposit. Due to the apparent disparity with the bulk data

it was deemed necessary to confirm the findings with neutron measurements taken from the near-surface region. X-ray derived stresses for welded specimens are prone to errors through large grain size, texture and uneven surfaces. Neutron diffraction applies a larger sampling volume that is below the surface and through these factors can provide more reliable information. Three welds were selected for near-surface assessment, Table 7.1.

Table 7.1: Welds selected for near-surface stress evaluation.

Weld	Base Plate	Pass 1	Pass 2	Pass 3
C	BP700	LTT-1	LTT-1	LTT-1
G	BP700	HTT-1	HTT-1	LTT-2
H	BP700	HTT-1	HTT-1	HTT-1

Weld C had unusually low peak surface stresses in the weld deposit, which the neutron technique might confirm. Weld H was joined with a high M_S filler and was used as a benchmark. Weld G was analysed to determine whether a single capping pass would be sufficient to provide the same surface stress distribution as a full low M_S weld. Measurements were made at 0.15 mm below the top surface in the weld, heat-affected zone (HAZ) and base plate to ascertain how the stresses vary across both sides of the weld. The gauge volume selected was deemed to be the smallest possible that was capable of producing defined diffraction peaks. The centroid of the gauge volume could therefore be positioned at 0.15 mm below the surface, whilst simultaneously avoiding partial-immersion errors. Thus, the near-surface stress results were volume averaged over 0–0.3 mm below the surface. Further measurements were made at 2.5 mm depth to allow comparison with data collected at other neutron sources using larger gauge volumes. Macrographs of the three welds, Fig. 7.8, reveal the layer structure. The boundary between passes is pronounced when the LTT-2 filler is deposited on top of HTT-1.

7.3.1 Near-Surface Stress

In order to achieve positional accuracy, the change in full width at half maximum (FWHM) across the fusion boundary at the plate surface was analysed

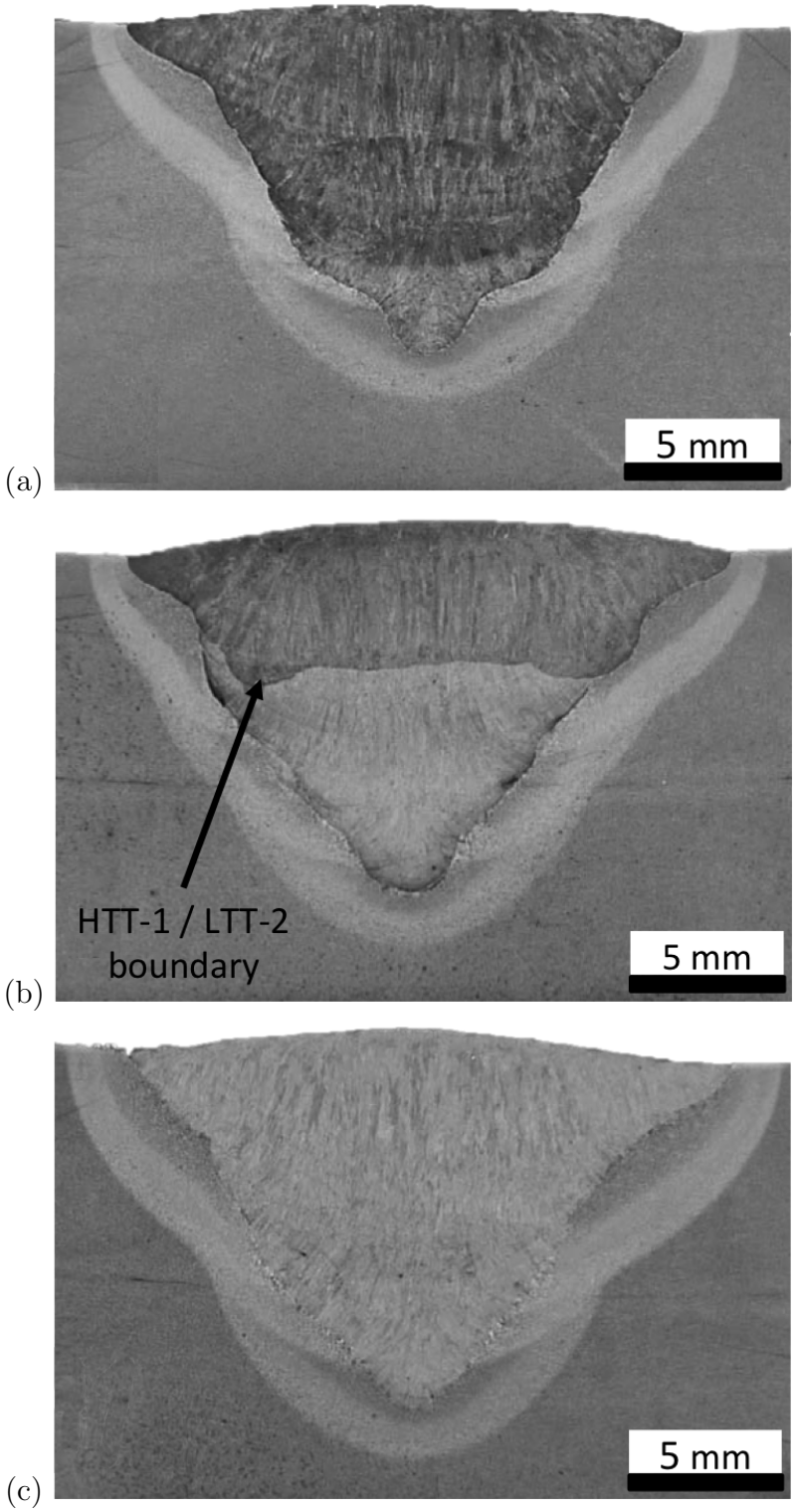

Figure 7.8: Macrostructures of (a) weld C, (b) weld G, (c) weld H.

in 0.25 mm increments. The diffraction peak altered significantly when the gauge volume was totally immersed in the weld metal compared with the base plate and this effect was used to ascertain the fusion boundary positions at the surface. The strain-free reference specimens, previously employed for the bulk stress analysis, were re-measured and used to account for the effect of compositional variation between the filler alloy and base plate. The surface residual stresses measured in three orientations by neutron diffraction are presented in Figs 7.9–7.10. Larger experimental uncertainties are registered in the weld metal than the base plate for all three specimens, which may be attributed to solidification texture. However, trends are evident and symmetry along the centreline would suggest that the data are reliable.

The profile for weld C, Fig. 7.9a, shows high tensile longitudinal stresses in the HAZ with compression in the weld metal, which is characteristic of these types of LTT alloys. Conversely, the transverse stresses are tensile in nature in the weld metal and mildly compressive in the HAZ. The normal stresses are compressive in the weld metal and given their proximity to a free-surface they may be expected to be closer to zero, however, it is possible for stress to be retained within a few hundred micrometres of material. The weld H filler, Fig. 7.9b, has a sufficiently high M_S that the benefits of transformation plasticity are eradicated on further cooling to ambient temperature and this is reflected by the tensile longitudinal stress in the weld metal. As with weld C, high tensile longitudinal stresses exist within the HAZ. The transverse stress is tensile in the weld metal and does not display the sharp change to a compressive stress at the fusion boundary, which is evident for weld C. Weld G, Fig. 7.10, displays a stress profile more akin to weld C. The longitudinal stress is compressive in the weld metal with high tensile stresses in the HAZ. Continuing the trend of the previous two specimens, tensile transverse stresses are found in the weld metal.

The transverse stress measured at the critical location of the weld toe differs significantly between weld C ($\sim$-600 MPa) and weld H ($\sim$-200 MPa). Also, the compressive region for weld C extends further into the base plate and weld metal. The filler M_S clearly influences the transverse residual stress distribution but tension remains in the central portion of the weld metal. This is not the case for the stresses measured in the longitudinal orientation. A possible

(a)

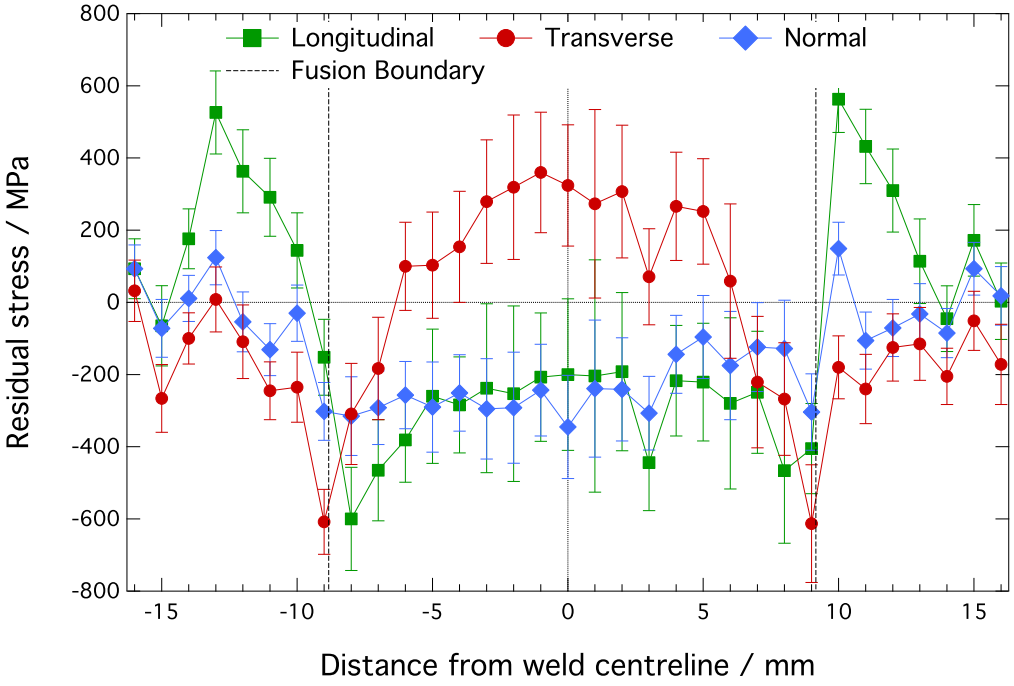

(b)

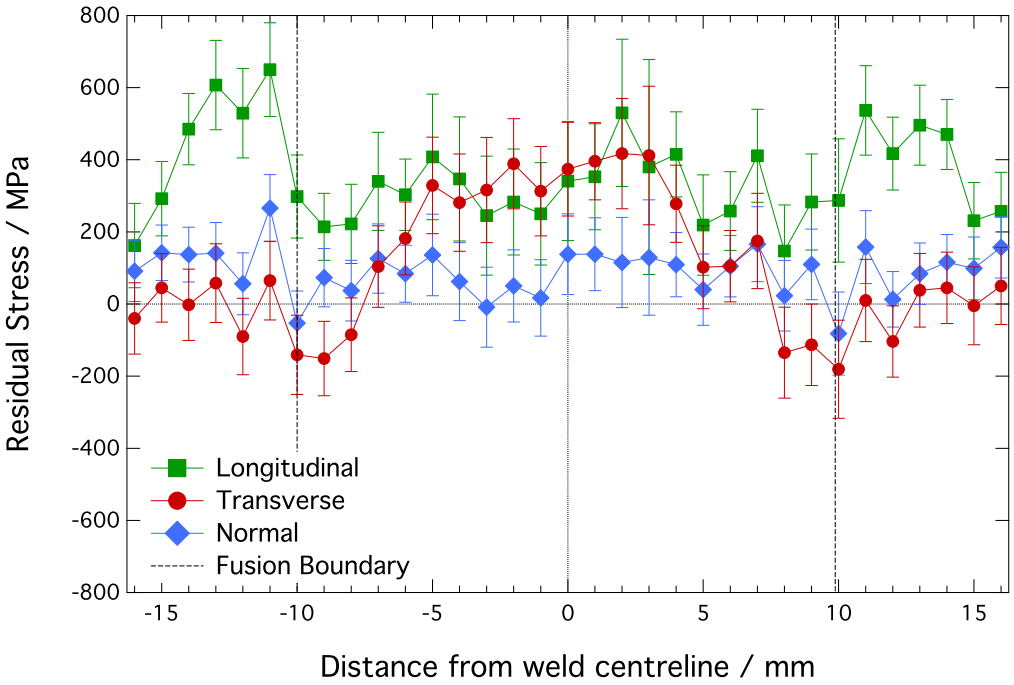

Figure 7.9: Longitudinal, transverse and normal near-surface residual stress profiles recorded at a depth of 0.15 mm by neutron diffraction; (a) weld C, (b) weld H.

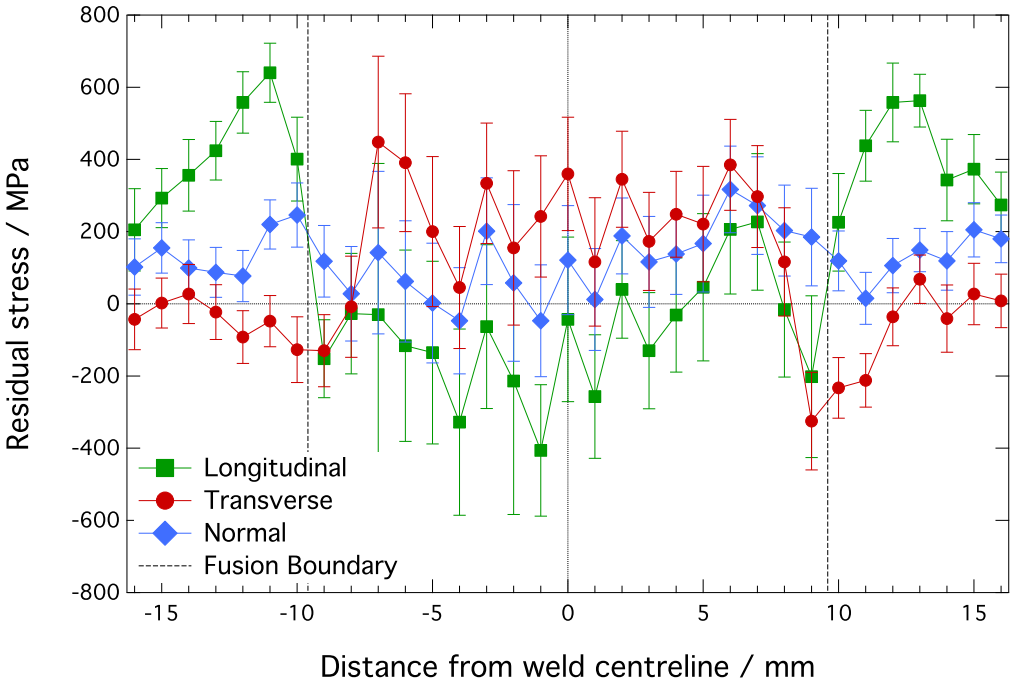

Figure 7.10: Longitudinal, transverse and normal near-surface residual stress profiles recorded at a depth of 0.15 mm by neutron diffraction; weld G.

explanation for this behaviour is that the longitudinally generated stresses are greatest because this is the direction of maximum thermal constraint during cooling. External stresses are known to initiate variant selection during the early stages of the $\gamma \rightarrow \alpha'$ transformation [138]. It is, therefore, presumed that the martensitic variants initially orient themselves in order to cancel the dominant longitudinal stresses. However, as the transformation continues, subsequent variants are less free to align themselves in such a manner as to minimise the tensile stresses in the transverse orientation. This hypothesis may be confirmed by detailed microstructural analysis. The residual stresses at the fusion boundary for weld C show compression in all orientations. In contrast, the longitudinal stresses in weld H are tensile in nature. The maximum tensile stresses at the fusion boundary for weld G are less tensile compared with weld H, which would suggest that there are benefits to applying an LTT capping pass in multipass welds but not to the extent of a full, multi-layer LTT weld.

7.3.2 Bulk Stress

The small gauge volume required to measure the near-surface stresses has the effect of deceasing the quantity of material sampled. This reduces the number of suitably oriented grains that can satisfy Bragg's Law and contribute to the diffraction pattern. To verify that by using such a small sampling volume there would be no detriment to the measured strains, the triaxial stress state was assessed at 2.5 mm below the surface and compared with previously collected data, Fig. 7.11. The reduction in sampling volume between the experiments conducted originally at ISIS (weld C) and FRM2 (weld H) is substantial. The change in dimensions, for the longitudinal measurement, from $3 \times 3 \times 3$ mm (weld C) and $2 \times 2 \times 2$ mm (weld H) to $0.3 \times 0.3 \times 3$ mm at the CNBC leads to a significant curtailment of irradiated material. This equates to a decrease in gauge volume of $\times 100$ for weld C and $\times 30$ for weld H, chapter 3. However, the trends identified for both sets of data for the two welded plates are comparable, the only minor exception being the stresses recorded in the weld metal.

For weld C, Fig. 7.11a, all three measurement orientations show slightly lower stress values when the small gauge volume is adopted. In most instances, the difference is less than 200 MPa but there are a few exceptions in the longitudinal direction where the discrepancy is twice this value. This is not necessarily a contradiction because the larger gauge volume will average the strains measured at a depth of $2.5\,\text{mm} \pm 1.5\,\text{mm}$, whilst the small gauge volume range is only $2.5\,\text{mm} \pm 0.15\,\text{mm}$. This could have a significant effect, depending on the stress gradients in this region. Error bars have been included for the longitudinal orientation and are representative of all orientations for the small gauge volume. Error bars are encompassed within the marker for the large gauge volume measurements.

The longitudinal, transverse and normal stress profiles for weld H, Fig. 7.11b, are in excellent agreement for the two different sampling volumes. This is the case for data recorded in both the base plate and the welding alloy. Greater disparity is registered in the weld metal for weld C, which is alloyed and effects the diffraction peaks more than the relatively lean base plate. The quantity of alloying additions in the HTT-1 filler (weld H) are much lower by comparison

(a)

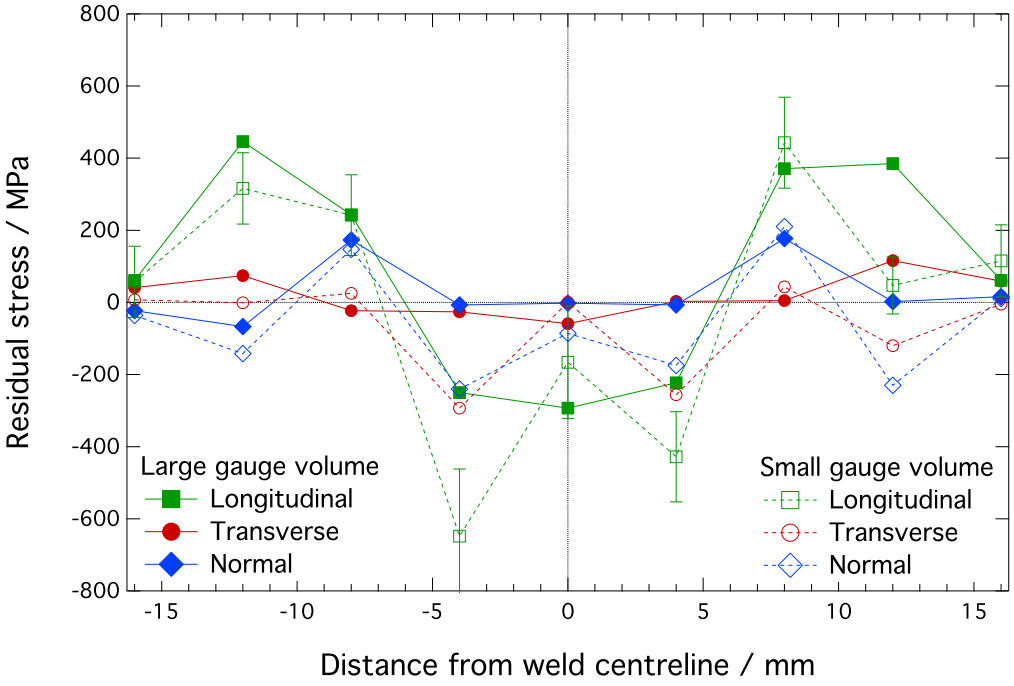

(b)

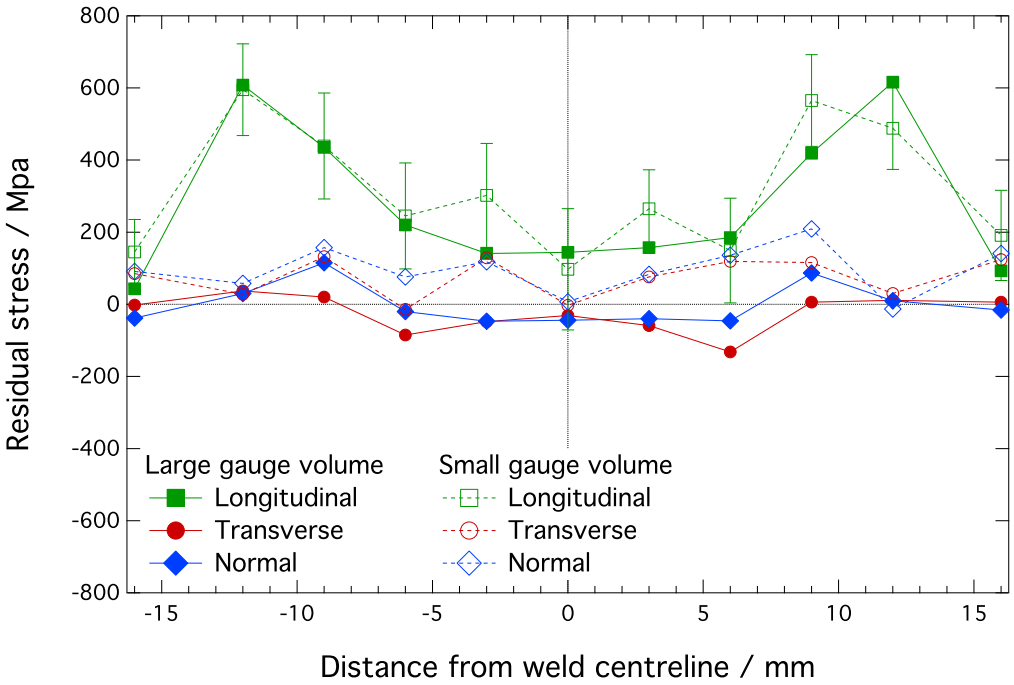

Figure 7.11: Residual stresses measured using neutrons at a depth of 2.5 mm below the sample surface. Measurements using a large gauge volume (solid lines) and small gauge volume (dashed lines); (a) weld C, (b) weld H.

and produce sharper, well defined peaks. The closeness in stress profiles may also be attributed to the smaller gauge volume used initially for the FRM2 bulk measurements, thus leading to a more comparable spatial resolution.

7.3.3 A comparison with X-rays

Longitudinal and transverse stress profiles derived from X-rays using the $\sin^2\psi$ method are presented along with near-surface measurements made with neutrons, Fig. 7.12–7.13. The error bars from the neutron data have not been included for clarity but can be referred to in Fig. 7.9. Whilst it is useful to compare both the X-ray and neutron data and anticipate similarities, it should be noted that measurements were made with different sampling volumes and at slightly different depths below the surface. The stresses measured by X-rays and neutrons are in agreement and the most significant observation is that all of the results derived, irrespective of technique, display large tensile transverse stresses in the weld metal.

The X-ray data for weld C were initially considered to be inconsistent with the results from all of the other welds. The near-surface neutron measurements would in some part agree with this theory, Fig. 7.12a. The higher tensile stress registered in the weld metal, by neutron diffraction, was expected but remains lower than the general trend supported by the additional specimens using X-rays. The peak longitudinal stresses are found in the HAZ. This is the case for both methods but the neutron results indicate greater tensile stress in this region, the order of 200–300 MPa. The number of measurement points is limited for the X-ray profiles, but if the technique is unable to detect peak tensile stresses of this magnitude then it may not be an appropriate procedure for this type of analysis. However, the discrepancy could be due to differing experimental conditions. Additional readings may improve the profile fits and provide a clear indication of the stresses at the weld toe. However, even with the limited data provided, compression is evident at his location in both orientations and coincides with the neutron results.

The stress profiles generated by the two diffraction modes for weld H, Fig. 7.12b, are consistent and indicate that there are no significant changes between the

(a)

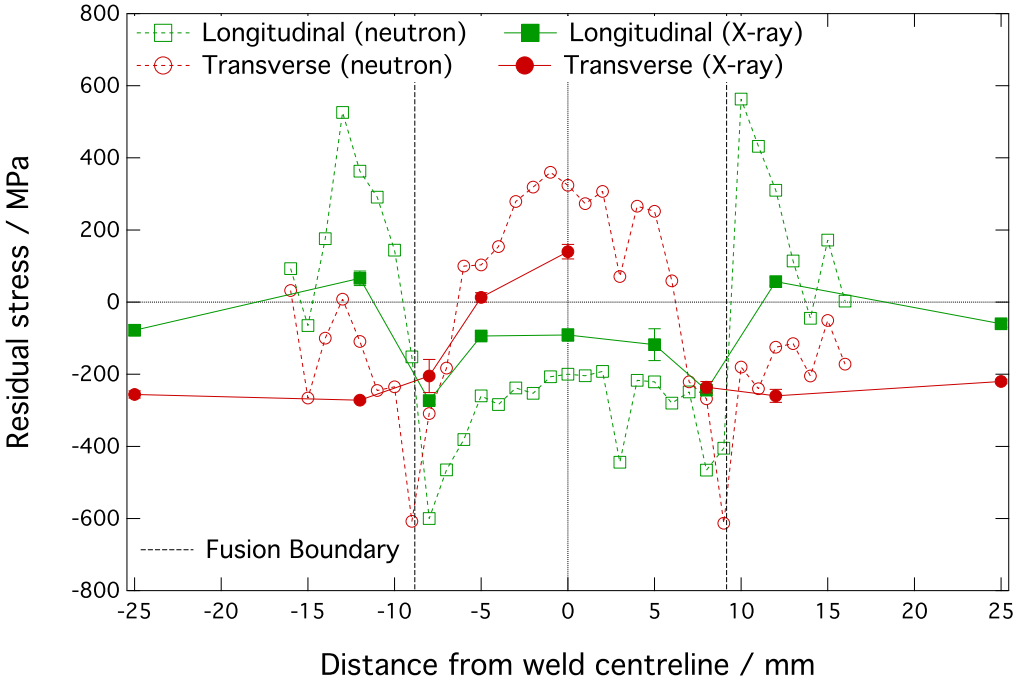

(b)

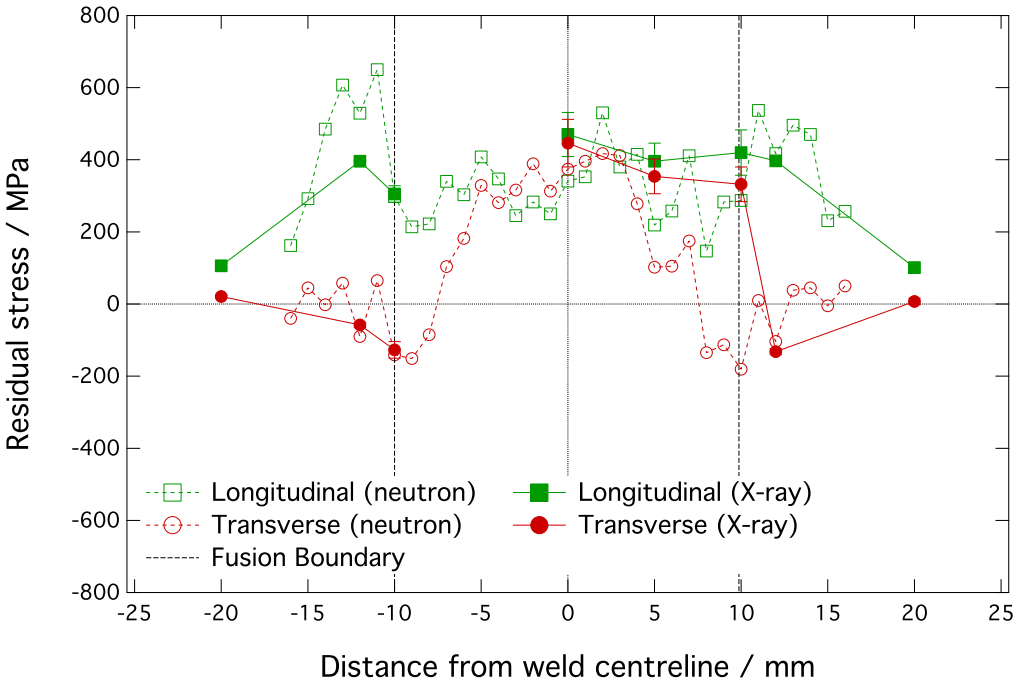

Figure 7.12: Surface residual stresses measured using X-rays (solid lines) and neutrons (dashed lines); (a) weld C, (b) weld H.

surface and near-surface. Weld G, Fig. 7.13, also seems to show a strong correlation between the profile fits. The replication of transverse stress is apparent, but once again the X-ray results do not register the extremes of tension in the HAZ for the longitudinal direction. Referring to the X-ray surface stress profiles in Figs 7.2–7.5, the maximum longitudinal tensile stress in the HAZ for all of the welds is ~ 400 MPa. This is much lower than those recorded by neutron diffraction so there may be a steep longitudinal stress gradient between the surface and the regions a few hundred micrometres below.

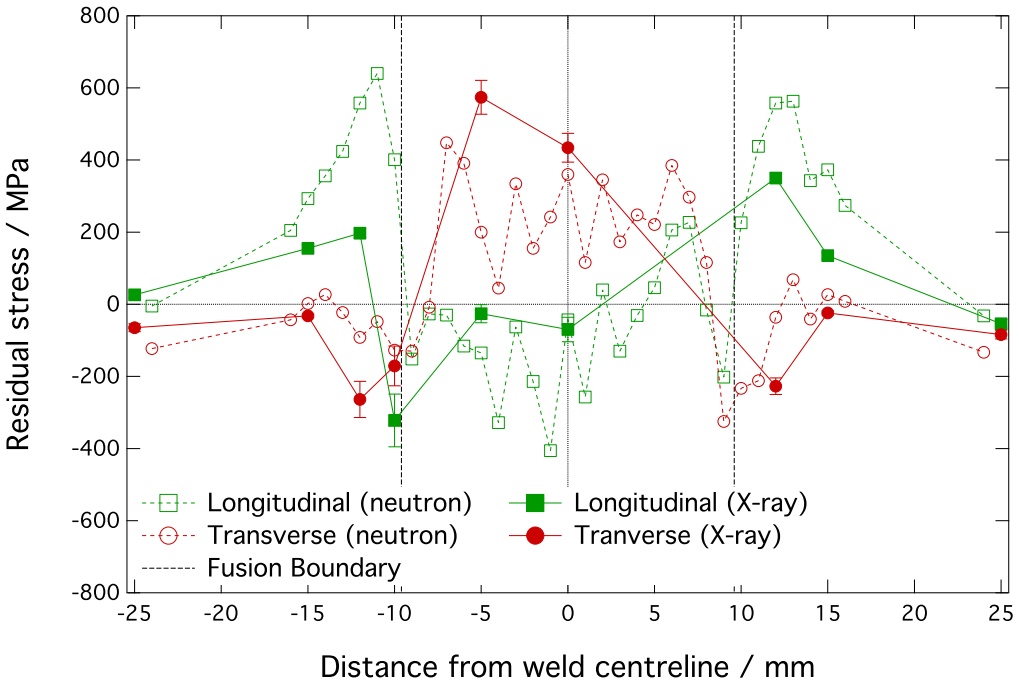

Figure 7.13: Surface residual stresses measured using X-rays (solid lines) and neutrons; weld G.

The change in stress with depth from the surface to the near-surface and into the bulk regions has been identified but the solidification and transformation activities that instigate these variations have yet to be resolved. However, the purpose of the near-surface neutron diffraction experiments was to determine the mechanism by which fatigue properties are enhanced through the use of a low M_S welding alloy. The results suggest that transformation plasticity influences the stress state in the vicinity of the weld toe such that compression is induced at this critical location.

7.4 Conclusions

X-ray and neutron diffraction have been used to assess the residual stress distributions for a series of plates, welded with low transformation-temperature filler alloys. The adoption of a small gauge volume has permitted the measurement of near-surface stresses using neutrons and revealed the local stress variations at the weld toe. Results from the two techniques have been critically compared along with synchrotron X-ray data from literature.

X-ray diffraction data have provided significant evidence for the accumulation of large tensile stress in the weld metal of low M_S filler alloys. The stress was identified in the transverse orientation and occurred for all welding conditions.

The near-surface stress distributions measured by neutron diffraction are comparable with those obtained from X-rays using the $\sin^2\psi$ technique. High tensile stresses were also observed in the transverse direction in the weld deposit. Both data sets agree with stress profiles generated using synchrotron X-rays for a similar, low M_S welding alloy.

The tensile transverse stresses measured in the weld metal became compressive in the vicinity of the fusion boundary. With regards to the neutron data, weld C displayed the greatest levels of compression.

The transverse stresses measured at the surface using X-rays and the near-surface using neutrons produce stress profiles that are radically different to those recorded at a depth of 2.5 mm.

The longitudinal stresses measured in the HAZ at the surface using X-rays are tensile in nature but lower than those registered by neutrons at the near-surface and at a depth of 2.5 mm.

Two low M_S welding alloys have been shown capable of inducing compressive longitudinal residual stress into the surface regions of the weld metal for multipass welds. Both neutron and X-ray diffraction confirm these findings.

Weld C appears to display the most desirable residual stresses as they are compressive in nature at the fusion boundary/weld toe, which is the expected site of crack initiation and subsequent propagation during service. In contrast, weld H, which was produced with a conventional filler alloy, produces tensile longitudinal stress at the fusion boundary.

Weld G, which has a singular capping pass made with the richly alloyed LTT-2 filler, is capable of inducing compressive longitudinal stress in the weld metal near the surface and the stress profile across the fusion boundary appears preferable to weld H.

Chapter 8

General Conclusions & Future Work

The primary objective of this work has been to characterise the residual stresses that develop during the process of multipass arc welding using martensitic, low-transformation temperature welding electrodes. A set of filler alloys and base plates were selected and subjected to strain analysis using neutron diffraction in order to determine the optimum welding conditions. Near-surface neutron diffraction was also used to probe the stress state in the vicinity of the free surface and these results have been compared critically with X-ray diffraction data. The study highlights the differences between the stress distribution at the surface and in the bulk material below. Two low M_S welding alloys were investigated and through detailed neutron diffraction measurements at the weld toe, the mechanism for improved fatigue performance has been established.

The use of diffraction techniques to infer residual stress is invaluable in the structural integrity assessment of welded components. The movement of atomic planes, relative to their equilibrium position in an unstressed state, can be detected through diffraction peak shifts with great accuracy. However, extensive substitutional alloying significantly increases the lattice spacing in the weld deposit. The compositional variation between the richly-alloyed weld metal and relatively lean base plate can mask the residual strains induced by thermal contraction and transformation plasticity. An accompanying strain-free reference specimen was measured alongside each welded plate in an effort to minimise such errors. It was not possible to replicate the exact measurement positions, so a viable function was selected to match the locations in the weld

with the reference specimens. This accounted for transition of the gauge volume into the weld metal, the weld deposit width and the difference of lattice spacing compared with the base material.

Peak broadening and asymmetry also contribute to errors during fitting but varying composition is the most significant source and additionally occurs between welding passes through dilution of the filler with the base plate. This was measured to be approximately 20–25% between the first and final weld layers. EDX and EPMA confirmed that alloying additions fluctuated about a mean level across the weld metal. However, the relatively large sampling volumes associated with neutron diffraction have the capacity to smooth these perturbations. For the purposes of stress calculation, the element concentrations were assumed to be constant across the weld deposit at a given depth based on the above justification. Three different neutron diffraction instruments were used in the course of this investigation but calibration and consistent experimental methods ensured reproducibility between them.

An assessment of stress evolution with increasing number of passes and varying interpass temperatures was performed and a low M_S welding alloy has been shown capable of inducing compressive stress into a multipass weld deposit. This is in direct contrast to the tensile stresses developed in the weld metal of a standard, high M_S filler. The measurement of sequential changes in stress distribution represent how the stress state of underlying layers can be altered. Compression developed in the first welding pass can be eradicated by the deposition of additional layers if the majority of the underlying weld material is not re-austenitised by the heat input of the new layer.

The interpass temperature, relative to the martensite-start temperature, has the potential to significantly influence residual stress. If $T_I > M_S$ for all welding passes, the entire weld remains austenitic until all of the layers have been deposited. It therefore becomes possible to exploit the stress reduction benefits of each and every layer. Conversely, if $T_I < M_S$ the deposition of new weld metal leads to increasingly tensile stresses in the underlying layers, thus reducing or eliminating the beneficial stress state previously created.

Further neutron diffraction studies were conducted with a view to optimising the welding process for industrial applications. The stress contours, overlaid on their respective macrographs, provide an immediate appreciation of the location and magnitude of stress across the weldment and were used to identify the effects of dilution and base plate strength. There is no additional benefit to stress relief through the use of a highly enriched filler, an overly suppressed M_S leads to incomplete martensitic reaction at ambient temperature. This creates the issue of retained austenite in the final weld deposits, which reduce its strength but could prove beneficial if a particularly tough and ductile weld was preferred. It may also enhance fatigue performance through its TRIP qualities, relieving local stress concentrations in service.

If a more consistent microstructure was desired throughout the mulitpass weld deposit, the appropriate procedure may be to begin welding with the highly enriched alloy, to compensate for dilution with the base plate, followed by deposition of the lower alloying content filler. A uniform M_S would ensure that the initial layer transforms simultaneously with any subsequent passes for a specified interpass temperature. However, to minimise the use of these relatively expensive LTT alloys, a final capping pass of the highly enriched filler was deposited onto a standard welding electrode and successfully imparted minor compression into the surface regions of the weld metal.

Peak tensile stresses accumulate in the vicinity of the HAZ, that correlate with the yield strength of the base plate. The re-austenised material that surrounds the weld deposit will transform to martensite at an elevated temperature governed by the base material, leading to tension in these regions. Compression in the weld and tension in the HAZ is a feature of using LTT alloys to join high strength ferritic steels. The use of a low strength base material may negate these thermal contraction strains further because the expanding LTT filler induces compression through plastic deformation into the adjacent plate.

The aim of this research is to improve fatigue performance through controlled stress distribution. The adoption of a small gauge volume has permitted the measurement of near-surface stresses using neutrons and these have been critically compared with X-ray data from this and previous work. Large tensile

stress, in the transverse orientation, was detected in the weld metal of the low M_S alloys. This result was confirmed by both neutron and X-ray diffraction and is in accord with literature. The surface stresses are radically different to those recorded within the bulk for both the transverse and longitudinal directions, even in the same weld layer.

With the small gauge volume set-up, the 3–pass low M_S filler, displayed the greatest level of compression at the weld toe. In contrast, the weld produced with a standard filler accumulates tensile longitudinal stress at the interface. The addition of a final capping pass of richly alloyed filler induced minor compression at the weld boundary, which was preferable to the high M_S weld. The results suggest that transformation plasticity influences the stress state in the vicinity of the weld toe such that compression is induced at this critical location.

8.1 Future Work

A significant amount of work has been performed to characterise the stress state, and the influences of thermal contraction and transformation plasticity have been observed on a macroscale. It would be beneficial to characterise the mechanism of stress alleviation on a smaller length scale through microstructural analysis. A fundamental question is the role of variant selection, if stress is relieved in a particular direction through shear displacement then it follows that it must be compensated for in another.

Given the complexity of physical processes that occur during welding, it would be beneficial to know whether residual stress distribution could be predicted on the basis of the electrode transformation behaviour. Finite element calculations currently account for changes such as: heat flow, material behaviour and strain. Recently developed models also account for transformation plasticity. However, the simulations are not fully representative of the mechanics of stress evolution and this could be improved through the incorporation of variant selection into the models.

The change in stress distribution between the weld metal surface and bulk is evident but the cause needs to be confirmed. Variation is expected between welding layers or materials but not within the same pass to the extent displayed. It is possible that solidification at a free surface, in the absence of restraint, contributes to this phenomenon. Stress measurements combined with a detailed observation of the microstructural changes between the surface and the bulk would reveal the contribution of the surface chill zone.

Fatigue improvement is the goal of these alloys and reconstructing the welds used in this work and then testing them would provide a wealth of information in terms of correlating the residual stresses with fatigue performance. It would be beneficial to develop a reproducible procedure to measure stress at the weld toe of cruciform specimens prior to fatigue testing that allows data to be compared directly between research groups. The fatigue improvements through the use of LTT alloys needs to be benchmarked against different post-weld treatments to establish the cost benefit for industrial application.

References

[1] K. Masubuchi. *Analysis of Welded Structures: Residual Stresses, Distortion and their Consequenses*. International Series on Materials Science and Technology, Volume 33. Pergamon Press, Oxford, 1980.

[2] T. R. Gurney. *Fatigue of welded structures*. Cambridge University Press, 1979.

[3] P. J. Withers and H. K. D. H. Bhadeshia. Residual stress part 1 - measurement techniques. *Materials Science and Technology*, 17:355–365, 2001.

[4] P. J. Withers and H. K. D. H. Bhadeshia. Residual stress part 2 - nature and origins. *Materials Science and Technology*, 17:366–375, 2001.

[5] K. Masubuchi, W. H. Kielhorn, and R. L. Rothman. *Welding Handbook: Fundamentals of Welding*, volume 1, chapter 6. American Welding Society, seventh edition, 1976.

[6] W. K. C. Jones and P. J. Alberry. A model for stress accumulation in steels during welding. *Metals Technology*, 11:557–566, 1977.

[7] J. W. Christian. *Theory of Transformations in Metals and Alloys, Part II*. Pergamon Press, Oxford, U. K., third edition, 2003.

[8] D. A. Porter and K. E. Easterling. *Phase Transformations in Metals and Alloys*. Chapman and Hall, second edition, 1992.

[9] H. K. D. H. Bhadeshia. *Handbook of Residual Stress and Deformation of Steel*, chapter Material Factors, pages 3–10. ASM International, eds G. Totten, M. Howes, T. Inoue, 2002.

[10] J. A. Francis, H. K. D. H. Bhadeshia, and P. J. Withers. Welding residual stresses in ferritic power plant steels. *Materials Science and Technology*, 23(9):1009–1020, 2007.

[11] W. Wang, L. Huo, Y. Zhang, D. Wang, and H. Jiang. New developed welding electrode for improving the fatigue strength of welded joints. *Journal of Materials Science and Technology*, 18:527–531, 2002.

[12] A. Ohta, O. Watanabe, K. Matsuoka, C. Shiga, S. Nishijima, Y. Maeda, N. Suzuki, and T. Kubo. Fatigue strength improvement by using newly developed low transformation temperature welding material. *Welding in the World*, 43:38–42, 1999.

[13] M. Marimuthu. *Design of Welding Alloys for Creep and Toughness*. PhD thesis, University of Cambridge, 2002.

[14] H. Lixing, W. Dongpo, W. Wenxian, and Y. Tainjin. Ultrasonic peening and low transformation temperature electrodes used for improving the fatigue strength of welded joints. *Welding in the World*, 48:34–39, 2004.

[15] S. Kundu. *Transformation Strain and Crystallographic Texture in Steels*. PhD thesis, http://www.msm.cam.ac.uk/phase-trans/2007/complete-thesis.pdf, University of Cambridge, Cambridge, U. K., 2007.

[16] A. A. Shirzadi, H. K. D. H. Bhadeshia, L. Karlsson, and P. J. Withers. Stainless steel weld metal designed to mitigate residual stresses. *Science and Technology of Welding and Joining*, 14:559–565, 2009.

[17] R. J. Moat, H. J. Stone, A. A. Shirzadi, J. A. Francis, S. Kundu, A. F. Mark, H. K. D. H. Bhadeshia, L. Karlsson, and P. J. Withers. Design of weld fillers for mitigation of residual stresses in ferritic and austenitic steel welds. *Science and Technology of Welding and Joining*, 16:279–284, 2011.

[18] L. Karlsson and L. Mráz. Increasing fatigue life with low transformation temperature (LTT) welding consumables. *Zváranie svarováni*, 1–2:8–15, 2011.

[19] A. Kromm, T. Kannengiesser, J. Alenkirch, and J. Gibmeier. Residual stresses in multilayer welds with different martensitic transformation temperatures analyzed by high–energy synchrotron diffraction. *Materials Science Forum*, 681:37–42, 2011.

[20] J. Gibmeier, E. Obelode, J. Altenkirch, A. Kromm, and T. Kannengiesser. Residual stress in steel fusion welds joined using low transformation temperature (LTT) filler material. *Materials Science Forum*, 768–769:620–672, 2014.

[21] J. A. Francis, H. J. Stone, S. Kundu, H. K. D. H. Bhadeshia, R. B. Rogge, P. J. Withers, and L. Karlsson. Effects of filler metal transformation temperature on residual stresses in a high strength steel weld. *Journal of Pressure Vessel Technology*, 131:0414011–0414018, 2009.

[22] H. E. Coules. Contemporary approaches to reducing weld induced residual stress. *Materials Science and Technology*, 29:4–18, 2013.

[23] *Introduction to Arc Welding, Welding Fundamentals and Processes, ASM Handbook*, volume 6A, pages 241—248. ASM International, 2011.

[24] L. E. Svensson. *Control of microstructure and properties in steel arc welds*. CRC Press, 1994.

[25] M. R. James and J. Lu. *Handbook of Measurement of Residual Stresses*, chapter 1. Society for Experimental Mechanics, 1996.

[26] S. Kou. *Welding Metallurgy, Third Edition*. John Wiley and Sons, 2003.

[27] H. K. D. H. Bhadeshia. Developments in martensitic and bainitic steels: Role of the shape deformation. *Materials Science and Engineering A*, A378:34–39, 2004.

[28] H. K. D. H. Bhadeshia and R. W. K. Honeycombe. *Steels: Microstructure and Properties, 3rd edition*. Butterworth–Heinemann, London, 2006.

[29] M. T. Hutchings, P. J. Withers, T. M. Holden, and T. Lorentzen. *Introduction to the characterization of residual stress by neutron diffraction*. CRC Press, Florida, USA, 2005.

[30] M. B. Prime. Cross-sectional mapping of residual stresses by measuring the surface contour after a cut residual stresses by measuring the surface contour after a cut. *Journal of Engineering Materials and Technology*, 123:162–168, 2001.

[31] B. D. Cullity and S. R. Stock. *Elements of X-ray diffraction*. Prentice-Hall, third edition, 2001.

[32] M. François, J. M. Sprauel, C. F. Déhan, M. R. James, F. Convert, J. Lu, J. L. Lebrun, N. Ji, and R. W. Hendricks. *Handbook of Measurement of Residual Stresses*, chapter 5. Society for Experimental Mechanics, 1996.

[33] T. M. Holden and G. Roy. *Handbook of Measurement of Residual Stresses*. Society for Experimental Mechanics, 1996.

[34] T. Nose and T. Okawa. Approaches for fundamental principles 2: Total solution for fatigue of steel . *Nippon Steel Technical Report*, 101:158–163, 2012.

[35] P. J. Bouchard. Residual stresses in lifetime and structural integrity assessment. *Encyclopedia of Materials: Science and Technology*, pages 8134–8142, 2001.

[36] G. E. Dieter. *Mechanical Metallurgy*. McGraw–Hill, 1988.

[37] S. Suresh. *Fatigue of Materials*. Cambridge University Press, second edition, 1998.

[38] H. K. D. H. Bhadeshia, J. A. Francis, H. J. Stone, S. Kundu, R. B. Rogge, P. J. Withers, and L. Karlsson. Transformation plasticity in steel weld metals. In *Proceedings of the 10th International Aachen Welding Conference*, 22–25 October 2007.

[39] H. K. D. H. Bhadeshia. *Bainite in Steels, 2nd edition*. Institute of Materials, London, U.K., 2001.

[40] G. Krauss. Martensite in steel: strength and structure. *Materials Science and Engineering*, A273–A275:40–57, 1999.

[41] Stéphane Forsik. The deflection of scratches by martensite, www.msm.cam.ac.uk/phase-trans/2004/CMisc/scratch/scratch.html, 2004.

[42] P. G. McDougall and C. M. Wayman. The crystallography and morphology of ferrous martensites. In G. B. Olson and W. S. Owen, editors, *Martensite*, pages 59–95, Ohio, USA, 1992. ASM International.

[43] H. K. D. H. Bhadeshia. TRIP–assisted steels? *ISIJ International*, 42:1059–1060, 2002.

[44] G. W. Greenwood and R. H. Johnson. The deformation of metals under small stresses during phase transformations. *Proceedings of the Royal Society A*, 283:403–422, 1965.

[45] J. A Francis, R. J. Moat, H. Abdolvand, and A. Forsey. An assessment of the mechanisms of transformation plasticity in SA508 grade 3 steel during simulated welding thermal cycles. *Materials Science Forum*, 777:188–193, 2014.

[46] S. Kundu, K. Hase, and H. K. D. H. Bhadeshia. Crystallographic texture of stress–affected bainite. *Proceedings of the Royal Society A*, 463:2309–2328, 2007.

[47] H. S. Yang and H. K. D. H. Bhadeshia. Austenite grain size and the martensite-start temperature. *Scripta Materialia*, 60:493–495, 2009.

[48] C. Heinze, A. Pittner, M. Rethmeier, and S. S. Babu. Dependency of martensite start temperature on prior austenite grain size and its influence on welding-induced residual stresses. *Computational Materials Science*, 69:251–260, 2013.

[49] H.-S. Yang, D. W. Suh, and H. K. D. H. Bhadeshia. More complete theory for the calculation of the martensite-start temperature in steels. *ISIJ International*, 52:162–164, 2012.

[50] C. Shiga, H. Y. Yasuda, K. Hiraoka, and H. Suzuki. Effect of M_S temperature on residual stress in welded joints of high-strength steels. *Welding in the World*, 54:71–79, 2010.

[51] J. Wang, P. J. van der Wolk, and S. van der Zwaag. Determination of martensite start temperature in engineering steels, part I, empirical relations describing the effect of steel chemistry. *Materials Transactions JIM*, 41:761–768, 2000.

[52] R. A. Grange and H. M Stuart. The temperature range of martensite formation. *Trans. Am. Inst. Min. Metall. Engng.*, 167:467–501, 1946.

[53] P. Payson and C. H. Savage. Martensite reactions in alloy steels. *Transactions of the American Society for Metals*, 33:261–80, 1944.

[54] K. W. Andrews. Empirical formulae for the calculation of some transformation temperatures. *Journal of the Iron and Steel Institute*, 203:721–727, 1965.

[55] W. Steven and A. G. Haynes. The temperature of formation of martensite and bainite in low alloy steels. *Journal of the Iron and Steel Institute*, 183:349–359, 1956.

[56] C. Y. Kung and J. J. Rayment. An Examination of the Validity of Existing Empirical Formulae for the Calculation of M_S Temperature. *Metallurgical Transactions A*, 13A:328–331, 1982.

[57] G. Ghosh and G. B. Olson. Kinetics of FCC→BCC heterogeneous martensitic nucleation. *Acta Metallurgica and Materialia*, 42:3361–3370, 1994.

[58] H. K. D. H. Bhadeshia. Thermodynamic extrapolation and the martensite-start temperature of substitutionally alloyed steels. *Metal Science*, 15:178–180, 1981.

[59] T. Cool and H. K. D. H. Bhadeshia. Prediction of the martensite–start temperature of power plant steels. *Materials Science and Technology*, 12:40–44, 1996.

[60] C. Capdevila, F. G. Caballero, and C. Garcia de Andrés. Analysis of the effect of alloying elements on the martensite-start temperature of steels. *Materials Science and Technology*, 19:581–586, 2003.

[61] T. Sourmail and C. Garcia-Mateo. A model for predicting the martensite–start temperature of steels. *Computational Materials Science*, 34:213–218, 2005.

[62] W. G. Vermeulen, P. F. Morris, A. P. de Weijer, and S. van der Zwaag. Prediction of martensite start temperature using artificial neural networks. *Ironmaking and Steelmaking*, 23:433–437, 1996.

[63] T. Sourmail and C. Garcia-Mateo. Critical assessment of models for predicting the martensite–start temperature of steels. *Computational Materials Science*, 34:323–334, 2005.

[64] D. P. Koistinen and R. E. Marburger. A general equation prescribing the extent of the austenite-martensite transformation in pure iron–carbon alloys and plain carbon steels. *Acta Metallurgica*, 7:59–60, 1959.

[65] J. Yamamoto, S. Meguro, Y. Muramatsu, N. Hayakawa, and K. Hiraoka. Analysis of martensite transformation behaviour in welded joint using low transformation-temperature materials. *Quarterly Journal of Japan Welding Society*, 25:560–568, 2007.

[66] E. R. Petty. *Martensite fundamentals and technology.* Longman, London, U.K., 1970.

[67] H. Terasaki and Y. Komizo. Diffusional and displacive transformation behaviour in low carbon-low alloy steels studied by a hybrid in situ observation system. *Scripta Materialia*, 64:29—32, 2011.

[68] K. Satoh. Transient thermal stresses of weld heat-affected zone by both-ends-fixed bar analogy. *Transactions of the Japan Welding Society*, 3:125–134, 1972.

[69] K. Satoh. Thermal stresses developed in high-strength steels subjected to thermal cycles simulating weld heat-affected zone. *Transactions of the Japan Welding Society*, 3:135–142, 1972.

[70] A. Ohta, K. Matsuoka, N. T. Nguyen, Y. Maeda, and N. Suzuki. Fatigue strength improvement of lap welded joints of thin steel plate using low

transformation temperature welding wire. *Welding Journal, Research Supplement*, 82:77s–83s, 2003.

[71] A. Ohta, N. Suzuki, Y. Maeda, K. Hiraoka, and T. Nakamura. Superior fatigue crack growth properties in newly developed weld metal. *International Journal of Fatigue*, 21:S113–S118, 1999.

[72] J. Eckerlid, T. Nilsson, and L. Karlsson. Fatigue properties of longitudinal attachments welded using low transformation temperature filler. *Science and Technology of Welding and Joining*, 8:353–359, 2003.

[73] Ph. P. Darcis, H. Katsumoto, M. C. Payares-Asprino, S. Liu, and T. A. Siewert. Cruciform fillet welded joint fatigue strength improvements by weld metal phase transformations. *Fatigue and Fracture of Engineering Materials and Structures*, 31:125–136, 2008.

[74] Y. Kudryavtsev, J. Kleiman, G. Prokopenko, V. Knysh, and L. Gimbrede. Effect of ultrasonic peening on microhardness and residual stress in materials and welded elements. X International Congress and Exposition on Experimental and Applied Mechanics. Society of Experimental Mechanics, 2004.

[75] C. Miki and T. Masayuki. Fatigue strength improvement of out-of-plane welded joints of steel girder under variable amplitude loading. *Welding in the World*, 57:823–840, 2013.

[76] J. A. Francis, H. J. Stone, S. Kundu, R. B. Rogge, H. K. D. H. Bhadeshia, P. J. Withers, and L. Karlsson. Transformation temperatures and welding residual stresses in ferritic steels. In *Proceedings of PVP2007, ASME Pressure Vessels and Piping Division Conference*, pages 1–8, San Antonio, Texas, 2007. American Society of Mechanical Engineers, ASME.

[77] J. Altenkirch, J. Gibmeler, A. Kromm, Th. Kannengiesser, Th. Nitschke-Pagel, and M. Hofmann. In situ study of structural integrity of low transformation temperature (LTT)-welds. *Materials Science & Engineering A*, 528:5566–5575, 2011.

[78] H. J. Stone, H. K. D. H. Bhadeshia, and P. J. Withers. In situ monitoring of weld transformations to control weld residual stresses. In *Stress*

Evaluation Using Neutrons and Synchrotron Radiation, volume 571-572 of *Materials Science Forum*, pages 393–398, 2008.

[79] A. Kromm, Th. Kannengiesser, J. Gibmeier, Ch. Genzel, and V. van der Mee. Determination of residual stresses in low transformation temperature (LTT-) weld metals using X-ray and high energy synchrotron radiation. *Welding in the World*, 53:3–16, 2009.

[80] A. Kromm, Th. Kannengiesser, and J. Gibmeier. In-situ observation of phase transformations during welding of low transformation temperature filler material. *Materials Science Forum*, 638-642:3769–3774, 2010.

[81] A. Kromm and T. Kannengiesser. In-situ-phase analysis using synchrotron radiation of low transformation temperature (LTT) welding material. *Soldagem e Inspecao*, 14:82–88, 2009.

[82] A. Kromm and Th. Kannengiesser. Characterising phase transformations of different LTT alloys and their effect on residual stresses and cold cracking. *Welding in the World*, 55:48–56, 2011.

[83] J. Altenkirch, J. Gibmeier, V. Kostov, A. Kromm, Th. Kannengiesser, S. Doyle, and A. Wanner. Time- and temperature-resolved synchrotron X-ray diffraction: observation of phase transformation and strain evolution in novel low temperature transformation weld filler materials. *Journal of Strain analysis*, 46:563–579, 2011.

[84] C. Heinze, A. Kromm, C. Schwenk, Th. Kannengiesser, and M. Rethmeier. Welding residual stresses depending on solid-state transformation behaviour studied by numerical and experimental methods. *Materials Science Forum*, 681:85–90, 2011.

[85] A. Kromm and T. Kannengiesser. Effect of martensitic phase transformation on stress build-up during multilayer welding. *Materials Science Forum*, 768–769:660–667, 2014.

[86] D. Camilleria, N. McPherson, and T. G .F. Gray. The applicability of using low transformation temperature welding wire to minimize unwanted residual stresses and distortions. *International Journal of Pressure Vessels and Piping*, 110:2–8, 2013.

[87] D. Deng and H. Murakawa. Influence of transformation induced plasticity on simulated results of welding residual stress in low temperature transformation steel. *Computational Materials Science*, 48:55—62, 2013.

[88] J. Yamamoto, K. Hiraoka, and M. Mochizuki. Analysis of martensite transformation behaviour in welded joint using low transformation temperature welding wire. *Science and Technology of Welding and Joining*, 15:104–110, 2010.

[89] H. Murakawa, M. Beres, C. M. Davies, S. Rashed, A. Vega, M. Tsunori, M. K. Nikbin, and D. Dye. Effect of low transormation temperature weld filler metal on welding residual stress. *Science and Technology of Welding and Joining*, 15:393–399, 2010.

[90] H. Dai, A. F. Mark, R. Moat, A. A. Shirzadi, H. K. D. H. Bhadeshia, L. Karlsson, and P. J. Withers. Modelling of residual stress minimization through martensitic transformation in stainless steel welds. In H. Cerjak and N. Enzinger, editors, *Mathematical Modelling of Weld Phenomena 9*, pages 239–252. Technische Universitat GRAZ, 2010.

[91] S. H. Thomas and S. Liu. Analysis of low transformation temperature welding (LTTW) consumables – distortion control and evolution of stresses. *Science and Technology of Welding and Joining*, 19:392–401, 2014.

[92] H. Dai, J. A. Francis, H. J. Stone, H. K. D. H. Bhadeshia, and P. J. Withers. Characterising phase transformations and their effects on ferritic weld residual stresses with X–rays and neutrons. *Metallurgical & Materials Transactions A*, 39:3070–3078, 2008.

[93] M. Takahashi and H. Y. Yasuda. Variant selection of martensites in steel welded joints with low transformation temperature weld metals. *Journal of Alloys and Compounds*, 577:S601–S604, 2013.

[94] L. Karlsson. Improving fatigue life with low transformation temperature welding consumables. *Svetsaren*, 64:27–31, 2009.

[95] L. Karlsson, L. Mráz, H. K. D. H. Bhadeshia, and A. Shirzadi. Alloying concepts for low transformation temperature welding consumables. *Biuletyn Instytutu Spawalnictwa*, 5:33–39, 2010.

[96] Z. Barsoum and M. Gustafsson. Fatigue of high strength steel joints welded with low temperature transformation consumables. *Engineering Failure Analysis*, 16:2186–2194, 2009.

[97] C. Miki, T. Hanji, and K. Tokunaga. Weld repair for fatigue-cracked joints in steel bridges by applying low temperature transformation welding wire. *Welding in the World*, 56:40–50, 2012.

[98] T. Kasuya and K. Sasaki. Flux cored wire for steel sheet with fatigue strength improvement. *Quarterly Journal of Japan Welding Society*, 27:158–162, 2009.

[99] X. Zhao, D. Wang, and C. Deng. Research on fatigue behavior of welded joint spraying fused by low transformation temperature alloy powder. *Materials and Design*, 53:490—496, 2014.

[100] S. Zhao, H. Y. Jing, Y. D. Han, and L. Y. Xu. Electrochemical Behavior of Welded Joints with 308L Stainless Welding Wire and Low Temperature Transformation Welding Wire, 2011.

[101] S. Zenitani, N. Hayakawa, J. Yamamoto, K. Hiraoka, Y. Morikage, T. Yauda, and K. Amano. Development of new low transformation temperature welding consumable to prevent cold cracking in high strength steel welds. *Science and Technology of Welding and Joining*, 12:516–522, 2007.

[102] T. Kasuya, Y. Hashiba, H. Inoue, T. Nose, K. Ito, and M. Enoki. Cold cracking susceptibility of austenitic and martensitic weld metals. *Welding in the World*, 56:76–84, 2012.

[103] M. C. Payares-Asprino, H. Katsumoto, and S. Liu. Effect of martensite start and finish temperature on residual stress development in structural steel welds. *Welding Journal, Research Supplement*, 87:279s–289s, 2008.

[104] F. Martínez and S. Liu. Development of compressive residual stress in structural steelweld toes by means of weld metal transformations. In *ASM Proceedings of the International Conference: Trends in Welding Research*, volume 2005, pages 583–588, 2005.

[105] J. D. Bolton, E. R. Petty, and G. B. Allen. The mechanical properties of α-phase low-carbon Fe-Mn alloys. *Metallurgical Transactions*, 2:2915–2923, 1971.

[106] L. F. G. De Souza, L. De Souza Bott, J. C. F. Jorge, A. S. Guimarães, and R. P. R. Paranhos. Microstructural analysis of a single pass 2.25% Cr–1.0% Mo steel weld metal with different manganese contents. *Materials Characterization*, 55:19–27, 2005.

[107] L. Karlsson, W. Bruins, C. Gillenius, S. Rigdal, and M. Goldschmitz. Matching composition supermartensitic stainless steel welding consumables. In *Supermartensitic Stainless Steels '99*, pages 172–179, Brussels, Belgium, 1999.

[108] Z Zhang and R. A. Farrar. Columnar grain development in C-Mn-Ni low-alloy weld metals and the influence of nickel. *Journal of Materials Science*, 30:5581–5588, 1995.

[109] S. Ooi. Eliminating residual stress in welded joints using transformation plasticity. MoD Ref: R+T/1/0232, 2010.

[110] D. Thibault, P. Bocher, M. Thomas, M. Gharghouri, and M. Côté. Residual stress characterization in low transformation temperature 13%Cr—4%Ni stainless steel weld by neutron diffraction and the contour method. *Materials Science and Engineering A*, 527:6205–6210, 2010.

[111] Y. Mikami, Y. Morikage, M. Mochizuki, and M. Toyoda. Angular distortion of fillet welded T joint using low transformation temperature welding wire. *Science and Technology of Welding and Joining*, 14:97–105, 2009.

[112] D. L. Saraiva, M. Béreš, C. C. Silva, C. S. Nunes, J. J. M. Silva, and H. F. G. Abreu. Application of low M_S temperature consumable to dissimilar welded joint. *Materials Science and Technology*, 30:1057–1062, 2014.

[113] H. Murata, N. Kato, and H. Tamura. Effect of transformation on residual stress in welding. *Quarterly Journal of Japan Welding Society*, 11:545–550, 1993.

[114] D. Amahatslon. Coreweld LTT - 3310. Technical report, ESAB, 2012.

[115] T. Okumura and T. Sourmail. Program MAP STEEL MTTTDATA, http://www.msm.cam.ac.uk/map/steel/programs/MTTTDATA.html, 2004.

[116] NPL. MTDATA. Software, National Physical Laboratory, Teddington, U.K., 2006.

[117] H. J. Stone. *The characterisation and modelling of electron beam welding.* PhD thesis, Department of Materials Science and Metallurgy, University of Cambridge, U. K., 2000.

[118] J. Lu. *Handbook of Measurement of Residual Stresses.* Society for Experimental Mechanics, 1996.

[119] P. J. Withers, M. Preuss, A. Steuwer, and J. W. L. Pang. Methods for obtaining the strain-free lattice parameter when using diffraction to determine residual stress. *Journal of Applied Crystallography*, 40:891–904, 2007.

[120] J. R. Santisteban, M. R. Daymond, J. A. James, and L. Edwards. ENGIN-X: a third-generation neutron strain scanner. *Journal of Applied Crystallography*, 39:812–825, 2006.

[121] M. E. Fitzpatrick and A. Lodini, editors. *Analysis of Residual Stress by Diffraction using Neutron and Synchrotron Radiation.* CRC Press, Florida, USA, 2003.

[122] E. J. Prince. The effect of finite detector slit height on peak positions and shapes in powder diffraction. *Journal of Applied Crystallography*, 16:508–511, 1983.

[123] M .R. Daymond and H .G. Priesmeyer. Elastoplastic deformation of ferritic steel and cementite studied by neutron diffraction and self-consistent modelling. *Acta Materialia*, 50:1613–1626, 2002.

[124] J. W. L. Pang, T. M. Holden, and T. E. Mason. The development of intergranular strains in a high-strength steel. *Journal of Strain Analysis for Engineering Design*, 33:373–383, 1998.

[125] A. N. Paradowska. *Investigation of residual stress in steel welds using neutron and synchrotron diffraction*. Lambert Academic Publishing, 2010.

[126] H.-S. Yang and H. K. D. H. Bhadeshia. Uncertainties in the dilatometric determination of the martensite–start temperature. *Materials Science and Technology*, 23:556–560, 2007.

[127] J. R. Patel and M. Cohen. Criterion for the action of applied stress in the martensitic transformation. *Acta Metallurgica*, 1:531–538, 1953.

[128] Y. K. Yang and S. Kou. Mechanisms of macrosegregation formation near fusion boundary in welds made with dissimilar filler metals. In *Materials Science and Technology Conference and Exhibition, MS and T'07 - "Exploring Structure, Processing, and Applications Across Multiple Materials Systems"*, volume 5, pages 3201–3212, 2007.

[129] H. K. D. H. Bhadeshia. Subroutine MAP STEEL FERR: Calculate ferrite lattice parameter, http://www.msm.cam.ac.uk/map/steel/subs/ferr-b.html, 1999.

[130] H. M. Rietveld. A profile refinement method for nuclear and magnetic structures. *Journal of Applied Crystallography*, 2:65–71, 1969.

[131] G. S. Pawley. Unit-cell refinement from powder diffraction scans. *Journal of Applied Crystallography*, 14:357–361, 1981.

[132] B. Eigenmann and E. Macherauch. X-ray investigation of stress states in materials. *Materialwissenschaft und Werkstofftechnik*, 27:426–437, 1996.

[133] T. I. Ramjaun, H. J. Stone, L. Karlsson, J. Kelleher, R. J. Moat, J. Robelo Kornmeier, K. Dalaei, and H. K. D. H. Bhadeshia. Effect of interpass temperature on residual stresses in multi-pass welds produced using a low transformation temperature filler alloy. *Science and Technology of Welding and Joining*, 19:44–51, 2014.

[134] W. Zinn and B. Scholtes. *Handbook of Residual Stress and Deformation of Steel*, chapter Residual Stress Formation Processes during Welding and Joining, pages 209–219. ASM International, eds G. Totten, M. A. I. Howes, T. Inoue, 2002.

[135] N. H. Tyas. *Grain refinement of austenitic stainless steel welds to facilitate ultrasonic inspection.* PhD thesis, University of Cambridge, Cambridge, U. K., 2000.

[136] H. K. D. H. Bhadeshia and L.-E. Svensson. Modelling the evolution of microstructure in steel weld metals. In H. Cerjak and K. E. Easterling, editors, *Mathematical Modelling of Weld Phenomena*, volume 1, pages 109–182. The Institute of Materials, London, 1993.

[137] K. Satoh. Transient thermal stresses of weld heat–affected zone by both–ends–fixed bar analogy. *Kovove Materialy*, 8:569–587, 1970.

[138] S. Kundu and H. K. D. H. Bhadeshia. Transformation texture in deformed stainless steel. *Scripta Materialia*, 55:779–781, 2006.